
Entangled Photons and Their Applications in Quantum Information Processing

A thesis submitted in partial fulfilment of
the requirements for the degree of

Doctor of Philosophy

by

Sarika Mishra

(Roll No. 17330027)

Under the supervision of

Prof. R. P. Singh

Professor

Atomic, Molecular and Optical Physics Division

Physical Research Laboratory, Ahmedabad, India



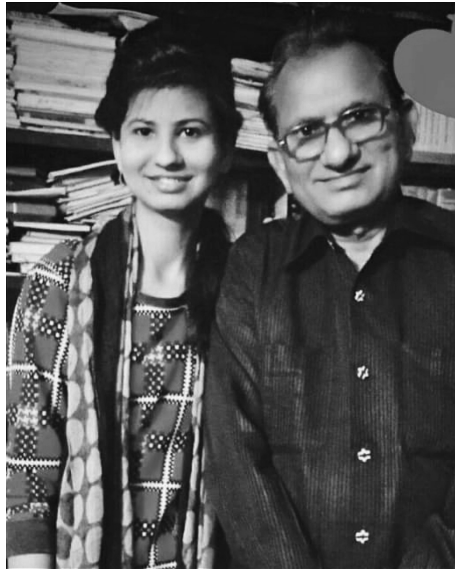
DISCIPLINE OF PHYSICS

INDIAN INSTITUTE OF TECHNOLOGY GANDHINAGAR

2022

गुरुर्ब्रह्मा गुरुर्विष्णुः गुरुर्देवो महेश्वरः ।
गुरुः साक्षात् परं ब्रह्म तस्मै श्री गुरवे नमः ॥

To
My father



His dedication, enduring compassion and support deserves eternal gratitude.

Declaration

I declare that this written submission represents my ideas in my own words and where others' ideas or words have been included, I have adequately cited and referenced the original sources. I also declare that I have adhered to all principles of academic honesty and integrity and have not misrepresented or fabricated or falsified any idea/data/fact/-source in my submission. I understand that any violation of the above will be cause for disciplinary action by the Institute and can also evoke penal action from the sources which have thus not been properly cited or from whom proper permission has not been taken when needed.

Signature

Name: Sarika Mishra

(Roll No: 17330027)

Date:

CERTIFICATE

It is certified that the work contained in the thesis titled “**Entangled photons and their applications in quantum information processing**” by Ms. Sarika Mishra (Roll No. 17330027), has been carried out under my supervision and that this work has not been submitted elsewhere for a degree.

Prof. R. P. Singh

Professor

Atomic, Molecular and Optical Physics Division,

Physical Research Laboratory,

Ahmedabad, India.

(Thesis Supervisor)

Date:

Thesis Approval

The thesis entitled

Entangled Photons and Their Applications in Quantum Information Processing

by

Sarika Mishra

(Roll No. 17330027)

is approved for the degree of

Doctor of Philosophy

Examiner

Examiner

Supervisor

Chairman

Date: _____

Place: _____

Acknowledgments

Finally, I made it! When I come to this section, it feels as if I have accomplished my dream of pursuing the highest degree of my academic career. It would not be wrong if I said that this five-year journey of my Ph.D. was a perfect roller coaster ride of my life and now since the journey is about to end, this doctoral thesis is the reward to all of it. Looking back, I feel like I was never alone in this journey; the constant support, love and prayers of my family, friends, teachers, and well-wishers were always with me and in this section of acknowledgements, I got the opportunity to express my sincere gratitude towards all of them.

First and foremost, I want to express my eternal gratitude to my Papa, Shri Rudra Prasad Mishra, who is the reason behind my successful endeavor. I vividly remember that as a child, whatever I dreamt of, you would put your heart and soul to make it come true papa. Today, whoever I am, and whatsoever I have achieved in my life, is all because of you. Honestly, words aren't enough to express my love, gratitude and respect for you. You are my pride, and I love you, PAPA.

Also, it gives me immense pleasure to express my eternal gratitude to Prof. R.P. Singh for his guidance and encouraging words towards the fulfillment of my research work. I am sincerely blessed to have you as my supervisor. If I recall, on my first visit to your office, somewhere little, I knew that you would be my supervisor. You were also the first one to motivate me and put me in the spotlight in front of others, which gave me the courage to communicate and share knowledge with others. Your simplicity in personal and professional lives along with the way you guide your students made me realize that you are not only a thesis supervisor but also a good friend. Your inspiring stories of the past and of course your retirement plans kept me motivated to achieve my goals throughout. You have always been like a father figure to me, and I am sure that we will continue staying 'entangled' in the future, and that time will not play any role between us.

All the errors, typos, and misunderstandings in this doctoral thesis are probably mine. However, I especially want to thank Prof. R.P. Singh for taking the time to carefully read my thesis and showing me the room for improvement. I hope that my writing skills did not make you mad at me :D.

Moreover, I take this opportunity to express my sincere thanks to my DSC members Dr. Goutam Kumar Samanta, Dr. Rajesh Kumar Kushawaha, and Dr. Shashikiran Ganesh, for

thoroughly reviewing my work. I would like to acknowledge their support, guidance, and patience. Their constructive remarks and friendly behavior always kept me high for my thesis work. Our discussions during the DSC and area seminar always helped me to understand my research work deeper.

I would like to express my profound respect to PRL for providing me with all the fundamental amenities during my research work. I would also like to thank the PRL academic committee members for their insightful comments and encouragement throughout the research period. I am grateful to the academics and administrative staff members of IIT Gandhinagar for helping me with the registration procedure and considering me to reward me with my Ph.D. degree. What's more, I would take this opportunity to express my sincere gratitude to all my teachers who taught me at any stage of my life. Because of their guidance and constant support, I was able to reach this stage where I could write my doctoral thesis.

Finally, I take this opportunity to express my deepest gratitude to the most important persons during my research work; My seniors, Dr. Ali Anwar, Dr. Nijil Lal, Dr. Anidya Banerji and Dr. Ayan Biswas. Firstly, my special thanks to Dr. Ali, who introduced me to the world of quantum optics and taught me the alignment and how to set up an experiment. I remember when I was barely able to couple the laser beam into a single mode fiber and I was getting frustrated then you told me "Sarika, these difficulties will always be there in this career. All you have to learn is some patience and calmness. Things in quantum experiments take time, but you will start getting results eventually." Your words always echoed in my mind whenever I got stucked and unmotivated. Further, I want to thank Dr. Nijil Lal, who has literally been a 'Google' to all my curiosity. During my research work, you always tried to explain things to me in the best possible manner. I always loved our discussions while working in the laboratory. I have always learned from you as to how to be so humble, grounded to earth, and be friendly to everyone. I feel lucky to work with such a gem of a person. Again, I would like to thank Ali and Nijil for taking their time to review my thesis. We, experimentalists, always welcome theoreticians to get extensive theoretical knowledge, and Dr. Anindya Banerji was the only theoretician (PostDoc) in our group. During the Covid lockdown, when I could not go to the laboratory, I started discussing with Dr. Anindya, and it always helped me to understand my subject even better. I have learnt a lot from you during and after the lockdown period too. I would like to thank Dr. Anindya for being part of my Ph.D. journey. Furthermore, I want to thank Dr. Ayan Biswas for teaching me the basics of quantum key distribution protocol and always trying to resolve my confusions about QKD protocols. Thank you for always caring

about my future like an elder brother and providing me with the requisite information about the upcoming PostDoc position.

The inspiration, support, and cooperation I have received from my group members are beyond the scope of any acknowledgment. They were always present for moral support and had created a fun-loving working atmosphere. I would like to express my sincere gratitude to my group members, Dr. Shashi Prabhakar, Satyajeet, Anju, Tanya, Vardaan, Jayant, Pooja, and J.K., for always being there for me. My special thanks goes to Satyajeet for always providing me 'travel loan' with zero interest. It always gave me a chance to take some rest from work and explore the beautiful world around me. I look forward to getting more travel loans from you soon :P. Additionally, I would like to thank Anju for always being there for moral support whenever needed. Next, I want to thank Tanya and Vardaan for their continuous support and care. Especially, I want to thank Vardaan for always appreciating me and the way I am. Thank you Pooja and J.K. for always helping me when I got stuck in computational work. Also, I would like to thank Dr. Shashi Prabhakar for his insightful comments and advice.

I want to take this opportunity to express my deepest gratitude to my friends whom I met here in PRL - Tanmay, Praveen, Ramanuj, Sovan, Sudipto, Deepak, Tanu, and Shivani for their unwavering support and love throughout my journey. Their instant help and positive reinforcement kept me going. I would like to thank Ramanuj, Sovan, and Sudipto for taking care of me like a little child all the time. Thank you, Praveen, for always giving me a "just chill bro" vibe. It is always stress-relieving and fun when we start talking and pulling each other's legs. I always loved your company and your 'bakwas' too :P. Further, I want to thank Deepak for being there with me whenever needed, and thank you for teaching me how Ubuntu works during my initial days in PRL. I would especially like to express my sincere gratitude to Tanmay for consistently keeping an eye on whether I am doing good. The way you keep track of my research progress and push me to complete my work in time makes me confused about who is my actual guide, you or Prof R.P. Singh :P. You have invariably guided me and appreciated my work throughout and now, as you know, I am about to get my highest academic degree; please stop calling me 'Pechi':P. Further, I want to thank my first shopping partner in Ahmedabad, Tanu. I had great fun with you during my stay in Navrangapura hostel. We shopped together, danced together, celebrated every single festival together. Every time I am reminded of a memory of you, my heart goes out. I still cannot process that I will never see you again. You have gone too soon. I pray to God that you have found your peace somewhere in your own universe. Furthermore, I want to thank Shivani for being my partner in worshipping

lord Shiva. I am glad that I have got one more friend like you, just before finishing my Ph.D.

I would also like to thank all the fellow researchers from PRL for being cool and friendly. Especially, I would like to mention Namandeep, Niharika, Ikshu, Arvind Mishra Ji, Surendra, Rahul, Abdur, Priyank, Harish, Shefali, Vishal, Kamlesh, Subith, Rituparna, hrushikesh, Supriyo, Sandeep, Saumya, Arijit, Pranav, Monika, Meghna, Wafikul, Chahat, Malika and many more. Kindly forgive me if I have left out anyone's name and please know that I'm thankful to all of you.

Besides, I would like to acknowledge my friends from Allahabad University, Sumitra, Gayatri, Sufiya, Uma, and Deepak. I would especially like to thank my best buddies Sumitra and Gayatri. It was you from whom I got to know the real meaning of true friends and how it feels to have some good friends. It was and always will be great fun to hang out with you both and pull each other's legs. I am thankful to Uma and Deepak for their constant support and love for me. I would also like to thank Monia for always appreciating me. It was a nice stay with you in Delhi.

I would also like to acknowledge 'Invincible NGO' for giving me the courage to travel alone. I am thankful to some of my new friends I met during my solo traveling. Thank you, Kiran, Vishal, Prabhat, Rahul, Lokendra, Nisarg, Meher, Sonali, Kapil and many more, for making me realize that this world is extremely safe and beautiful to explore even when you are traveling alone. It was great fun traveling with all of you. I, especially, want to thank Kiran for getting married this year. On this pretext I got a chance to attend Gujarati wedding :P.

At some point of time, everybody needs a person with whom they can share what they are feeling inside. And if you are doing Ph.D. in physics, then you must have at least one person with whom you can talk about anything except academic work to relieve all the stress. In this regard, my special thanks and gratitude goes to my bestfriend Ranjan. A little chit-chat with you always calms down my anxieties and insecure thoughts. Your support throughout this journey made me feel that I am not alone and someone is always there to take care of me during my tough times no matter what. Thank you for always listening to my emotional outburst patiently and handling my anxieties without getting irritated :P. You were there for me in my tough times and helped me handle them calmly in all cases.

My words would never be enough to express my parents' love, strength, and encouragement towards me. Yet, I want to express my eternal gratitude to my Mummy-Papa, Shri Rudra

Prasad Mishra and Smt. Chitrarekha Mishra, for their unbroken support and love throughout my life. Without their support, it would not be easy for me to reach this point in my life. My thesis will be incomplete if I don't express my love and thanks to my younger sibling Priyanka, Mona, and Deepak. They always believed in me, encouraged me to pursue my dreams, and provided me with all kinds of support whenever I needed. Furthermore, I want to thank all my family members Khushi, Pari, Muskan, Aditya, Aniket, Renu, Arti, Bharti, and Bhaiya-Bhabhi for their love and support.

I would also like to express my deepest gratitude to all the ancestors of physics who left us with something to work on.

Last but not the least, I want to thank myself for never giving up on any situation. I want to thank me for always believing in me. I want to thank myself for just being me all the time.

Above all, I want to thank God for showering blessings on me at all times.

Sarika Mishra

Abstract

Entangled photons have been used to perform many quantum information protocols such as quantum teleportation, quantum superdense coding, quantum cryptography etc. Spontaneous parametric down-conversion (SPDC) process emerged as one of the best methods to generate entangled photons. The photon pairs generated through SPDC are indistinguishable and maintain a quantum correlation among themselves in different degrees of freedom (DoFs) which leads to the quantum entanglement in those DoF. Among all such DoFs, polarization and orbital angular momentum (OAM) are the two important bases which are widely used to study the fundamental properties of entanglement. We use polarization entangled state to study the BBM92 protocol, an entanglement-based quantum key distribution (QKD) protocol, over 35 meters and 200 meters free-space atmospheric channel, and simultaneously study the effect of aerosols on the secure key rate. This is the first study of its kind where the extinction coefficient of atmospheric aerosols is used to study the variation of entanglement, quantum bit error rate (QBER) and key rate.

A quantum bit with more than two dimensions is known as a qudit. It enables access to a larger Hilbert space, which can provide significant improvement over qubit such as increasing the information capacity per photon in quantum communication, increasing the dimensionality of the Bell state in dense coding etc. Since entangled qudit states have more advantage over entangled qubit states in secure communication, we explore the dimensionality of the OAM entangled state. Higher dimensional entangled states (HD-ES) in OAM have been gaining more attention due to their easy scalability in dimension. Photon pair generated through SPDC theoretically show multi-dimensional entanglement in OAM. The OAM spectrum of the two entangled photons is known as spiral bandwidth (SB). Dimensionality of the entanglement depends on

the size of the spiral bandwidth. We show how the beam waist of the pump mode can affect the bandwidth of the OAM spectrum and how it helps in engineering the higher dimensional entanglement.

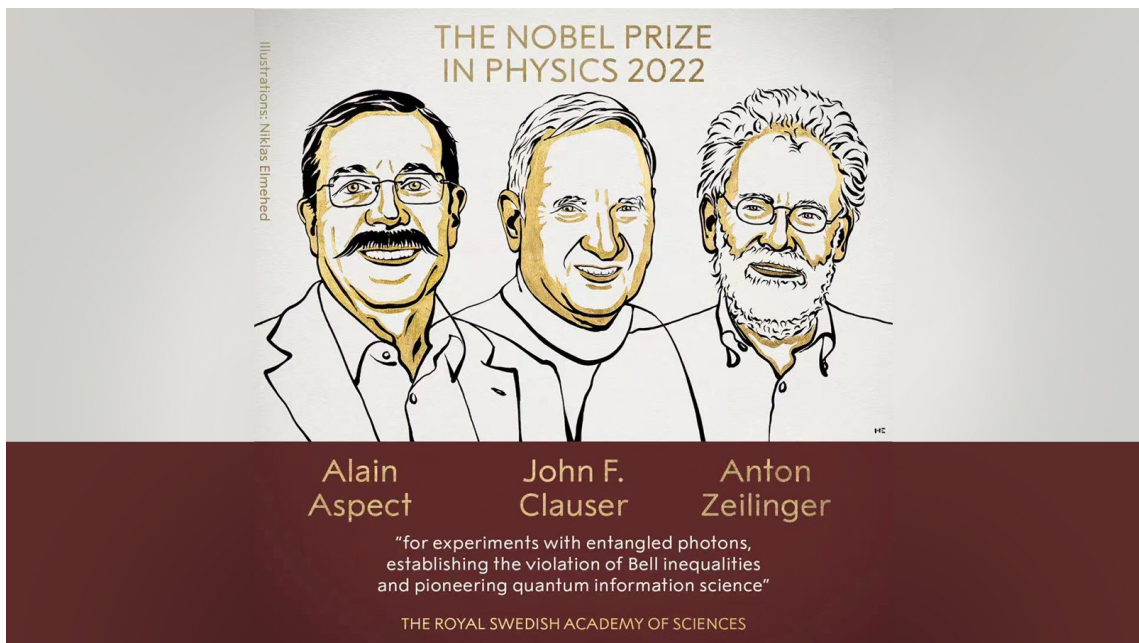
We also investigate the entanglement between different DoFs (polarization and OAM) which is known as hybrid entanglement. It allows the generation of qubit-qudit entanglement. We propose a new method to generate arbitrary classical non-separable state which can be easily transformed into quantum hybrid entangled state through the SPDC process. The effect of random scattering such as through a ground glass plate (GGP) on hybrid entanglement is also investigated.

Keywords: Quantum Entanglement, Quantum Cryptography, Quantum Communication, Quantum Key Distribution, BBM92 Protocol, Structured Light, Orbital Angular Momentum.

Abbreviations

BS	Beam Splitter
PBS	Polarizing Beam Splitter
HWP	Half-Wave Plate
QWP	Quarter-Wave Plate
PM	Prism Mirror
SPDC	Spontaneous Parametric Down-Conversion
EPS	Entangled Photon Source
QKD	Quantum Key Distribution
EB QKD	Entanglement Based Quantum Key Distribution
EC	Error Correction
QBER	Quantum Bit Error Rate
PA	Privacy Amplification
PE	Parameter Estimation
FC	Fiber Coupler
SMF	Single-Mode Fiber
MMF	Multi-Mode Fiber
SPCM	Single Photon Counting Module
SPS	Single Photon Source
SLM	Spatial Light Modulator
SPP	Spiral Phase Plate
CGH	Computer Generated Hologram
DoF	Degree of Freedom
OAM	Orbital Angular Momentum
GGP	Ground Glass Plate

Nobel Prize in Physics 2022



Contents

Acknowledgements	i
Abstract	vii
Abbreviations	ix
Contents	xiii
List of Figures	xxi
List of Tables	xxxiii
1 Introduction	1
1.1 Journey of photon	1
1.2 Basic concepts	3
1.2.1 The photon as an information carrier	3

1.2.2	The concept of qubit	4
1.2.3	Measurement of a qubit	6
1.2.4	Quantum description of a beam-splitter	8
1.2.5	Photon bunching and anti-bunching	10
1.3	Quantum entanglement	12
1.3.1	What is entanglement?	14
1.3.2	Types of quantum entanglement	15
1.3.3	Bell-CHSH inequality	19
1.4	Generation of entangled photon pairs	21
1.4.1	Spontaneous parametric down-conversion (SPDC)	22
1.4.2	Direct and post-selected entanglement	26
1.5	Quantum state tomography	27
1.5.1	The density matrix and Stokes parameter	29
1.5.2	Single-qubit tomography	30
1.5.3	Multi-qubit tomography	32
1.5.4	Qudit tomography	34
1.5.5	Maximum likelihood estimation	36
1.5.6	Extracting information from QST measurements	37

1.6	Applications of quantum entanglement	40
1.6.1	Quantum teleportation	40
1.6.2	Entanglement swapping	41
1.6.3	Superdense coding using entangled state	42
1.6.4	Entanglement-based quantum cryptography	43
1.7	Objective of Thesis	44
1.8	Overview of Thesis	45
2	Indistinguishable photons and entanglement	47
2.1	Introduction	47
2.1.1	Composite systems and identical particles	49
2.1.2	Bosons and fermions	50
2.2	Sources of indistinguishable photons	51
2.2.1	Non-linear crystal based sources	51
2.2.2	Solid-state sources	51
2.3	Quantifying indistinguishability	52
2.3.1	Hong-Ou-Mandel interference	53
2.3.2	Experimental setup and results	56

2.4	Indistinguishability and entanglement	59
2.4.1	Entanglement duality	59
2.4.2	Entanglement in polarization and orbital angular momentum	60
2.4.3	Experimental setup and results	63
2.5	Summary	69
3	Generation and transformation of polarization-entangled Bell states	71
3.1	Introduction	71
3.2	Theory	73
3.3	Experimental setup	77
3.3.1	Entangled photon pair generation	77
3.3.2	Transformation of Bell states	79
3.4	Results and discussion	80
3.5	Conclusion	84
4	Optimised entanglement detection for quantum information protocols	85
4.1	Introduction	85
4.2	Theoretical model	88
4.3	Experimental setup and results	91

4.4	Discussion	97
4.5	Conclusion	97
5	BBM92 quantum key distribution for an atmospheric channel of 200 meters	99
5.1	Introduction	99
5.2	Background	101
5.2.1	Entangled photon-pair source	102
5.2.2	Communication channel and their positioning	104
5.3	Results and Discussion	106
5.4	Conclusion	112
6	Engineering higher dimension entanglement	113
6.1	Introduction	113
6.2	Orbital angular momentum of light	114
6.2.1	Generation of OAM carrying light beam	116
6.2.2	Detection of OAM	119
6.3	Generation of OAM entanglement	120
6.3.1	Experimental setup	122

6.3.2	Results	123
6.4	Engineering higher dimension entangled state	124
6.4.1	Controlling OAM spectrum of two photon entangled state	126
6.4.2	Results and discussion	128
6.4.3	Effect of coupling efficiency on OAM spectrum	132
6.4.4	Entanglement verification	135
6.5	Conclusion	137
7	Scattering of hybrid entangled state	139
7.1	Introduction	139
7.2	Classical non-separable states	140
7.2.1	Experimental setup and results	142
7.3	Polarization entanglement using SPDC	145
7.4	Orbital angular momentum distribution in SPDC	147
7.5	Generation of hybrid entangled states	148
7.5.1	Scattering of hybrid Entanglement	149
7.5.2	Experimental setup and results	150
7.6	Conclusion	154

8 Summary and future scope	155
8.1 Summary of the work done	155
8.2 Scope for future work	159
 List of publications	 161
 Bibliography	 163

List of Figures

1.1	Bloch sphere representation of single qubit	5
1.2	(a) Classical description of beam-splitter, (b) Quantum description of beam-splitter	8
1.3	Experimental setup for (a) Photon anti-bunching, (b) Photon bunching. BS: beam-splitter, CC: coincidence counter, D_1 and D_2 : single photon detectors	11
1.4	Nobel Prize in Physics 2022 has been awarded to Alain Aspect, John F. Clauser and Anton Zeilinger for their groundbreaking experiments using entangled quantum states, the Royal Swedish Academy of Sciences announced on October 4, 2022	13
1.5	Schematic representation of quantum entanglement	14
1.6	(a) Generation of entangled photon pair in spontaneous parametric down-conversion SPDC process. Phase matching condition in this process derives from (b) energy conservation and (c) momentum conservation	22

1.7	SPDC ring distribution of signal and idler for (a) collinear (b) non-collinear geometry	24
1.8	Schematic diagram of quantum teleportation. EPS: entangled photon source, BSM: Bell state measurement,	40
1.9	Schematic diagram of entanglement swapping	42
1.10	Pictorial representation of the layout of the thesis work	46
2.1	The two photon interference (HOM) setup. When a photon enters the input port of an ideal 50:50 beam splitter, it chooses between the reflective or transmissive output ports. The coincidences between the output detectors D_1 and D_2 are recorded through a coincidence counting (CC) electronics.	53
2.2	The state of the system after interference is given by a superposition of all the four possibilities that occur when two photons enter the beam splitter from its two input ports.	54
2.3	The HOM dip obtained when minimum coincidences are recorded between the output ports of the beam splitter. The delay is introduced between the two input ports reducing the indistinguishability and thereby deteriorating the interference.	55

2.4	Experimental setup for the bi-photon interference using Type-I BBO crystal. L_1 , L_2 : lens, BPF: band pass filter, PM: prism mirror, TS: translation stage, M: mirror, HWP: half-wave plate, BS: beam splitter, FC: fiber coupler, SMF: single mode fiber, SPCM: single photon counting module	56
2.5	HOM dip for 3 nm and 10 nm band pass filter (BPF). FWHM of dip for 3 nm filter is wider than the 10 nm filter because of the large coherence length	57
2.6	Variation of coincidence counts at $\Delta L = 0$ as a function of HWP angle θ . Minimum coincidence counts are registered when both the photons have same polarization ($\theta = 0^\circ$, and 90°) and Maximum counts are registered for orthogonally polarized photon pairs ($\theta = 45^\circ$)	58
2.7	Schematic to observe entanglement in the even-odd basis of OAM by sorting photons in polarization. Indistinguishable photons in the Type-II down-converted pairs are sorted in polarization using a polarizing beam splitter (PBS).	64
2.8	OAM correlations corresponding to two orthogonal polarization projections in the collinear SPDC output. Visibility curves are plotted for V port OAM projection angles, $\theta_1 = 0$ (E - green dot), $\theta_1 = \pi/4$ (D_{EO} - red dot), $\theta_1 = \pi/2$ (O - blue dot) and $\theta_1 = 3\pi/4$ (A_{EO} - purple dot). θ_2 is the H port OAM projection angle. Solid curves are respective cosine fits. Error bars indicate statistical uncertainty of one standard deviation.	65

2.9	Schematic to sort the even-odd states of OAM from a collinear SPDC with pump carrying OAM ($m_p = 1$). The Dove prisms within the double Mach-Zehnder interferometer is kept orthogonal to each other. Half wave plate (HWP) along with polarizer (P) corresponds to the polarization projectors. O refers to the constructive port for odd OAM and E labels the constructive port for even OAM.	66
2.10	Verification of sorting of even and odd OAM states. The top two rows correspond to the singles output in the even and odd ports when pumped with a LG mode of order $m = 1$ and the bottom two rows correspond to that for a pump carrying Gaussian mode. The scale is normalized with respect to the maximum counts.	67
2.11	Polarization correlations corresponding to projections in the output ports of the even-odd sorted collinear SPDC output. Visibility curves are plotted for odd port polarization projection angles, $\theta_1 = 0$ (H - green dot), $\theta_1 = \pi/4$ (D - red dot), $\theta_1 = \pi/2$ (V - blue dot) and $\theta_1 = 3\pi/4$ (A - purple dot). θ_2 corresponds to even port projections. Solid curves are respective cosine fits. Error bars indicate statistical uncertainty of one standard deviation.	68
3.1	Schematic diagram of transformation of state	73
3.2	Transformation of Bell states using single-qubit logic gates	75

- 3.3 Experimental setup for the generation of entangled state $|\Psi\rangle^+$. L_1 , L_2 - Lenses, BBO - β -Barium borate crystal, BPF - Band pass filter, PM - Prism mirror, M - Mirror, BS - 50:50 Beam splitter, TS- translation stage, PBS - Polarizing beam splitter, HWP - Half-wave plate, FC - Fiber coupler, SMF - Single mode fiber, SPCM - single photon counting module, CC - Coincidence counter 78
- 3.4 Experimental setup for the transformation of entangled state $|\Psi^+\rangle$ into $|\Psi^-\rangle$ and $|\Phi^+\rangle$ by performing Z and X gate operation respectively using HWP_a only. additional HWP_b along with HWP_a is used to transform the state $|\Psi^+\rangle$ into $|\Phi^-\rangle$ 79
- 3.5 Experimental observation of polarization correlations for (a) $|\Psi\rangle^+$ and (b) $|\Psi\rangle^-$ state. Error bars indicate statistical uncertainty of one standard deviation. The coincidence counts (CC) are plotted along y-axis with the variation of 2β for $\alpha = 0^\circ$ (red), $\alpha = 22.5^\circ$ (blue), $\alpha = 45^\circ$ (green), and $\alpha = 67.5^\circ$ (magenta). 82
- 3.6 Experimental observation of polarization correlations for (a) $|\Phi\rangle^+$ and (b) $|\Phi\rangle^-$ state. Error bars indicate statistical uncertainty of one standard deviation. The coincidence counts (CC) are plotted along y-axis with the variation of 2β for $\alpha = 0^\circ$ (red), $\alpha = 22.5^\circ$ (blue), $\alpha = 45^\circ$ (green), and $\alpha = 67.5^\circ$ (magenta). 82
- 3.7 Calculated density matrix for entangled states (a) $|\Psi\rangle^+$, (b) $|\Psi\rangle^-$, (c) $|\Phi\rangle^+$, and (d) $|\Phi\rangle^-$. F is the state fidelity which is the measure of state overlap 83

- 4.1 Experimental setup used for generating the four Bell states. It is based on the Hong-Ou-Mandel (HOM) interferometer (enclosed in blue dotted box). Photon counting at ports 1 and 2 produces the HOM dip. Boxes A and B are used for polarization entanglement analysis. The blue arrows indicate translation stages. The details are in the text. L_1, L_2 : Lens; BBO : β Barium Borate crystal; TS : Translation Stage; M : Mirror; HWP : Halfwave Plate; BS : Beam Splitter; BB : Beam Blocker; PBS : Polarizing Beam Splitter; FC : Fiber Coupler; SMF : Single Mode Fiber; $SPCM$: Single Photon Counting Module and TDC : Time to Digital Converter. 91
- 4.2 Visibility plot of the HOM interference. We recorded a visibility of 98% measured as the ratio between the difference and sum of maximum and minimum coincidences. 92
- 4.3 Experimental setup used for generating the four Bell states. (A) $|\phi^+\rangle$, (B) $|\phi^-\rangle$, (C) $|\psi^+\rangle$ and (D) $|\psi^-\rangle$. $q[0]$ and $q[1]$ are the qubits. All are initialized to $|0\rangle$ by default. 94
- 4.4 A plot of $|S|$ as a function of the parameter p as in Eqn. 4.13 (black line). The black dashed line marks the value $|S| = 2\sqrt{2}$. The blue squares mark the values of $|S'|$ obtained from the laboratory, and the red circles mark the same obtained from IBM Quantum experience. 96
- 5.1 The block diagram of implemented BBM92 protocol. 102

- 5.2 Schematic diagram of the polarization entangled photon pairs source. Dual polarizing beam splitter D-PBS operates at both 405 nm and 810 nm. Half wave plates $HWP_{1,2,3}$ and $HWP_{4,5,6}$ operate at 405 nm and 810 nm respectively. Lens L_1 : 400 mm, lens L_2 : 200mm, M_1 and M_2 : high reflecting mirrors at 810 nm, Filter: bandpass filter of bandwidth 10 nm centered at 810 nm, PM: prism mirror, SMF: single-mode fiber, SPCM: single-photon counting modules. 103
- 5.3 Arrangement of various components in the channel. It includes the location of Alice and Bob, and their setups. (a) Aerial view of free space entanglement based QKD channel (Image courtesy: Google earth), (b) optical setup of Alice. Red solid lines indicate the direction of entangled photon pair. Out of each pair generated, one stays with Alice and another goes to Bob (c) non-LOS channel consist of one reflecting mirror, (d) front view of Alice and Bob room, (e) optical setup of Bob, (f) preparation of entangled photon pair source (EPS). 104
- 5.4 Schematic of the complete experimental setup that includes both optical and electronic arrangements. EPS: entangled photon source, FM: flip mirror, PM: prism mirror, M: mirror, F: filter, FC: fiber coupler, BS: beam splitter, PBS: polarization beam splitter, HWP: half wave plate, SMF: single-mode fiber, MMF: multi-mode fiber, SPCM: single-photon counting modules. 105
- 5.5 Time delay between Alice and Bob for 200 meters as observed from coincidence histogram. 107

5.6	Obtained H/V and D/A graphs for 35 m channel taken on 8 May 2021. Solid lines are theoretical fit and lines of 98% confidence interval. . .	108
5.7	Obtained H/V and D/A graphs for 200 m channel taken on 10 May 2021. Solid lines are theoretical fit and lines of 98% confidence interval.	109
6.1	Intensity distribution and wavefront of optical vortices of order $m = 0, 1,$ and 2	115
6.2	Intensity (top row) and phase distribution (bottom row) of various LG modes. The red curved arrow shows the direction of energy flow of vortex around the beam axis	116
6.3	Generation of optical vortex beam using SPP	117
6.4	Computer generated holograms for LG mode of order $m = \pm 1, \pm 2 \pm 3$	118
6.5	Working principle of spatial light modulator (SLM)	119
6.6	Experimental setup for measuring the OAM correlation in SPDC. SLM is used to change the spatial mode of Pump. Lens L_1 is used to focus the pump at the center of Type-II PPKTP crystal.	122
6.7	Experimentally measured OAM correlation in SPDC for the pump having (a) $m = -1$ (b) $m = 0,$ and (c) $m = 1$	123
6.8	Bottom row (d-f) shows experimentally recorded OAM spectrum of signal and idler for different pump waist of Gaussian mode and top row (a-c) is corresponding theoretical results. OAM spectrum is expanding with pump waist	129

- 6.9 (Bottom row) Experimentally observed OAM spectrum (Bottom row) for (a) Gaussian pump with $w_p = 106\mu\text{m}$ (b) LG mode of order 1 with $w_p = 196\mu\text{m}$ and (c) LG mode of order 2 with $w_p = 267\mu\text{m}$ 130
- 6.10 Observed OAM spectrum for narrow beam waist for $m = 0, 1, 2$. Size of OAM spectrum is expanding for higher order OAM. Here beam waist of Gaussian pump is $24\mu\text{m}$ 131
- 6.11 Generation of qutrit entangled state using narrow pump waist with superposition of Gaussian mode ($m = 0$) and LG mode ($m = \pm 2\hbar$). Higher order OAM are arising due to the waist mismatch of each mode in superposition state of pump. 132
- 6.12 Effect of coupling efficiency on OAM spectrum for Gaussian pump for various beam size of signal/idler (w) at fiber position. Mode field diameter (MFD) of SMF is $5\mu\text{m}$. Top row (a-c) shows the theoretical results and bottom row (d-f) shows experimentally recorded data. . . . 133
- 6.13 Effect of coupling efficiency on OAM spectrum for LG mode pump ($w_p = 150\mu\text{m}$) of order $m = 1$ for various beam size of signal/idler (w) at fiber position. Mode field diameter (MFD) of SMF is $5\mu\text{m}$. Top row (a-c) shows the Theoretical results and bottom row (d-f) shows experimentally recorded data. 134

- 6.14 Normalized coincidence counts as a function of hologram angle α .
 The angle of hologram β on SLM₂ is fixed while those on SLM₁ is rotated from 0 to π . OAM correlations are corresponding to a) $m = 0/1$ basis, and b) $m = 0/-1$ basis. The normalized coincidences are plotted along y-axis with the variation of α for $\beta = 0^\circ$ (blue), $\beta = 45^\circ$ (green), $\beta = 90^\circ$ (magenta), and $\beta = 135^\circ$ (red). 136
- 6.15 Normalized coincidence counts as a function of hologram angle α .
 The angle of hologram β on SLM₂ is fixed while those on SLM₁ is rotated from 0 to π . OAM correlations are corresponding to $m = 1/-1$ basis. The normalized coincidences are plotted along y-axis with the variation of α for $\beta = 0^\circ$ (blue), $\beta = 45^\circ$ (green), $\beta = 90^\circ$ (magenta), and $\beta = 135^\circ$ (red). 137
- 7.1 Sagnac interferometry based classical non-separable state 141
- 7.2 Experimental setup to generate classical non-separable state. SLM does not modulate the spatial mode of vertical polarized light. Therefore, At the output of SLM, H and V polarized light will have different OAM mode 142
- 7.3 Experimentally generated classical non-separable state of different OAM. SPP of order $m = -2$ is used. m_1 is the order of OAM associated with horizontally polarized light. ϕ is the relative phase between H and V polarized light 143
- 7.4 Experimental setup to produce polarization entangled state 146

7.5	Basic experimental setup to observe orbital angular momentum distribution in SPDC	147
7.6	Experimental setup to generate quantum hybrid entangled state using Type-I BBO crystal. Multimode fiber (MMF) is used to detect OAM of the idler photons and single mode fiber is used to detect the polarization of signal photon with Gaussian mode. Ground glass plate (GGP) used for scattering.	150
7.7	Density matrices of the measured hybrid entangled state (a) before scattering and (b) after scattering	153

List of Tables

3.1	Operation of quantum gate and corresponding HWP angles. The gate transforms an input state to an output state.	77
3.2	Theoretical prediction of detecting entangled photon pair in H/V and D/A bases	81
3.3	Experimental observation of detecting number of entangled photon pairs in H/V and D/A bases	81
3.4	Calculated average visibility and Bell-CHSH parameter S	83
4.1	Coincidence counts with optical qubits. The numbers are actual counts recorded with a coincidence window of 486 ps and integration time of 1 s.	93
4.2	Coincidence counts on IBM Quantum platform. The numbers below are in percentage.	95

5.1	Extinction coefficient (Ext.) and particulate matter (PM _{2.5}) concentrations are averages of hourly data from 12 midnight to 5 AM obtained from the Aerosol Monitoring Laboratory, PRL. The extinction coefficients data correspond to 525 nm. The data is fitted with the Angstrom power law for urban aerosols (model) corresponding to 70% relative humidity (appropriate for April-May) and found that wavelength exponent for extinction coefficients between 525 and 800 nm is about 1.5. Mm: Mega meter.	106
5.2	Summary of the parameters obtained for 35 m channel on 8 May 2021, and 200 m channel on 10 May 2021.	110
7.1	Experimentally recorded parameters, <i>DOP</i> and S_L for classical separable state and non-separable state.	144
7.2	Recorded coincidence counts for entangled state with and without scattering. The integration time is 1 sec for before scattering and 3 sec for after scattering	152
7.3	Recorded parameters for with and without scattering.	153

Chapter 1

Introduction

If quantum mechanics hasn't profoundly shocked you, you haven't understood it yet.

-Niels Bohr

1.1 Journey of photon

Though the word 'Photon' was first introduced by the physical chemist Gilbert Norton Lewis in 1926 [1], all rights of the birth of the 'light quanta' are reserved with the article published by Albert Einstein in 1905 [2]. In his theory of photoelectric effect, he described the particle nature of light to explain the black-body radiation for which he won the Nobel Prize in 1921. Earlier in 1900, the German physicist Max Planck proposed his model of black-body radiation [3]. It retained all classical properties except the quantized interaction of light with matter. In 1905, the quantum picture of light came into existence when Einstein used the concept of Max Planck's black-body radiation and explained that light consists of discrete packets of energy known as light quanta. After 18 years, in 1923, this concept was experimentally verified by the discovery of Compton scattering [4]. Gilbert Lewis in 1926 popularized the term

‘Photon’ as a basic unit of light.

Things started to change when in 1956, Hanbury Brown and Twiss performed an experiment to measure the intensity correlation of light [5]. They divided the light by a half-silvered mirror and detected it by two photomultiplier tubes. This experimental setup is now known as the Hanbury Brown and Twiss (HBT) interferometer. They used this setup to measure the angular size of the star ‘Sirius’ [6]. In 1977, using the HBT interferometer Kimble et al.[7], observed the first evidence of single photon source. They observed the photon antibunching which has no classical analogue. This experiment was considered as a signature of single photon generation. The era of quantum optics started emerging in the late 1960’s which deals with quantum property of light. In 1935, Erwin Schrodinger introduced the term ‘quantum entanglement’ [8]. The concept of entanglement attracted much attention and debates due to its nonlocal behaviour. Einstein, along with Podolsky and Rosen published a paper in 1935 in which he suspected the incompleteness of quantum theory through thought experiments where it violates local realism. In 1964, J.S. Bell proved that the nonlocality is mathematically possible in quantum physics [9]. In 1969, Clauser, Horne, Shimony, and Holt proposed an experiment to test the two photon polarization entanglement using Bell-CHSH inequality [10]. A great mile stone was achieved in 1982, when the first experimental verification of the violation of Bell’s inequality was performed by Alain Aspect [11].

In 1987 and 1988, C. K. Hong, Z. Y. Ou, and L. Mandel performed a series of experiments on biphoton interference (photon bunching) using identical pair of photons generated in spontaneous parametric down-conversion (SPDC) process [12, 13]. They introduced the relationship between photon indistinguishability and quantum interference. The indistinguishability of photons plays an important role in photon bunching,

quantum entanglement, random number generation, and in many quantum information protocols. Their experimental setup is now known as HOM interferometer. It has given a big boost to the research on fundamental quantum phenomena and has been widely used in many quantum information applications.

The journey of photon is rich in history but till now, nobody knows the exact answer of ‘What is light?’. In his old age, Einstein gave his own summary:

“All the fifty years of conscious brooding have brought me no closer to the answer to the question, ‘What are light quanta?’ Of course today every rascal thinks he knows the answer, but he is deluding himself.”

1.2 Basic concepts

1.2.1 The photon as an information carrier

In quantum information protocols, one needs an information carrier whose physical properties can be easily manipulated in order to encode information in it. In quantum world, the information carrier is known as quantum bit or qubit. The information can be encoded in form of different degrees of freedom (DoFs) of qubit. Among all quantum systems, the single photons are the perfect candidate for transferring the information between two parties [14–16]. Using single photons as a qubit carrier has many advantages such as their high speed (3×10^8 m/s), which makes them ‘flying qubits’ that can reach anywhere very easily. Their capacity of encoding huge information, transmission without decoherence in free space and optical fiber and easy detection techniques make them an ideal candidate for quantum key distribution (QKD) protocols [17]. Many physical properties of photons can be used to encode information such

as their polarization, orbital angular momentum (OAM), time-bin, frequency-bin and many more. For manipulation of photonic qubit one can use standard optics, such as birefringent plates (e.g. half-wave plate, quarter-wave plate, quartz plate etc.) and/or interferometers.

1.2.2 The concept of qubit

In classical computers, information is stored and transferred as binary bits that can have only two values, either 0 or 1. In a similar way, in quantum computers, the information is stored in the form of quantum bits or qubits. Qubit is the basic unit of quantum information which represents the quantum state of individual photons. The advantage of qubit over classical bit is that qubit not only represents pure 0 and 1 state but also represents superposition state, in which the photon is considered to be in both the states, 0 and 1, at the same time before measurement [18]. This comes from the superposition principle of quantum physics which says that a particle can be in superposition of different states at the same time, until measured. In general, the superposition state of a single qubit can be written as,

$$|\psi\rangle = \alpha|0\rangle + \beta|1\rangle, \quad (1.1)$$

where, α and β are the probability amplitudes where the quantum information of qubit is stored. From the normalization condition, $|\alpha|^2 + |\beta|^2 = 1$. $|0\rangle$ and $|1\rangle$ are the Dirac notation to represent the quantum states corresponding to 0 and 1. Both the states are orthogonal to each other, $\langle 0|1\rangle = 0$ and can be represented as vectors in two dimensional Hilbert space,

$$|0\rangle = \begin{pmatrix} 1 \\ 0 \end{pmatrix}, \quad |1\rangle = \begin{pmatrix} 0 \\ 1 \end{pmatrix} \quad (1.2)$$

For convenience, Eqn. 1.1 can be rewritten as,

$$|\psi\rangle = \cos\left(\frac{\theta}{2}\right)|0\rangle + e^{i\phi}\sin\left(\frac{\theta}{2}\right)|1\rangle. \quad (1.3)$$

where θ and ϕ are the two degrees of freedom which can be used to control the state $|\psi\rangle$. All the possible quantum states of a single qubit can be visualized using the Bloch sphere of unit radius. The quantum state $|\psi\rangle$ is the state vector pointing at the surface of the sphere characterized by the two angles θ and ϕ .

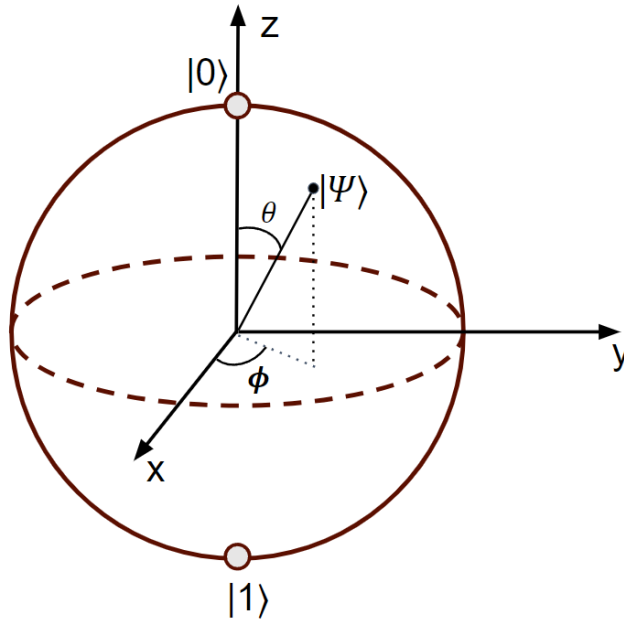


Figure 1.1: Bloch sphere representation of single qubit

Stokes parameter

Any general (pure or mixed) state of a qubit can be uniquely represented by a point on or within the unit sphere [19]. The coordinates of these points are three normalized Stokes parameters, $S = (S_1, S_2, S_3)$, which represent the (x, y, z) axis respectively.

Mathematically, Stokes parameter S_i are the set of four parameters S_0, S_1, S_2, S_3 that describe the state of single-qubit,

$$S_0 = P_{|0\rangle} + P_{|1\rangle}, \quad S_1 = P_{\frac{1}{\sqrt{2}}(|0\rangle+|1\rangle)} - P_{\frac{1}{\sqrt{2}}(|0\rangle-|1\rangle)} \quad (1.4a)$$

$$S_2 = P_{\frac{1}{\sqrt{2}}(|0\rangle+i|1\rangle)} - P_{\frac{1}{\sqrt{2}}(|0\rangle-i|1\rangle)}, \quad S_3 = P_{|0\rangle} - P_{|1\rangle} \quad (1.4b)$$

where $S_0 = 1$ due to normalization. P_i is the probability of finding the state $|i\rangle$. The value of Stokes parameters are given by,

$$\sum_{i=0}^3 S_i^2 = \begin{cases} 1 & \text{Pure state} \\ < 1 & \text{Mixed state} \\ 0 & \text{Maximally mixed state} \end{cases} \quad (1.5)$$

Any two orthogonal states are found on two diametrically opposite points of the Bloch sphere and the lines connecting to these points form a diameter of sphere. The pure qubit states lie on the surface of the Bloch sphere, mixed states lie inside the sphere and totally mixed states are found at the center of sphere.

1.2.3 Measurement of a qubit

Projective measurement is used to know the quantum information encoded in a qubit (as α and β) in terms of probability. Projective measurement is defined as ‘projection of quantum state onto that state whose information we want to extract’. The projection operator can be defined as,

$$P_{proj} = |\psi\rangle\langle\psi|, \quad (1.6)$$

where ψ is the state we want to measure. Let’s consider the state,

$$|\psi\rangle = \sum_n c_n |\psi_n\rangle, \quad (1.7)$$

After projection, the original state $|\psi\rangle$ collapses to give the information about the measured state,

$$\begin{aligned} P_{proj} |\psi\rangle &= |\psi_m\rangle \langle \psi_m | \psi \rangle \\ &= \sum_n c_n |\psi_m\rangle \langle \psi_m | \psi_n \rangle \\ &= c_m |\psi_m\rangle, \end{aligned}$$

where

$$\langle \psi_m | \psi_n \rangle = \delta_{mn} = \begin{cases} 0 & \text{For } m \neq n \\ 1 & \text{For } m = n \end{cases} \quad (1.8)$$

Let's consider the Bloch sphere of a single qubit and say, we want to perform the measurement on z-axis. This means that the projection of state $|\psi\rangle$ (Eqn. 1.3) on either $|0\rangle$ or $|1\rangle$. Using Eqn. 1.3, the corresponding probability of measuring the state $|0\rangle$ or $|1\rangle$ is given as,

$$P_{|0\rangle} = |\langle 0 | \psi \rangle|^2 = \cos^2 \frac{\theta}{2}, \quad (1.9a)$$

$$P_{|1\rangle} = |\langle 1 | \psi \rangle|^2 = \sin^2 \frac{\theta}{2}. \quad (1.9b)$$

To obtain the full information about the qubit whose initial state is $|\psi\rangle$, one has to measure the state along all the three axes x, y, and z. This process is known as quantum state tomography (QST).

1.2.4 Quantum description of a beam-splitter

In quantum world, beam splitter (BS) is an essential optical element that helps to manifest many fundamental quantum tasks such as quantum superposition, quantum interference, quantum entanglement, quantum randomness, etc. Being the heart of many quantum information protocols, it becomes important to understand the quantum description of BS. The classical description leads to incorrect results when it comes to single photon source [20] as shown below.

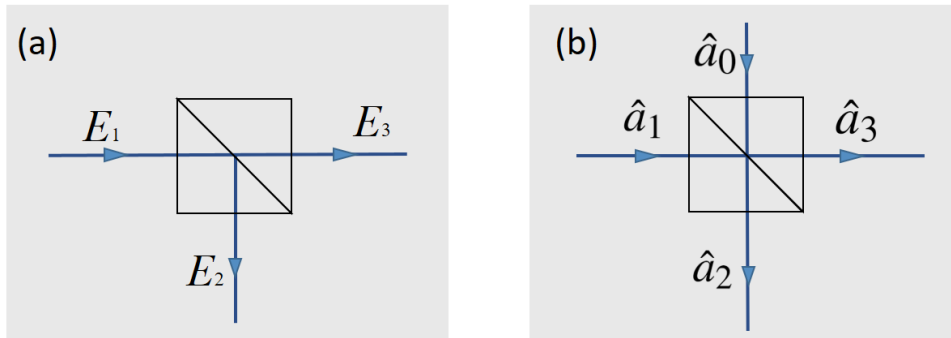


Figure 1.2: (a) Classical description of beam-splitter, (b) Quantum description of beam-splitter

Consider a light beam of complex amplitude E_1 incident on one of the input ports of lossless BS. It is then split between the two output ports of the BS (Figure 1.2a). The output fields can be written in terms of the input field as,

$$E_2 = rE_1 \quad \text{and} \quad E_3 = tE_1, \quad (1.10)$$

where r and t are the reflectance and transmittance of the BS respectively. In a loss-less scenario, $|r|^2 + |t|^2 = 1$. For a 50 : 50 BS, $|r| = |t| = 1/\sqrt{2}$. Since we assumed that it is a lossless BS, the sum of the intensity of output beams should be equal to the intensity

of the input beam,

$$|E_1|^2 = |E_2|^2 + |E_3|^2, \quad (1.11)$$

In quantum description, the complex field amplitude E_i can be replaced by annihilation operator \hat{a}_i as shown in Figure 1.2b,

$$\hat{a}_2 = r\hat{a}_1 \quad \text{and} \quad \hat{a}_3 = t\hat{a}_1, \quad (1.12)$$

According to the quantum mechanics, the annihilation and creation operator \hat{a} and \hat{a}^\dagger must satisfy the commutation relations,

$$[\hat{a}_i, \hat{a}_j^\dagger] = \delta_{ij} = \begin{cases} 0 & i \neq j \\ 1 & i = j \end{cases} \quad (1.13)$$

where δ_{ij} is the kronecker delta symbol. Now, if we calculate the commutation relation using Eqn. 1.12, then

$$[\hat{a}_2, \hat{a}_2^\dagger] = |r|^2, \quad [\hat{a}_3, \hat{a}_3^\dagger] = |t|^2, \quad \text{and} \quad [\hat{a}_2, \hat{a}_3^\dagger] = rt^* \neq 0, \quad (1.14)$$

Since $|r|^2 \neq 1$ and $|t|^2 \neq 1$, therefore if we compare Eqn. 1.13 and Eqn. 1.14 then it is evident that Eqn. 1.14 does not follow the commutation relation. This shows that the classical picture of BS provides incorrect quantum description of light. The reason of getting incorrect results is hidden in ‘unused’ empty input port of BS. In classical picture, the empty input field does not affect the output beams but in quantum picture, the ‘vacuum fluctuation’ has significant importance which can not be ignored. The vacuum state can change the whole scenario and leads to the important physical effect. Now let’s consider the empty port of the BS as a vacuum state, $|0\rangle$, with annihilation

operator, \hat{a}_0 , and rewrite the BS transformation,

$$\hat{a}_2 = r\hat{a}_1 + t'\hat{a}_0 \quad \text{and} \quad \hat{a}_3 = t\hat{a}_1 + r'\hat{a}_0, \quad (1.15)$$

where r' , t' and r , t are the two sets of reflectance and transmittance of an asymmetric BS. The above transformation of BS satisfy the commutation relations as long as the following relations hold,

$$|r| = |r'|, \quad |t| = |t'|, \quad r^*t' + r't'^* = 0, \quad \text{and} \quad r^*t + r't'^* = 0. \quad (1.16)$$

These relations can also be derived from the energy conservation law and known as reciprocity relations.

1.2.5 Photon bunching and anti-bunching

In quantum optics, light beam is considered as a stream of photons. The average number of photons passing through a cross-section of the light beam per unit time is known as photon flux, Φ , and is given by:

$$\Phi = \frac{P}{\hbar\omega} \text{ photons/sec.} \quad (1.17)$$

where ω and P are the frequency and power of the light beam respectively.

Photon anti-bunching

The anti-bunching of photon is purely a quantum effect with no classical counterpart. To prove the quantum nature of a light source, one has to ensure that the photons are coming out from it in an ordered manner, rather than with random time intervals. This

is called photon anti-bunching. Consider a light source that emits one photon at a time which is then incident on one of the input ports of a 50:50 beam splitter (Figure 1.3a). Two single photon detectors, D_1 and D_2 , are kept at the two output ports of the beam splitter. Both the detectors are then connected to a coincidence counter which registers the simultaneous detection of photons. For a truly single photon source, there will be a time intervals between successive photon emissions. Hence if two consecutive photons are detected in D_1 and D_2 , simultaneous detection will not happen and there will be zero coincidence counts at any instant (Figure 1.2a). The probability of detecting two photons at the same time will be zero. This is called anti-bunching. This kind of experimental result can be explained only with quantum description of Hanbury Brown and Twiss (HBT) interferometer [5].

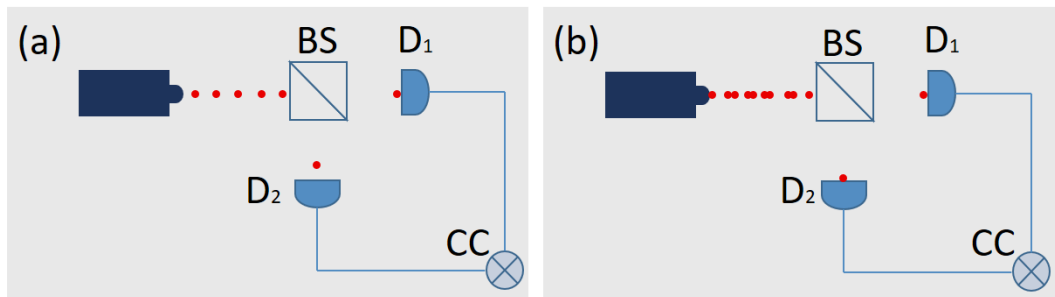


Figure 1.3: Experimental setup for (a) Photon anti-bunching, (b) Photon bunching. BS: beam-splitter, CC: coincidence counter, D_1 and D_2 : single photon detectors

Photon bunching

In this case, two or more photons clumped together in bunches as shown in Figure 1.3b. This means that if bunched photons are incident on one input port of a 50:50 beam splitter and detector D_1 detects one photon at time $t = 0$, then there is a high probability of detecting another photon at detector D_2 simultaneously (Figure 1.3b). As a result, non-zero coincidence counts could be recorded for some detections. The probability of detecting two photons at the same time will be maximum. This is called

photon bunching.

Photon bunching and anti-bunching can be defined in terms of second order correlation function $g^{(2)}(\tau)$ [18],

$$g^{(2)}(\tau) = \frac{n_{12}(\tau)}{n_1(t)n_2(t+\tau)} \quad (1.18)$$

where τ is the time difference between two photons arriving at the detectors D_1 and D_2 . $n_i(t)$ is the number of photons registered at detector D_i at time t and $n_{12}(\tau)$ is the coincidence counts within a short interval, τ . The function $g^{(2)}(\tau)$ is independent of time and it is defined as the conditional probability of detecting a second photon at time $t = \tau$, given that first photon is detected at $t = 0$. Hence $g^{(2)}(0)$ represents the probability of simultaneous detection of photons and would be zero for a single photon source.

1.3 Quantum entanglement

In the EPR paper [8], they questioned the completeness of quantum mechanics based on local realism. They proposed a Gedanken experiment in which if two particles are quantum mechanically correlated, then measuring the position (or momentum) of one particle gives the information of position (or momentum) of the other particle ‘instantaneously’ no matter how far they are. This is clearly a violation of the principle of locality and principle of Heisenberg uncertainty. They claimed that such an experiment directly contradicts the principle of existing quantum mechanics. According to EPR, a complete quantum theory must incorporate the principle of reality and locality. They concluded that, to ensure the completeness of quantum theory, there must be some local hidden variables which decide the outcome of an experiment prior, or independent, to measurement. Thereafter, the search of local hidden variable theory

(LHVT) became the hot topic of research.

In 1964, John Bell formulated his famous theorem where he proved that LHVT and quantum theory predict different results in particular circumstances [9]. He derived an inequality based on local realism which was violated by quantum entanglement. In 1969, John F. Clauser, Michael A. Horne, Abner Shimony, and Richard A. Holt proposed an experiment to check the two photon polarization entanglement using Bell-CHSH inequality [10]. In 1982, the first experimental verification of the violation of Bell's inequality was performed by Alain Aspect [11, 21]. Later on in 1997, Anton Zeilinger and his colleagues demonstrated quantum teleportation using entangled photon source [22]. For their groundbreaking contribution in quantum mechanics, the Royal Swedish Academy of Sciences awarded the Nobel Prize in Physics 2022 to Alain Aspect, John F. Clauser, and Anton Zeilinger *“for experiments with entangled photons, establishing the violation of Bell inequalities and pioneering quantum information science.”*

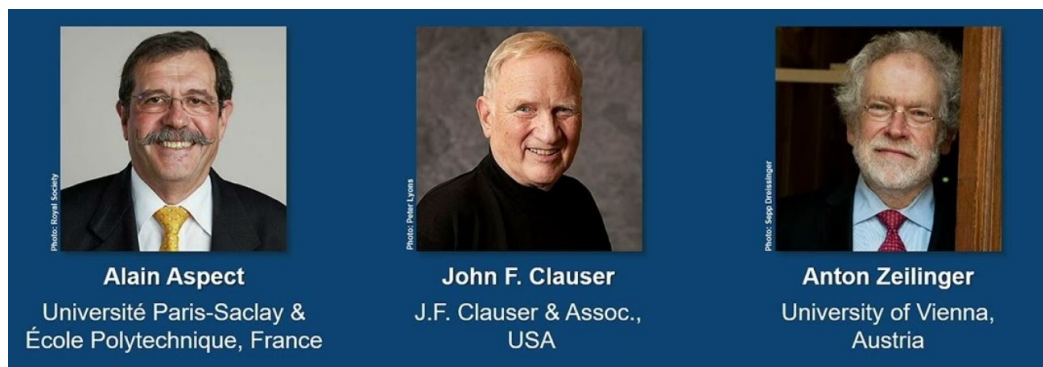


Figure 1.4: Nobel Prize in Physics 2022 has been awarded to Alain Aspect, John F. Clauser and Anton Zeilinger for their groundbreaking experiments using entangled quantum states, the Royal Swedish Academy of Sciences announced on October 4, 2022

1.3.1 What is entanglement?

According to quantum entanglement [23], if two systems are entangled then they share a strong non-local correlation (quantum correlation) which will be maintained even when they are separated by vast distances. The essence of entanglement is that measurement performed on one particle directly affects the state of other particle even when they are far apart (Figure 1.5).

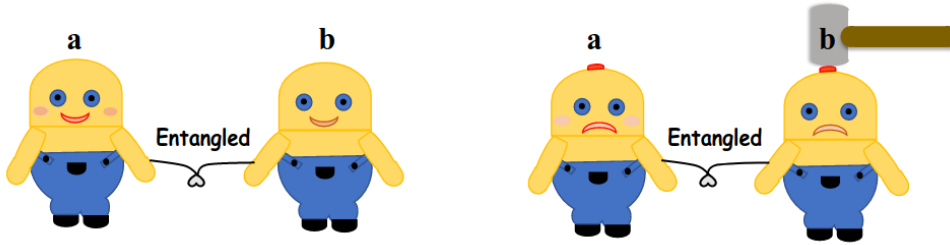


Figure 1.5: Schematic representation of quantum entanglement

Mathematically, an entangled state can be represented as two states which are non-separable. Consider two photons, a and b , whose combined state is written as,

$$|\psi\rangle_{ab} = |\psi\rangle_a \otimes |\psi\rangle_b, \quad (1.19)$$

where $|\psi\rangle_a$ and $|\psi\rangle_b$ are the individual quantum states of each photon. Eqn 1.19 is not entangled state because the combined state can be written as a direct product of the two photons. Therefore measuring the state of photon, a , will not affect the state of photon, b .

A pair of photons is said to be entangled if the quantum state of each particle can not be described independently but only the quantum state as a whole. Mathematically,

$$|\psi\rangle_{ab} \neq |\psi\rangle_a \otimes |\psi\rangle_b. \quad (1.20)$$

Here the state, $|\psi\rangle_{ab}$, is a non-separable state and shows the non-local correlations.

Multipartite entanglement

Entanglement between two photons is called bipartite entanglement. Multipartite entanglement is when N number of photons share entanglement [24, 25]. For example, GHZ states (named after physicists Daniel M. Greenberger, Michael A. Horne and Anton Zeilinger) [26] represents three photons entanglement,

$$|GHZ\rangle = |000\rangle + |111\rangle \quad (1.21)$$

Here, a measurement performed on one photon reveals the outcome of measurements on the other two photons.[27]

1.3.2 Types of quantum entanglement

There are different types of entanglement in terms of different DoFs of photons. One can divide entanglement in two different groups:

1. Continuous-variable (CV) entanglement

- Position and momentum entanglement [28]
- Energy and time entanglement [29]
- OAM and angular position entanglement etc. [30]

2. Discrete-variable (DV) entanglement

- Polarization (or spin) entanglement [29]
- Orbital angular momentum entanglement [31]

- Path entanglement [32]
- time-bin entanglement etc. [33]

Continuous-variable (CV) entanglement

Continuous variable pairs such as position-momentum, Energy-time, and orbital angular momentum-angular position are known as complementary variable or canonically conjugate variable pairs. Heisenberg's uncertainty relationship between two conjugate variables is described by,

$$\Delta x \Delta p \geq \frac{\hbar}{2}, \quad (1.22a)$$

where Δx is the uncertainty in position and Δp is the uncertainty in momentum. Similarly one can write the uncertainty relation in energy-time (ΔE and Δt), and OAM-angular position (ΔL and $\Delta \phi$) as,

$$\Delta E \Delta t \geq \frac{\hbar}{2}, \quad (1.22b)$$

$$\Delta(L) \Delta \phi \geq \frac{\hbar}{2}, \quad \text{respectively.} \quad (1.22c)$$

A violation of conditional uncertainty derived by EPR indicates the entanglement, which is analogous to the original EPR paradox,

$$\Delta(x_1|x_2) \Delta(p_1|p_2) < \frac{\hbar}{2}. \quad (1.23)$$

where x_1, p_1 and x_2, p_2 are the position and momentum of individual photon of entangled pair.

Discrete-variable (DV) entanglement

Photons can be entangled in any degrees of freedom such as spin, polarization, orbital angular momentum which possess discrete values.

Polarization entanglement

Polarization is the most popular DoF for the generation of entanglement due to availability of highly efficient polarization-control components [34]. For two photons entangled in polarization, the entangled state can be written in the form,

$$|\Psi_{ent}\rangle = \frac{1}{\sqrt{2}} (|H\rangle_a |H\rangle_b + |V\rangle_a |V\rangle_b), \quad (1.24)$$

where H and V are horizontal and vertical polarization states. Beauty of above entangled state is that it is invariant under change of polarization basis. Therefore, if we rewrite above equation in rotated polarization basis by an angle α , the original state will remain intact. Let's rewrite above equation in rotated polarization basis,

$$|\Psi_{ent}\rangle_{\alpha} = \frac{1}{\sqrt{2}} (|H_{\alpha}\rangle_a |H_{\alpha}\rangle_b + |V_{\alpha}\rangle_a |V_{\alpha}\rangle_b), \quad (1.25)$$

where,

$$\begin{aligned} |H_{\alpha}\rangle &= \cos \alpha |H\rangle + \sin \alpha |V\rangle, \\ |V_{\alpha}\rangle &= -\sin \alpha |H\rangle + \cos \alpha |V\rangle, \end{aligned} \quad (1.26)$$

If we simplify Eqn. 1.25 by using Eqn. 1.26, we get Eqn. 1.24,

$$\frac{1}{\sqrt{2}} (|H_{\alpha}\rangle_a |H_{\alpha}\rangle_b + |V_{\alpha}\rangle_a |V_{\alpha}\rangle_b) = \frac{1}{\sqrt{2}} (|H\rangle_a |H\rangle_b + |V\rangle_a |V\rangle_b). \quad (1.27)$$

This shows that measuring the state of photon in any polarization basis preserves their entangled state. There are four different polarization entangled states and they are written in the form,

$$\begin{aligned} |\Phi^\pm\rangle &= \frac{1}{\sqrt{2}} \left(|H\rangle_a |H\rangle_b \pm |V\rangle_a |V\rangle_b \right), \\ |\Psi^\pm\rangle &= \frac{1}{\sqrt{2}} \left(|H\rangle_a |V\rangle_b \pm |V\rangle_a |H\rangle_b \right). \end{aligned} \quad (1.28)$$

These states are maximally entangled and are known as Bell states.

OAM entanglement

Unlike polarization which is essentially a two dimensional Hilbert space, orbital angular momentum can theoretically range from $-\infty$ to $+\infty$. Therefore, it can be used to generate higher dimensional entanglement, known as qudit entanglement. A single qudit state in OAM can be written as,

$$|\psi\rangle = \sum_{m=-\infty}^{\infty} C_m |m\rangle, \quad (1.29)$$

where m is the OAM of photon and C_m is the probability amplitude corresponding to the state $|m\rangle$, with the normalization condition $\sum_{m=-\infty}^{\infty} |C_m|^2 = 1$. The two qudit entangled state can be written as:

$$|\psi\rangle = \sum_{m=-\infty}^{\infty} C_m |m, -m\rangle. \quad (1.30)$$

Using d-dimensional or qudit entanglement over qubit enables access to larger Hilbert space and is a valuable resource for secure and efficient quantum information processing. In recent years, entanglement of more than two-dimensions has attracted interest owing to a larger information capacity [35–37]. It provides best security in quantum

information protocols which can not be matched using qubit based system.

Hyper entanglement

In the previous section, we have shown that a system of two photons can be entangled in polarization or OAM. However, they can be entangled in polarization and OAM independently at the same time [38, 39]. This is called hyper entanglement. A hyper entangled state in polarization and OAM is given by,

$$|\phi_{\pm}\rangle = \frac{1}{\sqrt{2}} (|H\rangle_a |H\rangle_b \pm |V\rangle_a |V\rangle_b) \otimes \frac{1}{\sqrt{2}} (|m\rangle_a |-m\rangle_b \pm |-m\rangle_a |m\rangle_b). \quad (1.31)$$

It is important to note here that while there is entanglement in polarization and OAM, there is no entanglement between polarization and OAM [40].

Hybrid Entanglement

In the case of hybrid entanglement [41, 42], two different degrees of freedom, such as polarization and OAM, are entangled with each other [43]. A hybrid entangled state between polarization and OAM can be written as,

$$|\phi_{\pm}\rangle = \frac{1}{\sqrt{2}} (|H\rangle_a |m\rangle_b \pm |V\rangle_a |-m\rangle_b). \quad (1.32)$$

This means that measuring the polarization state of one photon reveals the OAM state of other photon.

1.3.3 Bell-CHSH inequality

To verify the two qubit polarization entanglement, one needs to check for the violation of CHSH version of Bell's inequality [10], which used the correlation of the probabil-

ities $E(\alpha, \beta)$ and introduced an experimentally determinable parameter S ,

$$S = E(\alpha, \beta) - E(\alpha, \beta') + E(\alpha', \beta) + E(\alpha', \beta'), \quad (1.33)$$

where $\alpha, \alpha', \beta, \beta'$ are the four different polarizer angles. Probability correlation $E(\alpha, \beta)$ is defined as,

$$E(\alpha, \beta) = P_{VV}(\alpha, \beta) + P_{HH}(\alpha, \beta) - P_{VH}(\alpha, \beta) - P_{HV}(\alpha, \beta), \quad (1.34)$$

where $P_{VV}(\alpha, \beta)$ is the probability of measuring one photon in $|V_\alpha\rangle$ and another photon in $|V_\beta\rangle$ at the same time. The parameter S is bounded for a classical system,

$$|S| \leq 2, \quad (1.35)$$

For certain choices of angle, $\alpha = 0^\circ, \alpha' = 45^\circ, \beta = 22.5^\circ, \beta' = 67.5^\circ$, quantum mechanical predictions gives maximum violation to this inequality,

$$|S|^{\text{QM}} = 2\sqrt{2} = 2.8284, \quad (1.36)$$

For a maximally entangled state, the theoretically measured value of probability correlation, $|E|$, for above choice of angles is $1/\sqrt{2}$. In order to observe the entanglement, the value of S parameter should be in between 2 and $2\sqrt{2}$,

$$2 < |S|^{\text{Entangled}} \leq 2\sqrt{2}. \quad (1.37)$$

Experimentally, the probabilities P can be defines as,

$$\begin{aligned} P_{VV}(\alpha, \beta) &= \frac{N(\alpha, \beta)}{N_{total}}, & P_{HH}(\alpha, \beta) &= \frac{N(\alpha_{\perp}, \beta_{\perp})}{N_{total}} \\ P_{VH}(\alpha, \beta) &= \frac{N(\alpha, \beta_{\perp})}{N_{total}}, & P_{HV}(\alpha, \beta) &= \frac{N(\alpha_{\perp}, \beta)}{N_{total}} \end{aligned} \quad (1.38)$$

where,

$$N_{total} = N(\alpha, \beta) + N(\alpha_{\perp}, \beta_{\perp}) + N(\alpha, \beta_{\perp}) + N(\alpha_{\perp}, \beta), \quad (1.39)$$

where, $\alpha_{\perp} = \alpha + 90^{\circ}$ and $\beta_{\perp} = \beta + 90^{\circ}$. $N(\alpha, \beta)$ is the experimentally measured number of coincidence counts of photon pairs for the polarizer angles, α , β , α_{\perp} , and β_{\perp} . Now the correlation probability can be written as in terms of photon coincidence counts,

$$E(\alpha, \beta) = \frac{N(\alpha, \beta) + N(\alpha_{\perp}, \beta_{\perp}) - N(\alpha, \beta_{\perp}) - N(\alpha_{\perp}, \beta)}{N(\alpha, \beta) + N(\alpha_{\perp}, \beta_{\perp}) + N(\alpha, \beta_{\perp}) + N(\alpha_{\perp}, \beta)}. \quad (1.40)$$

The CHSH version of Bell's inequality is only applicable for two qubit entanglement. To verify the qudit entanglement, one needs to check CGLMP inequality[44].

1.4 Generation of entangled photon pairs

The most efficient method of generating entangled photon pair is spontaneous parametric down-conversion (SPDC) [45, 46]. This is a non-linear process where an input photon 'pump' of high energy is absorbed in a non-linear second order crystal to create two lower energy photons, signal and idler, at the output. The process is called 'spontaneous' because both the photons are created spontaneously, there are no initial signal and idler fields to stimulate the generation of down-converted photons. They are generated from vacuum energy fluctuations. The term 'parametric' indicates that the non-linear interaction between the photons and crystal does not add or subtract energy or momentum. The term 'down-conversion' means that the generated signal and idler

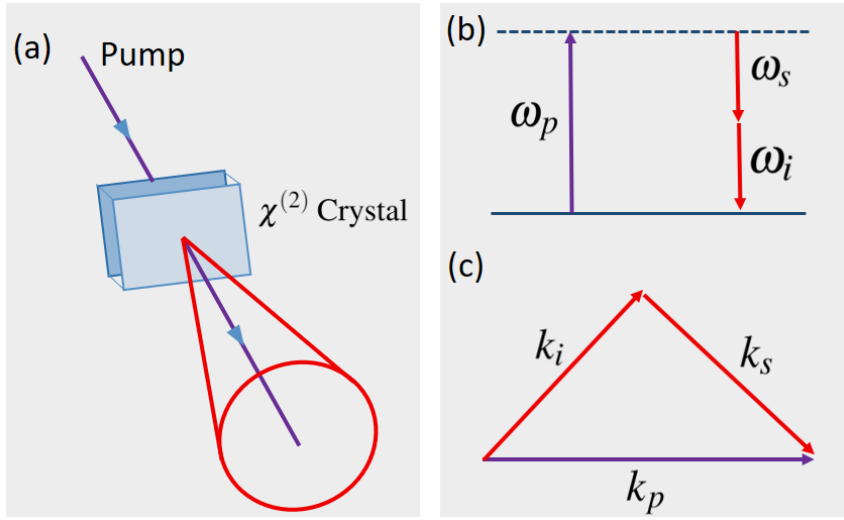


Figure 1.6: (a) Generation of entangled photon pair in spontaneous parametric down-conversion SPDC process. Phase matching condition in this process derives from (b) energy conservation and (c) momentum conservation

photon pairs must have a lower frequency than the pump photon according to energy conservation.

1.4.1 Spontaneous parametric down-conversion (SPDC)

Consider a non-linear crystal characterized by $\chi^{(2)}$ nonlinearity. $\chi^{(2)}$ is the second order susceptibility of the crystal which arises due to the dipole moment per unit volume (or polarization) induced by the electric field of light propagating through the crystal. The dielectric polarization response of the crystal is a nonlinear function of incident electric field and can be written as,

$$P = \chi^{(1)}E_1 + \chi^{(2)}E_1E_2 + \chi^{(3)}E_1E_2E_3 + \dots, \quad (1.41)$$

where $\chi^{(n)}$ is n^{th} -order susceptibility. Consider that the pump field is quantized. The SPDC process requires photon-crystal interaction [47]. Therefore, the interaction

Hamiltonian can be written as,

$$\hat{H} \sim \chi^{(2)} \hat{a}_p \hat{a}_s^\dagger \hat{a}_i^\dagger + H.c. \quad (1.42)$$

where $H.c.$ is the Hermitian conjugate. \hat{a}_p is the annihilation operator of the pump photon. \hat{a}_s^\dagger and \hat{a}_i^\dagger are the creation operator of the signal and idler photons respectively. Because of the ‘spontaneous’ nature of the process, the signal and idler are initially in vacuum states and during the interaction with crystal, the pump photon annihilates and gets converted into two photons, signal and idler,

$$|1\rangle_p |0\rangle_s |0\rangle_i \rightarrow \hat{a}_p \hat{a}_s^\dagger \hat{a}_i^\dagger |1\rangle_p |0\rangle_s |0\rangle_i = |0\rangle_p |1\rangle_s |1\rangle_i. \quad (1.43)$$

Both the photons, signal and idler, are assumed to be created simultaneously. Because of the simultaneous generation, the correlation between both the photons in various degree of freedom have been maintained. This correlation in various DoFs such as polarization, OAM, path, time etc. leads to the entanglement between both the photons.

Phase-matching

SPDC process follows energy and momentum conservation [48]. According to the conservation law, the sum of the energy of signal and idler must be equal to the energy of pump photon. Similarly, sum of the momentum of signal and idler photon must be equal to the momentum of pump photon. These two conservation jointly known as phase matching condition,

$$\begin{aligned} \omega_p &= \omega_s + \omega_i, \\ \vec{k}_p &= \vec{k}_s + \vec{k}_i. \end{aligned} \quad (1.44)$$

where ω_p , ω_s and ω_i are the frequency and \vec{k}_p , \vec{k}_s and \vec{k}_i are the wave vector of pump, signal and idler respectively. Both the photons that emerge from the crystal go along different directions following momentum conservation. Set of all such possible directions form a concentric cone which satisfies the phase matching condition. The transverse profile of the cone is known as SPDC ring. One can select signal and idler at the diametrically opposite points on the SPDC ring. Depending upon the wave vector direction, SPDC ring distribution can have collinear and non-collinear geometry as shown in Figure 1.7.

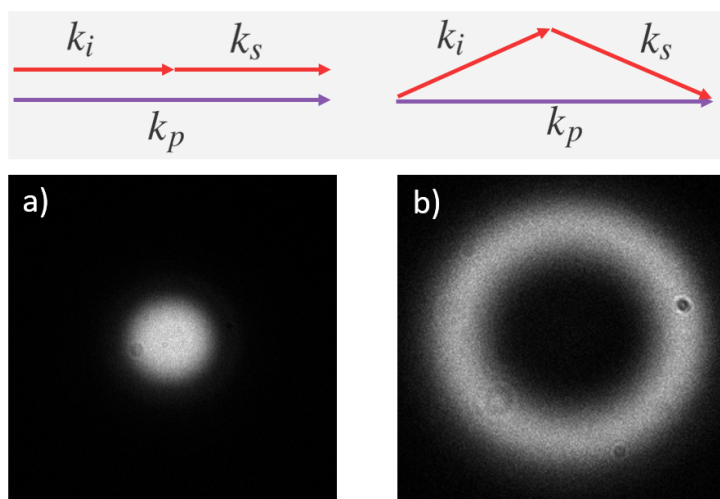


Figure 1.7: SPDC ring distribution of signal and idler for (a) collinear (b) non-collinear geometry

There are two types of phase matching condition: Birefringent phase matching (BPM) and quasi phase matching (QPM). The BPM is achieved by using the birefringence property of non-linear crystal, for example, Beta-Barium Borate (β -BBO), Bismuth Borate (BIBO), and Lithium Niobate (LiNbO_3) crystals. QPM can be achieved by using periodically poled crystal, for example, periodically poled Potassium Titanyl Phosphate (PPKTP), periodically poled Lithium Niobate (PPLN) and periodically poled Lithium Tantalate (PPLT) [49, 50].

Depending upon the crystal structure and orientation of optic axis, there are three types of SPDC:

Type-0 Phase matching: In Type-0 SPDC process, signal, idler and pump all have same polarization [51]. The joint state of SPDC photons for horizontally polarized pump is written as,

$$|\psi\rangle_{\text{SPDC}} = |H\rangle_s |H\rangle_i, \quad (1.45)$$

For vertically polarized pump, the state becomes,

$$|\psi\rangle_{\text{SPDC}} = |V\rangle_s |V\rangle_i. \quad (1.46)$$

Type-I Phase matching: In Type-I SPDC process, signal and idler have same polarization but orthogonal to the pump polarization [50]. The joint state of SPDC photons for horizontally polarized pump is written as,

$$|\psi\rangle_{\text{SPDC}} = |V\rangle_s |V\rangle_i, \quad (1.47)$$

For vertically polarized pump, the state becomes:

$$|\psi\rangle_{\text{SPDC}} = |H\rangle_s |H\rangle_i, \quad (1.48)$$

The state given in Eqn. 1.47 and 1.48 is not entangled. If two Type-I crystal joint together having optical axis perpendicular to each other then one can generate joint polarization entangled state using diagonal/anti-diagonal pump polarization. The joint state of SPDC photons with two crystal stacked together is written as,

$$|\psi\rangle_{\text{SPDC}} = c_1 |H\rangle_s |H\rangle_i \pm c_2 |V\rangle_s |V\rangle_i. \quad (1.49)$$

For maximally entangled state $c_1 = c_2 = 1/\sqrt{2}$. This method was first demonstrated by Kwiat et.al. [34].

Type-II Phase matching: In Type-II SPDC process, signal and idler have orthogonal polarization. Both the photons are emitted along two different cones due to the birefringent property of nonlinear Type-II crystal. And the intersection of the cone provides the polarization entangled state. The joint state of SPDC photons of these intersecting points is written as,

$$|\psi\rangle_{\text{SPDC}} = \frac{1}{\sqrt{2}} (|H\rangle_s |V\rangle_i \pm |V\rangle_s |H\rangle_i). \quad (1.50)$$

Type-II crystal is most commonly used for the generation of polarization entangled state.

1.4.2 Direct and post-selected entanglement

General methods to create an entangled photon pair in polarization and OAM can be divided in two main categories :

- Directly created entanglement
- Post-selectively created entanglement

For example, polarization entanglement can be directly created by using type-II nonlinear crystal or cascaded nonlinear crystal where two Type-I crystals are stacked together with their optic axis orthogonal to each other [52]. In this case, when the photon pair, signal and idler, exit from the crystal, they are directly entangled in polarization. One can observe the entanglement without any selection of subset containing photon pairs.

For post selectively created entanglement [13], Consider two orthogonal polarized photons pass through two input ports of the 50:50 BS. The joint polarization state at the output port of BS is given by,

$$\begin{aligned} |\psi\rangle_{BS} &= \frac{1}{\sqrt{2}}(i|H\rangle_a + |H\rangle_b) \otimes \frac{1}{\sqrt{2}}(|V\rangle_a - i|V\rangle_b) \\ &= \frac{i}{2}(|H\rangle_a|V\rangle_a - |H\rangle_b|V\rangle_b) + \frac{1}{2}(|H\rangle_a|V\rangle_b + |V\rangle_a|H\rangle_b), \end{aligned} \quad (1.51)$$

The above state is not a polarization entangled state. But if we post-select those photon pairs that are detected simultaneously at the output port of the BS then whole state will collapse and final state will become,

$$|\psi\rangle_{\text{entangled}} = \frac{1}{\sqrt{2}}(|H\rangle_a|V\rangle_b + |V\rangle_a|H\rangle_b). \quad (1.52)$$

which is a polarization entangled Bell state. Hybrid entangled states are also generated by applying the post-selection method [53].

1.5 Quantum state tomography

Entangled quantum states have been used as an important tool in various quantum information protocols such as quantum teleportation, entanglement swapping, quantum key distribution, etc. Therefore, it is important to have precise knowledge of the nature of such an entangled state. It is possible to tomographically reconstruct the quantum state of two entangled photons. Quantum state tomography (QST) is a well known technique for the full characterization of any experimentally generated quantum state. It is used to determine the unknown quantum state by reconstructing its density matrix through a series of measurements [19, 54, 55]. The density matrix gives the complete description of any quantum state. It contains all the possible information about

the state and QST aims to extract it. In this section, the basics of state preparation, reconstruction of density matrix and concept of QST is introduced.

Pure state

A general single-qubit pure state can be written as a linear superposition of two orthogonal states $|0\rangle$ and $|1\rangle$,

$$|\psi\rangle = \alpha|0\rangle + \beta|1\rangle, \quad (1.53)$$

where α and β are the probability amplitudes and $|\alpha|^2 + |\beta|^2 = 1$. $|0\rangle$ and $|1\rangle$ can be expressed as,

$$|0\rangle = \begin{pmatrix} 1 \\ 0 \end{pmatrix}, \quad |1\rangle = \begin{pmatrix} 0 \\ 1 \end{pmatrix}, \quad (1.54)$$

The vector representation for the joint state of more than one qubit (say 2-qubit) can be written as,

$$|0\rangle \otimes |1\rangle \equiv |01\rangle = \begin{pmatrix} 1 \\ 0 \end{pmatrix} \otimes \begin{pmatrix} 0 \\ 1 \end{pmatrix} = \begin{pmatrix} 0 \\ 1 \\ 0 \\ 0 \end{pmatrix}, \quad (1.55)$$

The general form of a 2-qubit pure state is given by,

$$|\psi\rangle = \alpha|00\rangle + \beta|01\rangle + \gamma|10\rangle + \delta|11\rangle. \quad (1.56)$$

where α, β, γ , and δ are the corresponding probability amplitudes. The Hilbert space of a multi-qubit is spanned by the state vectors which are tensor products of single qubit state vectors.

Mixed state

A mixed quantum state is described as an incoherent mixture of pure states. It is a statistical ensemble of different pure states $|\psi_i\rangle$ with specific probability P_i . This means that any particle can have a certain probability of being in a given pure state. Mixed state can only be represented by its corresponding density matrix, $\hat{\rho}$, Given as,

$$\hat{\rho} = \sum_i P_i |\psi_i\rangle \langle \psi_i|, \quad (1.57)$$

where P_i is the probability of finding the system pure state $|\psi_i\rangle$ and it is given by,

$$P_i = \langle \psi_i | \hat{\rho} | \psi_i \rangle, \quad (1.58)$$

Note: For $P_i = 1$, the state is called pure state. Hence the density matrix for a pure state is written as,

$$\hat{\rho}_{\text{pure}} = |\psi\rangle \langle \psi|. \quad (1.59)$$

The density matrix can be used to represent both pure and mixed quantum states.

1.5.1 The density matrix and Stokes parameter

Any single-qubit density matrix can be represented as a function of Stokes parameters, S_i , and Pauli matrices, σ_i ,

$$\hat{\rho} = \frac{1}{2} \sum_{i=0}^3 S_i \hat{\sigma}_i, \quad (1.60)$$

The $\hat{\sigma}_i$ matrices are,

$$\hat{\sigma}_0 = \begin{pmatrix} 1 & 0 \\ 0 & 1 \end{pmatrix}, \quad \hat{\sigma}_1 = \begin{pmatrix} 0 & 1 \\ 1 & 0 \end{pmatrix}, \quad \hat{\sigma}_2 = \begin{pmatrix} 0 & -i \\ i & 0 \end{pmatrix}, \quad \hat{\sigma}_3 = \begin{pmatrix} 1 & 0 \\ 0 & -1 \end{pmatrix} \quad (1.61)$$

The set of four Stokes parameters, S_0 , S_1 , S_2 , and S_3 , that describe the polarization state of a single-qubit are given as,

$$\begin{aligned} S_0 &= P_{|H\rangle} + P_{|V\rangle}, & S_1 &= P_{|D\rangle} - P_{|A\rangle} \\ S_2 &= P_{|L\rangle} - P_{|R\rangle}, & S_3 &= P_{|H\rangle} - P_{|V\rangle} \end{aligned} \quad (1.62)$$

where $S_0 = 1$ due to normalization. P_i is the probability of finding the photon in polarization state $|i\rangle$. The value of Stokes parameters are given by,

$$\sum_{i=0}^3 S_i^2 = \begin{cases} 1 & \text{Pure state} \\ < 1 & \text{Mixed state} \\ 0 & \text{Maximally mixed state} \end{cases} \quad (1.63)$$

In order to reconstruct the density matrix, one has to calculate the Stokes parameters experimentally. It is equivalent to the complete set of tomographic measurements [19].

1.5.2 Single-qubit tomography

Consider the reconstruction of density matrix of single qubit polarization state,

$$|\psi\rangle = \alpha |H\rangle + \beta |V\rangle, \quad (1.64)$$

The 2×2 single-qubit density matrix corresponding to the above state is given as,

$$\hat{\rho} = |\psi\rangle\langle\psi| = \begin{array}{c} \langle H| \quad \langle V| \\ |H\rangle \begin{pmatrix} \alpha\alpha^* & \alpha\beta^* \\ \beta\alpha^* & \beta\beta^* \end{pmatrix} \\ |V\rangle \end{array}, \quad (1.65)$$

The matrix, $\hat{\rho}$, can be identified by measuring the Stokes parameters S_1 , S_2 , and S_3 . Any single qubit polarization state can be uniquely represented by a point on or within the unit sphere, known as Bloch sphere or Poincare sphere. The coordinates of the points on the sphere are three normalized Stokes parameters describing the state of polarization. The process of finding the coordinates of unknown state by projective measurement in H/V, D/A, L/R basis on initial state $|\psi\rangle$ and then determining the density matrix is known as quantum state tomography. Polarization projective measurements can be performed using half-wave plates (HWP) and quarter-wave plates (QWP) [54]. The projection state can be written as,

$$|\psi_{proj}(h, q)\rangle = \hat{U}_{HWP}\hat{U}_{QWP}|\psi\rangle, \quad (1.66)$$

where \hat{U}_{HWP} and \hat{U}_{QWP} are unitary operators corresponding to HWP and QWP respectively. Let's denote the projection state corresponding to the particular waveplate angle (h, q) by $|\psi_i\rangle$. Using Eqn. 1.58, the average number of photon counts observed in experiment will be,

$$\begin{aligned} n_i &= N \langle \psi_i | \hat{\rho} | \psi_i \rangle \\ &= NP_i, \end{aligned} \quad (1.67)$$

where N is a constant number that depends upon photon flux and detector efficiency. These photon counts are related to Stokes parameters. Hence with the help of Eqn. 1.60 one can reconstruct the single-qubit density matrix $\hat{\rho}$,

$$\hat{\rho} = \frac{1}{2}(S_0\hat{\sigma}_0 + S_1\hat{\sigma}_1 + S_2\hat{\sigma}_2 + S_3\hat{\sigma}_4). \quad (1.68)$$

This can be further generalized as the complete description of the multi-qubit density matrix.

1.5.3 Multi-qubit tomography

Multiple-qubit pure state can be written as a tensor product of several single qubit states,

$$|\psi\rangle = \sum_{i_1, i_2, i_3, \dots, i_n=0,1} \alpha_{i_1, i_2, \dots, i_n} |i_1\rangle \otimes |i_2\rangle \otimes \dots \otimes |i_n\rangle, \quad (1.69)$$

where n is the number of qubits (n -qubit). Here, α_i is the amplitude coefficient and $\sum_i |\alpha_i|^2 = 1$. The symbol \otimes stands for the tensor product which is used to join the Hilbert spaces of subsystems:

$$|i_1, i_2, i_3, \dots, i_n\rangle = |i_1\rangle \otimes |i_2\rangle \otimes \dots \otimes |i_n\rangle, \quad (1.70)$$

Extending Eqn. 1.60, n -qubit density matrix can be represented as in terms of multi-qubit Pauli operators and Stokes parameters,

$$\hat{\rho} = \frac{1}{2^n} \left(\sum_{i_1, i_2, \dots, i_n=0}^3 S_{i_1, i_2, \dots, i_n} \hat{\sigma}_{i_1} \otimes \hat{\sigma}_{i_2} \otimes \dots \otimes \hat{\sigma}_{i_n} \right). \quad (1.71)$$

From the normalization condition, $S_{0,0,\dots,0} = 1$. This shows that n -qubit density matrix (Eqn. 1.71) can have $(4^n - 1)$ real parameters, i.e. we need multi-qubit Stokes parameter S_{i_1, i_2, \dots, i_n} , to identify the unknown state [19]. The procedure for computing the density matrix for multiple-qubit is exactly same as for single qubit. Example of two-qubit tomography is given below:

Two-qubit tomography

Consider a 2-qubit polarization state,

$$|\psi\rangle = \alpha |HH\rangle + \beta |HV\rangle + \gamma |VH\rangle + \delta |VV\rangle, \quad (1.72)$$

Using $\hat{\rho} = |\psi\rangle\langle\psi|$, density matrix corresponding to 2-qubit is given by,

$$\hat{\rho} = \begin{array}{c} \langle HH| \quad \langle HV| \quad \langle VH| \quad \langle VV| \\ |HH\rangle \\ |HV\rangle \\ |VH\rangle \\ |VV\rangle \end{array} \begin{pmatrix} \alpha\alpha^* & \alpha\beta^* & \alpha\gamma^* & \alpha\delta^* \\ \beta\alpha^* & \beta\beta^* & \beta\gamma^* & \beta\delta^* \\ \gamma\alpha^* & \gamma\beta^* & \gamma\gamma^* & \gamma\delta^* \\ \delta\alpha^* & \delta\beta^* & \delta\gamma^* & \delta\delta^* \end{pmatrix} \quad (1.73)$$

putting $n = 2$ in Eqn. 1.71, the 2-qubit density matrix is given by,

$$\hat{\rho} = \frac{1}{4} \left(\sum_{i,j=0}^3 S_{i,j} (\hat{\sigma}_i \otimes \hat{\sigma}_j) \right), \quad (1.74)$$

where 2-qubit Pauli matrices, σ_{ij} , is given as,

$$\sigma_{i,j} = \sigma_i \otimes \sigma_j, \quad (1.75)$$

For example,

$$\begin{aligned} \sigma_{1,2} &= \sigma_1 \otimes \sigma_2 \\ &= \begin{pmatrix} 0 & 1 \\ 1 & 0 \end{pmatrix} \otimes \begin{pmatrix} 0 & -i \\ i & 0 \end{pmatrix} \\ &= \begin{pmatrix} 0 & 0 & 0 & -i \\ 0 & 0 & i & 0 \\ 0 & -i & 0 & 0 \\ i & 0 & 0 & 0 \end{pmatrix} \end{aligned}$$

Similarly, the 2-qubit Stokes parameters S_{ij} , can be written as a tensor product of single-qubit Stokes parameters,

$$S_{ij} = S_i \otimes S_j, \quad (1.76)$$

For example,

$$\begin{aligned} S_{0,3} &= S_0 \otimes S_3 \\ &= (P_{|H\rangle} + P_{|V\rangle}) \otimes (P_{|H\rangle} - P_{|V\rangle}) \\ &= P_{|HH\rangle} - P_{|HV\rangle} + P_{|VH\rangle} - P_{|VV\rangle}. \end{aligned}$$

where P_{HV} is the joint probability of detecting one photon in $|H\rangle$ and another photon in $|V\rangle$.

1.5.4 Qudit tomography

The single-qudit state of dimension, d , is represented as,

$$|\psi\rangle = \alpha_0 |0\rangle + \alpha_1 |1\rangle + \dots + \alpha_{d-1} |d-1\rangle, \quad (1.77)$$

The mixed qudit state can be written as,

$$\hat{\rho} = \sum_{i=0}^{d-1} P_i |\psi_i\rangle \langle \psi_i|, \quad (1.78)$$

In order to reconstruct qudit density matrix,

$$\hat{\rho} = \frac{1}{d} \left(\sum_{i=0}^{d-1} S_i \hat{\sigma}_i \right), \quad (1.79)$$

it is necessary to find S_i and σ_i matrices similar to qubit matrices. For simplicity, divide both the matrices in three different groups $\{X, Y, Z\}$: $\{S_i^X, S_i^Y, S_i^Z\}$ and $\{\sigma_i^X, \sigma_i^Y, \sigma_i^Z\}$, where $\sigma^X \equiv \sigma_1$, $\sigma^Y \equiv \sigma_2$, and $\sigma^3 \equiv \sigma_3$ [55]. According to this division, we can rewrite the density matrix as,

$$\hat{\rho} = \frac{1}{d} \left(S_0 \hat{\sigma}_0 + \sum_{j,k=0:j \neq k}^{d-1} (S_{j,k}^X \hat{\sigma}_{j,k}^X + S_{j,k}^Y \hat{\sigma}_{j,k}^Y) + \sum_{r=1}^{d-1} S_r^Z \sigma_r^Z \right), \quad (1.80)$$

where $S_0 = 1$ and $\hat{\sigma}_0 = I$. The X and Y labeled Stokes parameters and $\hat{\sigma}$ matrices are defined identically to that of qubit,

$$\hat{\sigma}_{j,k}^X = |j\rangle \langle k| + |k\rangle \langle j|, \quad (1.81a)$$

$$\hat{\sigma}_{j,k}^Y = -i(|j\rangle \langle k| - |k\rangle \langle j|), \quad (1.81b)$$

$$S_{j,k}^X = P_{\frac{1}{\sqrt{2}}(|j\rangle + |k\rangle)} - P_{\frac{1}{\sqrt{2}}(|j\rangle - |k\rangle)}, \quad (1.81c)$$

$$S_{j,k}^Y = P_{\frac{1}{\sqrt{2}}(|j\rangle + i|k\rangle)} - P_{\frac{1}{\sqrt{2}}(|j\rangle - i|k\rangle)}, \quad (1.81d)$$

The expressions for S_r^Z and $\hat{\sigma}_r^Z$ are a bit more complex and expressed as,

$$\hat{\sigma}_r^Z = \sqrt{\frac{2}{r(r+1)}} \left(\sum_{j=0}^{r-1} |j\rangle \langle j| - r|r\rangle \langle r| \right), \quad (1.82a)$$

$$S_r^Z = \sqrt{\frac{2}{r(r+1)}} \left(\sum_{j=0}^{r-1} P_{|j\rangle} - rP_{|r\rangle} \right). \quad (1.82b)$$

These are the complete set (d^2) of $\hat{\sigma}$ matrices and Stoke's parameters.

Physical density matrix

The density matrix for all physical states must have the following properties to be physical [56],

- The density matrix should be normalized, i.e. $\text{Tr}\{\hat{\rho}\} = 1$.
- should be Hermitian, i.e. $\hat{\rho}^\dagger = \hat{\rho}$.
- should be positive semidefinite, i.e. all the non-negative eigenvalues must lie in the interval $[0,1]$ and their sum must be equal to 1.

Reconstructing the quantum state is a probabilistic process. Sometimes experimental errors and statistical fluctuations in photon counts measured in single-photon detector can affect the reconstruction of quantum state. Hence the tomographic measurement of the density matrix can produce the results that violate the essential properties of matrices such as positive semidefinite. To avoid this problem, one can optimize the density matrix using maximum likelihood estimation (MLE) process.

1.5.5 Maximum likelihood estimation

Experimental inaccuracies, imperfect projections and statistical fluctuations of coincidence counts may lead to the ‘unphysical’ density matrix. Maximum likelihood estimation (MLE) is simple technique to get back the physical density matrix [54, 56].

The basic approach of MLE is as follows:

- Compute the experimental density matrix using tomographic measurements on the quantum state.

- Guess the ideal density matrix based on experimentally reconstructed matrix.
- From the ideal density matrix, compute the set of tomographic measurement of the ideal state.
- Using optimization technique, compute the difference (χ) between ideal and experimental tomographic measurements,

$$\chi = \left(\sum_i \frac{C_{ideal}^i - C_{exp}^i}{\sqrt{C_{exp}^i + 1}} \right)^2. \quad (1.83)$$

where i represents the i^{th} tomographic projection. C_{exp} and C_{ideal} are the tomographic measurements for experimentally derived density matrix and ideal density matrix respectively.

- Optimize the ideal density matrix such that it minimizes the value of χ .

The above approach ensures that the optimized density matrix is Hermitian with positive semidefiniteness.

1.5.6 Extracting information from QST measurements

From the reconstructed density matrix one can extract many information about an unknown quantum state such as fidelity, entropy, concurrence and tangle.

Fidelity: Fidelity, F , is the measure of state overlap and it quantifies the similarity between the target matrix, $\hat{\rho}_t$, and reconstructed density matrix, $\hat{\rho}$. It is represented by,

$$F(\hat{\rho}_t, \hat{\rho}) = Tr \left(\sqrt{\sqrt{\hat{\rho}_t} \hat{\rho} \sqrt{\hat{\rho}_t}} \right)^2, \quad (1.84a)$$

If $\hat{\rho}_t$ is a pure state then,

$$F = \text{Tr}[\hat{\rho}_t \hat{\rho}]. \quad (1.84b)$$

If both the matrices are identical then, $F = 1$ and if there is no similarity between them then, $F = 0$.

Linear entropy: Linear entropy, S_L , quantifies the purity of state. It computes the degree of mixedness in a quantum state, and is given by,

$$S_L = \frac{4}{3} (1 - \text{Tr}\{\hat{\rho}^2\}) = \begin{cases} 0 & \text{Pure state} \\ 1 & \text{Mixed state} \end{cases} \quad (1.85)$$

Von Neumann entropy: Von Neumann entropy, S , is mainly used to measure the purity of a quantum entangled state.

$$S \equiv -\text{Tr}\{\hat{\rho} \log_2(\hat{\rho})\} = -\sum_i \lambda_i \log_2\{\lambda_i\} = \begin{cases} 0 & \text{Pure state} \\ 1 & \text{Mixed state} \end{cases} \quad (1.86)$$

where λ_i is the eigenvalue of density matrix, $\hat{\rho}$.

Concurrence and Tangle: Concurrence, C , and Tangle, T , are used to measure the degree of entanglement or quantum-coherence properties of entanglement. The concurrence for a 2-qubit pure state, $|\psi\rangle$, is defined by,

$$C(|\psi\rangle) = \sqrt{2(1 - \text{Tr}(\hat{\rho}_A^2))} = \sqrt{2(1 - \text{Tr}(\hat{\rho}_B^2))}, \quad (1.87)$$

where ρ_A and ρ_B are the reduced density matrices, given by,

$$\begin{aligned}
 \rho_A &= \text{Tr}_B[|\psi\rangle\langle\psi|] \\
 &= \langle H|_B \hat{\rho} |H\rangle_B + \langle V|_B \hat{\rho} |V\rangle_B, \\
 \rho_B &= \text{Tr}_A(|\psi\rangle\langle\psi|) \\
 &= \langle H|_A \hat{\rho} |H\rangle_A + \langle V|_A \hat{\rho} |V\rangle_A,
 \end{aligned} \tag{1.88}$$

Using Eqn. 1.73 in above equation, the reduced density matrix ρ_A and ρ_B will become,

$$\hat{\rho}_A = \begin{array}{c} \langle H| \\ \langle V| \end{array} \begin{array}{cc} & \begin{array}{c} \langle H| \\ \langle V| \end{array} \\ \begin{array}{c} |H\rangle \\ |V\rangle \end{array} & \begin{pmatrix} \alpha\alpha^* + \beta\beta^* & \alpha\gamma^* + \beta\delta^* \\ \gamma\alpha^* + \delta\beta^* & \gamma\gamma^* + \delta\delta^* \end{pmatrix} \end{array}$$

$$\hat{\rho}_B = \begin{array}{c} \langle H| \\ \langle V| \end{array} \begin{array}{cc} & \begin{array}{c} \langle H| \\ \langle V| \end{array} \\ \begin{array}{c} |H\rangle \\ |V\rangle \end{array} & \begin{pmatrix} \alpha\alpha^* + \gamma\gamma^* & \alpha\beta^* + \gamma\delta^* \\ \beta\alpha^* + \delta\gamma^* & \beta\beta^* + \delta\delta^* \end{pmatrix} \end{array}$$

Tangle T can be directly calculated from the Concurrence C ,

$$T = C^2. \tag{1.89}$$

The value of the tangle and the concurrence can range from 0 to 1. For product state or mixed state the value is 0 and for pure state (e.g. maximally entangled states) the value is 1.

1.6 Applications of quantum entanglement

The quantum properties of light such as superposition principle and quantum entanglement lie at the heart of quantum optics. The basic idea of quantum information processing (QIP) is to use these two important principles of quantum physics to enhance the capabilities of storing and transferring the data [15, 57–59]. Applications of QIP which utilise the properties of quantum entanglement as a resource are given below:

1.6.1 Quantum teleportation

Quantum teleportation is the technique to transfer a quantum state of qubit from one location to another without direct exchange of the qubit [22, 60–63]. In this protocol,

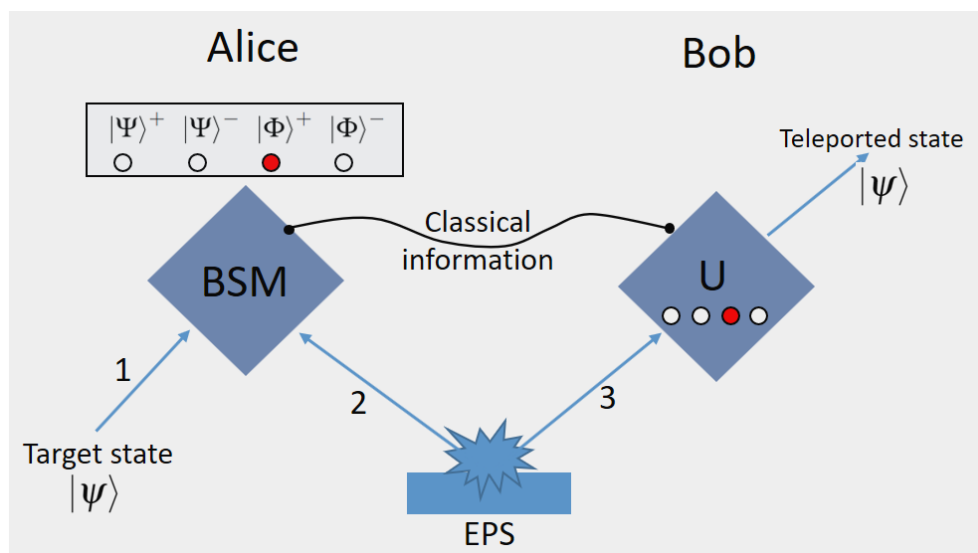


Figure 1.8: Schematic diagram of quantum teleportation. EPS: entangled photon source, BSM: Bell state measurement,

the quantum state at one location gets destroyed and exactly same state is recreated at a different location, with the help of shared entanglement. The basic setup is shown

in Figure 1.8. The quantum teleportation requires entangled photon pair, projective measurement, and exchange of 2-bit of classical information. Consider Alice wants to send state $|\psi\rangle$ of photon 1, to Bob who is at a distant location. A third party, Charlie, creates an entangled photon pairs (photons 2 and 3) and sends photon 2 to Alice and photon 3 to Bob. Alice then performs a Bell state measurement (BSM) on photon 1 and 2. She stores the results in two classical bits and sends it to the Bob via classical channel. Bob then applies unitary operation on photon 3 according to the state of classical bits he has received from Alice. At the end of the protocol, the state of photon 3 becomes $|\psi\rangle$ which is the same quantum state as photon 1. Thus Alice has successfully teleported her quantum state of photon to Bob.

1.6.2 Entanglement swapping

Entanglement swapping is the extended version of quantum teleportation [62, 64]. It involves the teleportation of the entangled state between two photons that has never interacted in the past. Let's consider two entangled photon pairs, 1-2 and 3-4, which are created independently from two different sources. The aim is to swap the entanglement from photon pairs 1-2 and 3-4 to the photon pairs 1-4 and 2-3. The experimental setup is shown in Figure 1.9. Say Alice and Bob are in possession of entangled photon pair 1-2 and 3-4 respectively. A third party, Charlie, will select one photon from each entangled pair, say photons 2 and 3, and perform Bell state measurement (BSM) on them, which ensures the entanglement between photon 2 and 3. This will project photons 1 and 4 onto an entangled state without any interaction. The most difficult task of this protocol is the success of BSM. It requires precise timing of the two photon pairs for synchronization. After performing the BSM on two independent photons 2 and 3, Charlie can allow Alice and Bob to share their entangled pair 1 and 4 that never interacted in the past. The entanglement swapping is an important ingredient of

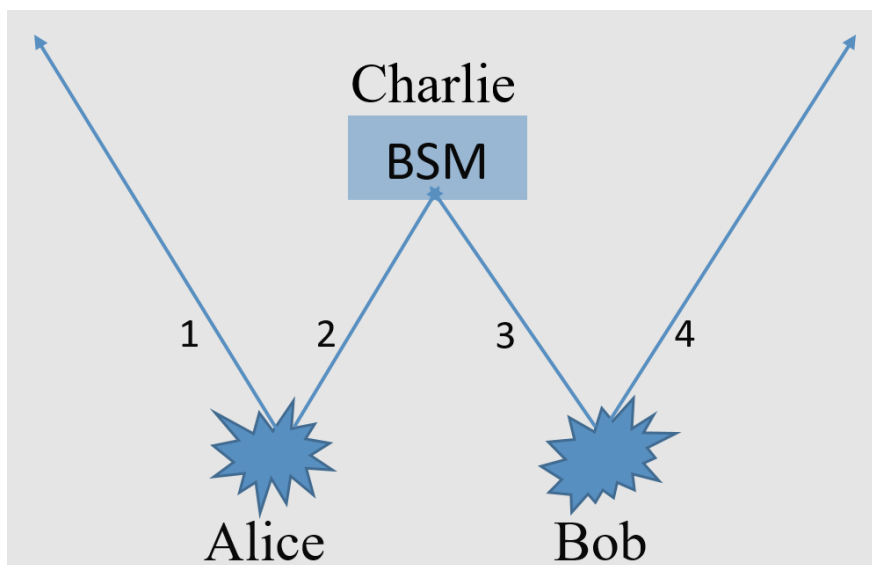


Figure 1.9: Schematic diagram of entanglement swapping

quantum repeaters which is used to connect the quantum computers with each other via swapping.

1.6.3 Superdense coding using entangled state

Superdense coding is the secure protocol which allows Alice to send two bits of classical information to Bob by only transmitting a single qubit [65, 66]. Superdense coding is the flipped version of quantum teleportation. Teleportation transmits single qubit using two bit of classical information whereas superdense coding transmits two bit of classical information using single qubit. One can send 2^n number of classical bits by using n-qubit of quantum communication. In this protocol,

- Charlie first prepares a two-qubit entangled state $|\Phi^+\rangle$:

$$|\Phi^+\rangle = \frac{1}{\sqrt{2}} (|0\rangle_A |0\rangle_B + |1\rangle_A |1\rangle_B)$$

He then sends one qubit to Alice and another to Bob. Here Alice and Bob are at

two completely different locations.

- Alice then encodes the desired two bit of classical information on her qubit by applying a set of quantum gates (Hadamard gate and CNOT gate) to her qubit. As a result, the Bell state $|\Phi^+\rangle$ will transform into any of the four Bell states ($|\Phi^\pm\rangle$ and $|\Psi^\pm\rangle$). She will assign classical two-bit message to each Bell state.
- After performing the desired quantum gate operation, Alice sends her qubit to Bob. After receiving Alice's qubit, Bob performs appropriate measurement on both the qubits (A and B) to decode the Alice's message.

The quantum communication using superdense coding is secure because even if any eavesdropper intercepts the qubit sent by Alice to Bob, he will not be able to extract information from it. Because of the property of entanglement, the measurement performed on individual qubit by eavesdropper gives completely random information which is of no use. This is the major reason to use entanglement-based quantum key distribution protocols.

1.6.4 Entanglement-based quantum cryptography

Quantum cryptography uses the fundamental laws of quantum physics to detect the presence of any eavesdropper when sharing a confidential information between two parties [67–69]. It is the process of encrypting and protecting the information in such a way that only the person who has the secret key can decrypt it. Secret key is the series of random numbers which is used to encrypt the confidential message so that no eavesdropper can decode it except the two parties who shared the secret key. The process of sharing the secret key between two parties in a secure way is known as quantum key distribution (QKD). Broadly, in terms of quantum system, there are two

types of QKD protocols: prepare and measure based QKD such as BB84 protocol and quantum entanglement-based QKD protocol such as E91 protocol [70] and BBM92 protocol [68]. One of the main drawback of BB84 protocol is that Alice has to prepare a string of pure random numbers by herself and protect it against eavesdropper until Bob received it. Such problems can be overcome by using an entanglement based QKD protocol because randomness is inherent in the entangled state.

1.7 Objective of Thesis

Entangled photon sources have been used to perform many quantum information protocols. Spontaneous parametric down-conversion process emerged as one of the best method to generate entangled photon source. The photon pairs generated through SPDC process are indistinguishable and maintained a quantum correlation among themselves in different DoFs which leads to the quantum entanglement in those DoFs. The main objective of the thesis is to generate and characterize the quantum entanglement in different degrees of freedom. We have used mainly two DoFs, polarization and orbital angular momentum (OAM) to study quantum entanglement. We have explored many methods for entanglement generation such as HOM based interferometry, Sagnac interferometry etc. We have demonstrated entanglement-based BBM92 protocol over a distance of 200 m to study the effect of atmospheric aerosols on the key rate. We have also studied the higher dimensional entanglement in OAM basis since it increases the information capacity per photon. We have also explored different methods to generate hybrid entanglement. The effect of scattering through ground glass plate on hybrid entangled photon pairs is also investigated.

1.8 Overview of Thesis

The thesis is organized in eight chapters. Chapter 1 is mainly dedicated to understand the basic concepts which will be useful to understand the work described in the upcoming chapters. This chapter introduces the concept of qubit and its measurement, generation and characterization of quantum entanglement and their applications in various quantum information protocols such as quantum teleportation, entanglement swapping, superdense coding, and entanglement based quantum key distribution.

Chapter 2 covers the concepts of indistinguishable photons. Quantum mechanics allows identical particles to lose their individuality completely and become truly indistinguishable. This property of indistinguishability gives rise to exclusive quantum phenomena such as two particle interference. In this chapter, we describe the relationship between indistinguishability and quantum correlations such as quantum interference, quantum entanglement.

Chapter 3, discusses the generation and transformation of polarization entangled Bell states. In this chapter, the concept of quantum logic gate is used to transform the Bell states, which is the essential step to demonstrate superdense coding protocol.

In Chapter 4, we propose a method for calculating the value of Bell-CHSH parameter with only two sets of measurement settings for two qubit entangled states. This leads to optimised use of resources and a much better cost to performance ratio when certifying the amount of entanglement present in the system.

Chapter 5 describes the field implementation of the quantum key distribution protocol using entangled photon pairs. We report the effect of atmospheric aerosols on the key rate obtained with BBM92 protocol, an entanglement-based QKD protocol, over

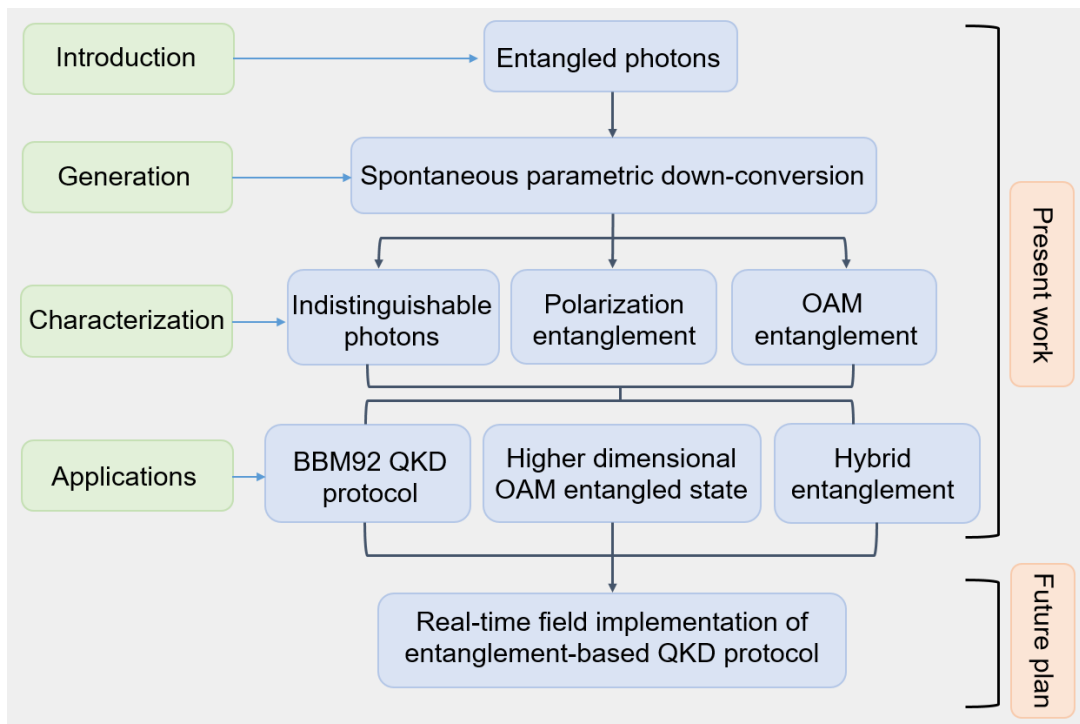


Figure 1.10: Pictorial representation of the layout of the thesis work

200 m distance. We show that concentration and extinction coefficient of atmospheric aerosols play a major role in the observed sift key rate, and eventually, the secure key rate.

In Chapter 6, the generation of high dimensional entanglement is discussed. Controlling the spiral bandwidth of entangled photon pairs via pump shaping is studied. We have shown that how the beam waist of pump mode can affect the bandwidth of OAM spectrum and how it helps to engineer the higher dimensional entanglement.

In chapter 7, the generation of hybrid entanglement between polarization and orbital angular momentum is discussed. In this chapter the effect of scattering media such as ground glass plate on hybrid entangled state is also investigated.

Finally, the summary of the thesis and the future scope are given in chapter 8. A layout of the thesis work is illustrated in Figure 1.10

Chapter 2

Indistinguishable photons and entanglement

A photon is what a photodetector detects.

-Roy Glauber

2.1 Introduction

Photons are characterized by several physical properties, such as their momenta, frequency, polarization etc. These properties can be combined altogether to define the ‘mode’ of the associated electromagnetic field. Two photons are said to be ‘identical particles’ when they cannot be discerned based on such properties. On the other hand, indistinguishability arises from the existence of such identical properties along with the symmetrisation of the wavefunction, which also paves way to entanglement. In a broader sense, this symmetrisation ensures that the states remain identical upon particle interchange. The concept of indistinguishability of particles existed before modern

quantum mechanics. Through his concept of generic phase in the context of statistical equilibrium, Gibbs defined many-particle states where particles possess the same state-independent properties [71, 72]. Such indistinguishable quantum many-particles cannot possess distinct individual states.

The study and quantification of the indistinguishability is of great importance in photon-based quantum information processing towards realising quantum logic gates as well as secure quantum communication [73, 74]. The quality of a single photon source is attributed to its brightness, single photon purity and indistinguishability. For heralded single photons, reduced temporal coherence will result in reduced purity of the output of the Bell State measurement which affects various operations in quantum information processing such as swapping, teleportation etc.

The degree of indistinguishability, usually measured through two photon interference, can get affected by poor spectral, spatial, temporal, or polarization mode overlaps. Source characteristics as well as the interaction with the environment [75] can also deteriorate indistinguishability. Further limitations arise in terms of efficiency as the quest for practical indistinguishable photon sources usually requires some kind of filtering at the origin. In recent years efforts are being made towards obtaining optimal single photon sources with minimal trade-off between efficiency and indistinguishability [76–78]. For applications in quantum networks, it is also important for the source to be optimal in terms of entanglement as well as indistinguishability simultaneously [79–83].

Indistinguishability of photons lies at the heart of key quantum technologies involving photon-based systems. The connection between the mutual coherence of the photons and their intrinsic indistinguishability also provides the connection between the wave particle dualism. In simpler words, indistinguishability gives rise to quantum

interference [84]. The relationship between photon indistinguishability and quantum interference has been established through various which-way experiments [85–88]. Many recent studies use two photon interference for realizing quantum gates as well as quantum computing schemes. Interference of indistinguishable multiphotons is fundamental to advanced and computationally complex problems such as boson sampling [89]. Photon indistinguishability also plays an important role in photon bunching and stimulated emission [90, 91]. Another manifestation of quantum indistinguishability is the generation of random numbers [92]. Indistinguishability has also been studied as a useful quantum feature where entanglement in spatially overlapping identical particles realizes many quantum information protocols [93]. Further studies explore quantum indistinguishability to be used as a controlling feature for noise-free entanglement generation [94]. Another implication of quantum indistinguishability is the property of dualism in the entanglement of identical particles [95]. This property could be utilized as a test for indistinguishability unaffected by the mutual interaction of the particles. In quantum networks, indistinguishability can be used to characterize entanglement as well as identify any compromises in the communication channel due to eavesdropping. The preservation of photon indistinguishability after transmission could verify the quality of entanglement preservation as well as the security of the channel.

2.1.1 Composite systems and identical particles

For composite, compound, or multipartite systems, the quantum state consists of two or more subsystems. Consider a simple case consisting of many two-level subsystems such as multi-qubits. The dimensionality of the total system is defined as $N = 2^n$ where n refers to the number of subsystems each of which belongs to a Hilbert space, $\mathcal{H}_i (i \in n)$. The total state belongs to a Hilbert space defined by the tensor product of the subsystem-Hilbert spaces. These subsystems are termed distinct if they belong

to different Hilbert spaces. These subsystems could be spatially separated particles where local operations such as preparation or measurement of the individual subsystems are possible. It is important to note that these subsystems need not necessarily be spatially separated particles, but could as well be different degrees of freedom of a single quantum system. The hybrid entanglement of polarization and orbital angular momentum (OAM) of a single photon is an example to such systems. A general multipartite system where these subsystems could be represented by the same Hilbert space would form identical particles.

2.1.2 Bosons and fermions

Identical particles have the same intrinsic properties. The lack of individuality makes distinct identification impossible. Any measurement will treat all the subsystems the same way and observable properties will remain invariant under permutations of the particle labels that we associate to them. In other words, symmetric or anti-symmetric invariance over particle permutations underlies quantum indistinguishability. In addition, the indistinguishability gives rise to a fundamental limitation on certain states in being physical and realizable [96]. As an example, consider the case of two identical particles, where ψ_m and ϕ_n form the complete orthonormal basis for particles labelled by ψ and ϕ ,

$$\Psi = \psi_m \phi_n \quad (m \neq n). \quad (2.1)$$

This state is different and orthogonal to the state, $\Psi' = \phi_m \psi_n$, obtained by merely changing the labels of the subsystems. However, states such as,

$$\psi_m \phi_m \quad (2.2a)$$

$$\frac{1}{\sqrt{2}}(\psi_m \phi_n + \phi_m \psi_n) \quad (m \neq n) \quad (2.2b)$$

$$\frac{1}{\sqrt{2}}(\psi_m\phi_n - \phi_m\psi_n) \quad (m \neq n) \quad (2.2c)$$

are not forbidden since they are invariant under the permutation of particle labels. This further implies that only symmetric (Eq. 2.2b) or antisymmetric state vectors (Eq. 2.2c) are allowed for identical particles [97, 98]. The particles with the symmetric state vectors are bosons and the ones with the antisymmetric state vectors are fermions.

2.2 Sources of indistinguishable photons

2.2.1 Non-linear crystal based sources

The need for scalability of quantum information processing demands bright sources of indistinguishable single photons. Since photons do not interact with each other, one needs to look for efficient sources which produces indistinguishable single photons. The easier and efficient way to generate them is within non linear crystals. The most common way to generate identical photons is through the spontaneous parametric down-conversion (SPDC), where two lower energy photons (signal and idler) are generated when a higher energy pump photon is incident on a $\chi^{(2)}$ non-linear crystal. The SPDC process is well explained in Chapter 1 (Section 1.4.1).

2.2.2 Solid-state sources

While parametric down-conversion is usually the first choice of experimentalists in efficiently generating indistinguishable photons, such systems lack control over the arrival time of photons and hence it becomes difficult to perfectly overlap the incoming photons interferometrically. This lack of photon purity due to the probabilistic nature of generation forms a hurdle in achieving high bright sources from such systems.

On the other hand, a two-level single emitter system can emit on-demand photons. Due to the inherent single-photon behaviour, such deterministic sources can be used to generate ultrabright sources without affecting the purity of single photons. While atoms, molecules and ions were explored as single emitters in the early days, epitaxial quantum dots have been extensively investigated in the past decade [99–102].

Quantum dots (QDs) exhibit quantum confinement in all three dimensions of space. They are more prominent in semiconductors because of the energy gap in their electronic band structure. QDs generate a size dependent emission wavelength, narrow emission peak and broad excitation range [103]. After excited by a laser pulse, the system returns to the ground state emitting a cascade of photons. For a given emission energy, strong Coulomb interaction ensures that only a single photon is emitted. Keeping QD in a cavity increases the local density of electromagnetic modes and enhances the generation efficiency.

It is important to note that when strong excitations are used to obtain bright sources, many carriers are generated in the QD which further leads to dephasing and reduction in indistinguishability. In addition, decoherence due to the interaction of the QD with the solid state environment will lead to loss of indistinguishability [104]. However, over the past two decades, semiconductor quantum dots have proven to be promising sources of bright indistinguishable single photons [73, 105–109].

2.3 Quantifying indistinguishability

Many recent works have carried out the estimation of indistinguishability through quantum interference schemes [110–112]. The two photon interference is proved to be a great tool to characterize single photon sources as well as to verify the particle indistinguishability. However, such laborious interference experiments could be avoided

by alternate methods to estimate indistinguishability, such as through the second order correlation function ($g^{(2)}$) in the case of heralded single photon sources [113].

2.3.1 Hong-Ou-Mandel interference

The Hong-Ou-Mandel (HOM) interferometer is of great interest in studying fundamental quantum phenomena as well as in practical applications in quantum information processing. Consider the simple case of two photon interference [12], which is a pure quantum phenomena that results from the quantum exchange of two indistinguishable particles at the splitter. The Hong-Ou-Mandel outcome can also reveal whether the quantum statistics of the identical particles are of bosons or fermions[114]. An illustrative diagram of a simple 2x2 HOM interferometer with two input ports and

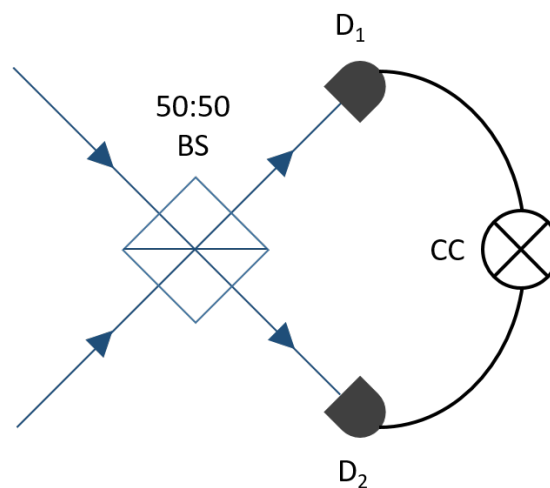


Figure 2.1: The two photon interference (HOM) setup. When a photon enters the input port of an ideal 50:50 beam splitter, it chooses between the reflective or transmissive output ports. The coincidences between the output detectors D_1 and D_2 are recorded through a coincidence counting (CC) electronics.

two output ports is given in Figure 2.1. For a simple 50:50 beam splitter, the transition

matrix is given by the Hadamard operator,

$$U = \frac{1}{\sqrt{2}} \begin{pmatrix} 1 & 1 \\ 1 & -1 \end{pmatrix} \quad (2.3)$$

and the input state is given by, $|\psi_{\text{in}}\rangle = a_1^\dagger a_2^\dagger |00\rangle$, where a_i^\dagger is the creation operator corresponding to each input port. Applying the Hadamard operation for the action of the beam splitter, the output state can be written as,

$$\begin{aligned} |\psi_{\text{out}}\rangle &= \frac{1}{2} (b_1^\dagger + b_2^\dagger) (b_1^\dagger - b_2^\dagger) |00\rangle \\ &= \frac{1}{2} \left[(b_1^\dagger)^2 - b_1^\dagger b_2^\dagger + b_2^\dagger b_1^\dagger - (b_2^\dagger)^2 \right] |00\rangle \\ &= \frac{1}{2} \left[(b_1^\dagger)^2 - (b_2^\dagger)^2 - [b_1^\dagger, b_2^\dagger] \right] |00\rangle. \end{aligned} \quad (2.4)$$

where b_i^\dagger is the creation operator corresponding to each output port of BS. For identical particles, this reduces to,

$$|\psi_{\text{out}}\rangle = \frac{1}{2} (|20\rangle - |02\rangle). \quad (2.5)$$

The action of a beam splitter sends an incident photon to the reflected or transmitted

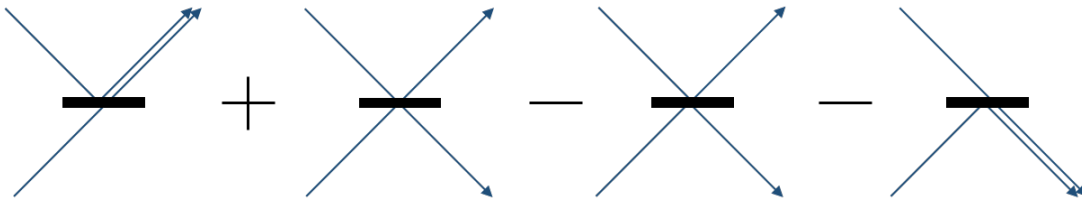


Figure 2.2: The state of the system after interference is given by a superposition of all the four possibilities that occur when two photons enter the beam splitter from its two input ports.

port. When two photons are incident on the two input ports of an ideal 50:50 beam splitter, there are four possibilities in which the two photons can exit the splitter. The state of the system after interference will be a linear superposition of all the possi-

bilities as given in Figure 2.2. The negative signs arise as a phase difference of π is experienced upon reflecting off from a surface of higher index of refraction. When it comes to identical photons, both the photons exit through the same output port together. Given that their wave packets perfectly overlap, the possibilities that they exit through different ports is prevented by quantum mechanics. When the interfering photons are indistinguishable, we observe zero coincidence between the detectors corresponding to the output ports of the interferometer. This is referred to as the HOM dip

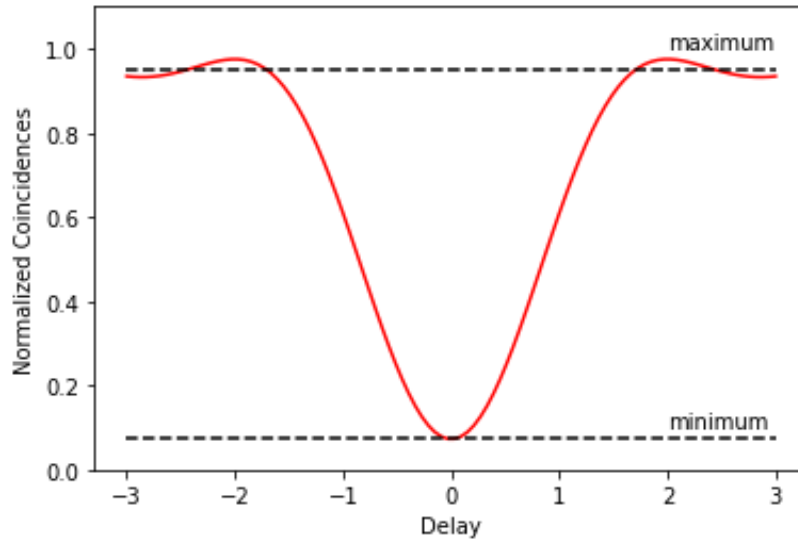


Figure 2.3: The HOM dip obtained when minimum coincidences are recorded between the output ports of the beam splitter. The delay is introduced between the two input ports reducing the indistinguishability and thereby deteriorating the interference.

as given in Figure 2.3. As we introduce path delay between the two photons, they become distinguishable and coincidences begin to be observed between the output ports.

The visibility of the HOM curve is given as,

$$\begin{aligned}
 V &= (N_{dist} - N_{indist})/N_{dist} \\
 &= (N_{max} - N_{min})/N_{max}
 \end{aligned}
 \tag{2.6}$$

where N_{dist} (N_{max}) and N_{indist} (N_{min}) stands for coincidence counts corresponding to distinguishable and indistinguishable scenarios respectively.

2.3.2 Experimental setup and results

The experimental setup for bi-photon interference is shown in Figure 2.4. Horizontally

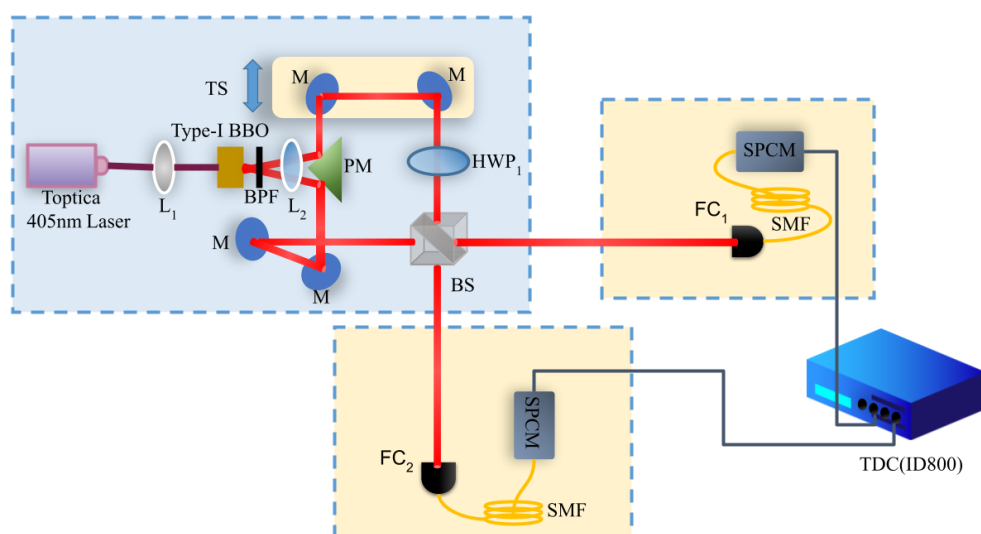


Figure 2.4: Experimental setup for the bi-photon interference using Type-I BBO crystal. L_1 , L_2 : lens, BPF: band pass filter, PM: prism mirror, TS: translation stage, M: mirror, HWP: half-wave plate, BS: beam splitter, FC: fiber coupler, SMF: single mode fiber, SPCM: single photon counting module

polarized UV diode laser (Toptica Topmode) of wavelength 405 nm is used to pump the Type-I β -barium borate (BBO) non-linear crystal. A plano convex lens (L_1) is used to focus the beam inside the center of the crystal. The crystal creates two down-converted photons, signal and idler, of wavelength 810 nm each. A band pass filter 810 ± 5 nm is used just after the crystal to block the pump beam and pass down the signal and idler photons. Both the photons are then separated in two different directions with the help of prism mirror and again combine at the 50:50 beam splitter (BS). The output port of BS is connected to two fiber couplers (FC_1 and FC_2). The FC ($f = 4.6$ mm) is used to

couple the down-converted photons into the single mode fiber (SMF). The SMFs are connected to the single photon counting modules (SPCM-AQRH-16-FC, Excelitas). Both the SPCMs are then connected to a coincidence counter (CC) (IDQuantique-ID800) to measure the number of correlated photon pairs.

Inside the interferometry, a translation stage (TS) is kept in one of the input arms of the BS to ensure temporal indistinguishability. One half-wave plate (HWP_1) is also kept in one of the arms to ensure polarization indistinguishability. First we ensure that both the photons, signal and idler, are identical in all degrees of freedom. We kept the angle of HWP_1 in such a way so that both the photons have same polarization. We recorded the number of correlated photon pairs by moving the translation stage (TS). The TS allows us to match the path length of signal and idler photons so that they become temporally indistinguishable. Figure 2.5 shows the number of coincidence counts as a function of relative delay (ΔL) between signal and idler. As expected,

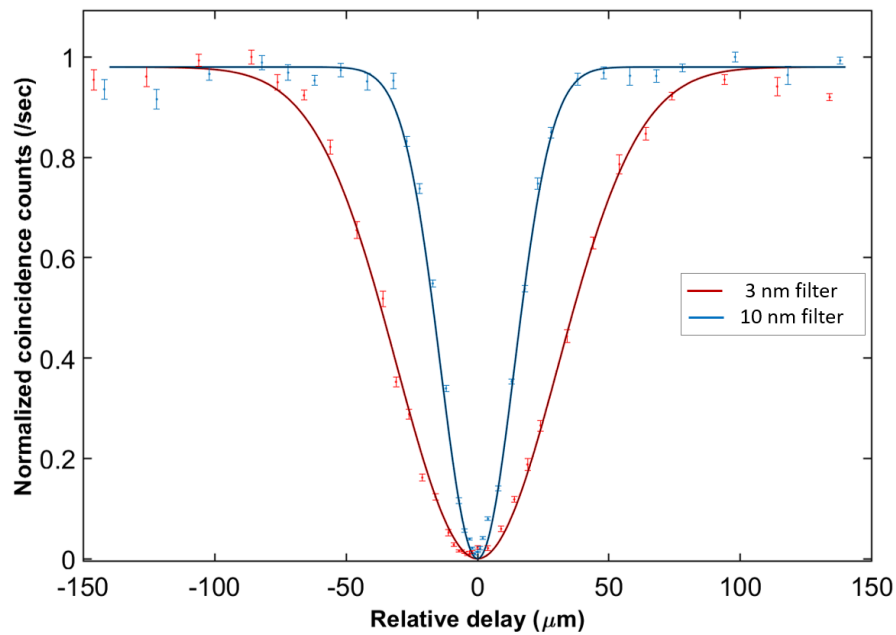


Figure 2.5: HOM dip for 3 nm and 10 nm band pass filter (BPF). FWHM of dip for 3 nm filter is wider than the 10 nm filter because of the large coherence length

we recorded the minimum coincidence counts for $\Delta L = 0$ and maximum coincidence counts for $\Delta L \geq L_c$ where L_c is the coherence length of down-converted photons. The full-width at half maximum (FWHM) of the HOM dip is the coherence length of down-converted photons and it is inversely proportional to the FWHM of the band pass filter $L_c \propto 1/\Delta\lambda$ as evident in Figure 2.5. The experimentally observed FWHM of the dip for 3 nm filter and 10 nm filter is $(146 \pm 2) \mu\text{m}$ and $(68 \pm 2) \mu\text{m}$ respectively. The visibility of the HOM dip for 3 nm and 10 nm is 99.13% and 98.90% respectively.

We also recorded the data for polarization mismatch between signal and idler. We first kept the translation stage at dip region i.e. $\Delta L = 0$ and then we started changing the polarization of one photon with the help of HWP₁. Figure 2.6 shows the number of coincidence counts as a function of HWP₁ angle θ (rotated polarization state). It is

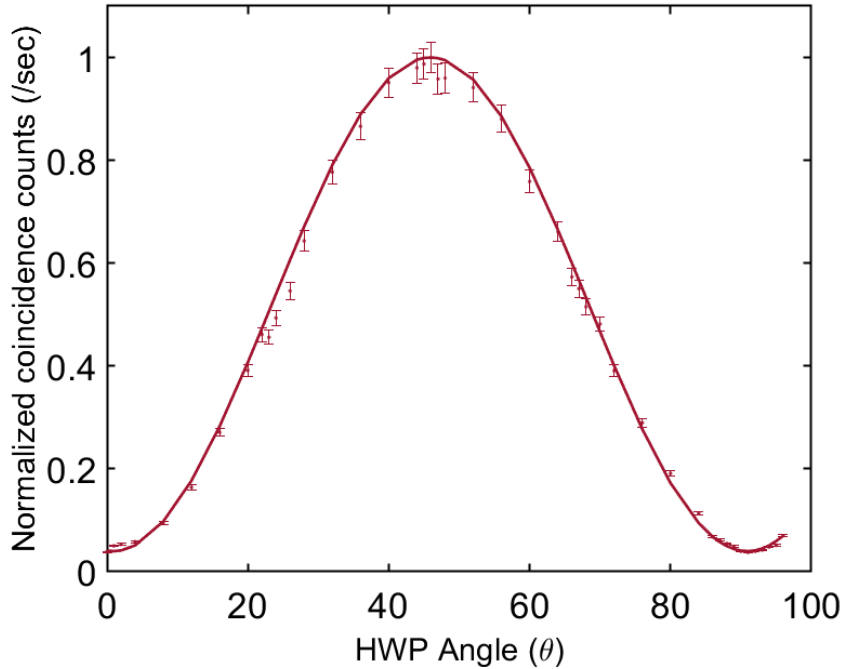


Figure 2.6: Variation of coincidence counts at $\Delta L = 0$ as a function of HWP angle θ . Minimum coincidence counts are registered when both the photons have same polarization ($\theta = 0^\circ$, and 90°) and Maximum counts are registered for orthogonally polarized photon pairs ($\theta = 45^\circ$)

evident from the Figure 2.6 that even if both the photons are temporally indistinguishable, which means that both the photons are combining at the beam splitter (BS) at the same time, we can get the maximum counts if we distinguish them in another degree of freedom. Figure 2.6 shows that when both the photons have same polarization, the coincidence count is minimum and for orthogonal polarization the coincidence count is maximum (where $\Delta L = 0$). This shows that bunching effect happens only when both the photons are perfectly indistinguishable in all degrees of freedom.

2.4 Indistinguishability and entanglement

The identical particle systems and entanglement are two crucial constituents of applied quantum mechanics. In quantum information applications, entanglement is considered as an operational tool to realize protocols in distant locations. However, the extraction of entanglement was seen to be facing a wall when the spatial modes of the identical particles are constricted into a single spatial mode. In order to utilize such systems of indistinguishable particles, e.g. the spin squeezed states of Bose-Einstein condensates, the entanglement could be extracted into the independent modes of the system [115, 116]. This is achieved by a transfer of entanglement from the internal to spatial degrees of freedom of the system of indistinguishable particles [117]. Further studies based on particle statistics investigate the discrimination of indistinguishable particles as well as explore entanglement in such systems [118–120].

2.4.1 Entanglement duality

An interesting outcome of the complementarity in indistinguishable systems is the entanglement duality. A bipartite system of photons, entangled in two degrees of their freedom A and B , belongs to a single vector space spanned by the tensor product of the

Hilbert spaces corresponding to two particles. We need two variables to meaningfully describe the state of a bipartite entangled state. While one of the variables, A , is used to label the particles, entanglement is observed in the other variable, B , where $[A, B] = 0$. Duality of entanglement states that it is not possible to observe the entanglement in one variable of two indistinguishable particles, unless they are separated in terms of another variable [95]. Consider the two photon state

$$|\Psi\rangle_{(A_1, A_2, B_1, B_2)} = (c_1 \alpha_{A_1, B_1}^\dagger \alpha_{A_2, B_2}^\dagger + c_2 \alpha_{A_1, B_2}^\dagger \alpha_{A_2, B_1}^\dagger) |0\rangle, \quad (2.7)$$

where $\alpha_{A_1, B_1}^\dagger$ is the creation operator that takes the state $|0\rangle$ to the joint state $|B_1\rangle_{A_1}$. After the action of the creation operator, the state could be written as

$$\begin{aligned} |\Psi\rangle_{(A_1, A_2, B_1, B_2)} &= \alpha |B_1\rangle_{A_1} |B_2\rangle_{A_2} + \beta |B_2\rangle_{A_1} |B_1\rangle_{A_2} \\ &= \alpha |A_1\rangle_{B_1} |A_2\rangle_{B_2} + \beta |A_2\rangle_{B_1} |A_1\rangle_{B_2}. \end{aligned} \quad (2.8)$$

The property of entanglement duality has been verified for different degrees of freedom of photons [121–124]. Here we are considering polarization and orbital angular momentum (OAM) degrees of freedom.

2.4.2 Entanglement in polarization and orbital angular momentum

Entanglement is one of the most fascinating phenomena in quantum theory. It arises due to the non-separability of the sub-systems involved. SPDC generates twin photons entangled in different DoF. In particular, their entanglement in polarization as well as orbital angular momentum (OAM) are the most extensively studied and widely used in various quantum information protocols. In Type-II SPDC process, the generated down-

converted photons are independently entangled in polarization and OAM degrees of freedom. Consider the collinear case where $k_p = k_s = k_i = k$, the output state of SPDC process can be written as

$$|\Psi\rangle_{\text{SPDC}} = \frac{1}{\sqrt{2}} (|H, m_1\rangle_s |V, m_2\rangle_i + |V, m_1\rangle_s |H, m_2\rangle_i) \quad (2.9)$$

where m_1 and m_2 is the orbital angular momentum of signal and idler photon respectively. The SPDC process follows the OAM conservation law which means that sum of the OAM of signal and idler must be equal to the OAM of pump photon *i.e.* $m_p = m_s + m_i$.

The down-converted photons are indistinguishable in every other degree of freedom, including spatial position and momentum, except in polarization and OAM. To observe the entanglement in any degree of freedom, one has to perform the individual measurement on these photons. However, for two indistinguishable photons that are propagating along the same direction, it becomes impossible to perform individual measurements unless we sort and separate them under some distinguishing label. Separating the photons in one degree of freedom reveals the entanglement in the other. Separation of signal and idler in one degree of freedom means that we distinguish them in that degree of freedom and distinguishability destroys the entanglement in that particular degree of freedom. Duality in the entanglement of identical particles manifests that entanglement in only one variable can be revealed at a time. We demonstrate this using OAM and polarization variables of indistinguishable photons generated from collinear type II parametric down-conversion. We show polarization entanglement by sorting photons in even and odd OAM basis, while sorting them in two orthogonal polarization modes reveals the OAM entanglement. This method increases the efficiency of available entangled photons since we are not eliminating any photons from the gen-

erated output. After sorting the Eqn. 2.9 in polarization and OAM, it can be rewritten as,

$$|\Psi\rangle_{\text{SPDC}} = \frac{1}{\sqrt{2}} \left(|H\rangle_{m_1} |V\rangle_{m_2} + |V\rangle_{m_1} |H\rangle_{m_2} \right) \quad (2.10)$$

$$= \frac{1}{\sqrt{2}} (|m_1\rangle_H |m_2\rangle_V + |m_2\rangle_H |m_1\rangle_V) \quad (2.11)$$

In most protocols involving the entanglement of orbital angular momentum of photons, the infinite dimensional OAM spectrum in the output of SPDC is restricted to a two dimensional basis by the post-selection of the twin-photons. Due to this post-selection, a large amount of generated photons which belong to the other states in the infinite dimensional OAM basis are lost. A method to avoid this loss is to use an alternate basis defined by the even and odd states of OAM.

In this work, we propose that the OAM of twisted photons defined in their even-odd basis can be used to separate the otherwise completely indistinguishable photons in the collinear output. For a pump beam carrying an odd OAM value, the SPDC photons will be generated in pairs of even and odd OAM states, following the conservation of OAM.

For pump OAM, $m_p = 1$, in a collinear Type-II SPDC process where the idler-signal pairs are generated in orthogonal polarization states, the output OAM state can be written as:

$$\begin{aligned} |\Psi\rangle_{\text{SPDC}} &= \sum_{m_s=-\infty}^{+\infty} C_{m,1-m} |1\rangle_H |1-m\rangle_V, \\ &= C_{0,1} |0\rangle_H |1\rangle_V + C_{1,0} |1\rangle_H |0\rangle_V + \\ &\quad C_{2,-1} |2\rangle_H |-1\rangle_V + C_{-1,2} |-1\rangle_H |2\rangle_V + \dots, \\ &= \frac{1}{\sqrt{2}} (|E\rangle_H |O\rangle_V + |O\rangle_H |E\rangle_V). \end{aligned} \quad (2.12)$$

2.4.3 Experimental setup and results

The experimental setup to observe the OAM and polarization entanglement is shown in Figure 2.7 and 2.9 respectively. A horizontally polarized laser beam (Toptica Top-mode) of wavelength 405 nm is used to pump the nonlinear Type-II PPKTP crystal. A band pass filter (BPF, 810 ± 5 nm) is used to block the pump while transmitting the down-converted photons. The divergence of SPDC photons are collimated using lens, L_2 . The down-converted photon pairs are entangled in polarization as well as in OAM. The spatial and temporal overlap between signal and idler must be taken care in order to observe the maximum entanglement. In the detection part, fiber couplers (Thorlabs CFC-5X-B) are used to couple the signal and idler photon into optical fiber. These fibers are then connected to the single photon counting modules (SPCM-AQRH-16-FC, Excelitas) to detect the photons. Both the SPCM are then connected to a coincidence counter (CC) (IDQuantique-ID800) to measure the number of correlated photon pairs. We observe the polarization entanglement through OAM sorting and OAM entanglement through polarization sorting.

A. Observation of OAM entanglement through polarization sorting

The experimental setup to observe the OAM entanglement while sorting them in polarization is given in Figure 2.7. We used spiral phase plate (SPP) of order $m = 1$ in the input pump so that pump beam can carry an OAM of order 1. A polarizing beam splitter (PBS) is used to separate the horizontal (H) and vertical (V) polarized photon in transmitted and reflected port as shown in Figure 2.7. OAM measurements are performed with the help of phase flattening technique using combination of spatial light modulator (SLM) and single mode fiber (SMF). The crystal plane is imaged onto the

SLM kept in each arm of the PBS using two lens combination L_2 and L_3 . Again, both the SLM plane are imaged onto the fiber coupler for efficient coupling.

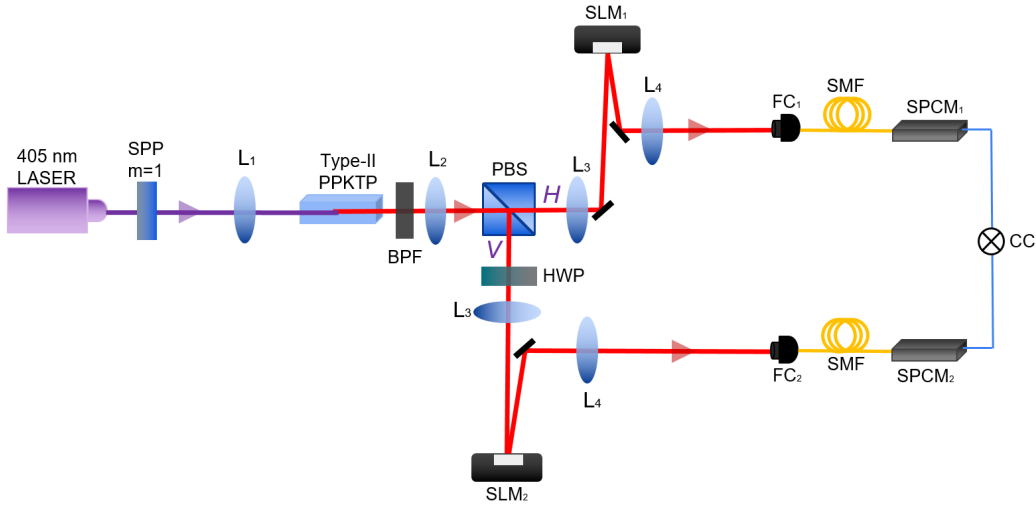


Figure 2.7: Schematic to observe entanglement in the even-odd basis of OAM by sorting photons in polarization. Indistinguishable photons in the Type-II down-converted pairs are sorted in polarization using a polarizing beam splitter (PBS).

Figure 2.8 shows the experimental data of OAM correlation in even-odd basis between H and V output port of PBS. The hologram displayed in the SLM corresponding to the superposition of even and odd OAM order acts a diagonal (D_{EO}) and anti-diagonal (A_{EO}) projections. The indistinguishable photons are efficiently sorted under the label of their polarization degree of freedom and OAM entanglement visibility is observed in both E/O as well as D_{EO}/A_{EO} basis. The normalized coincidences are plotted along y-axis with the variation of θ_2 for $\theta_1 = 0^\circ$ (blue), $\theta_1 = 45^\circ$ (red), $\theta_1 = 90^\circ$ (green), and $\theta_1 = 135^\circ$ (purple). A calculation of visibility gives $92.7 \pm 0.3\%$ (E/O basis) and $80.9 \pm 0.3\%$ (D_{EO}/A_{EO} basis). The Bell parameter is estimated to be, $S = 2.46 \pm 0.08$.

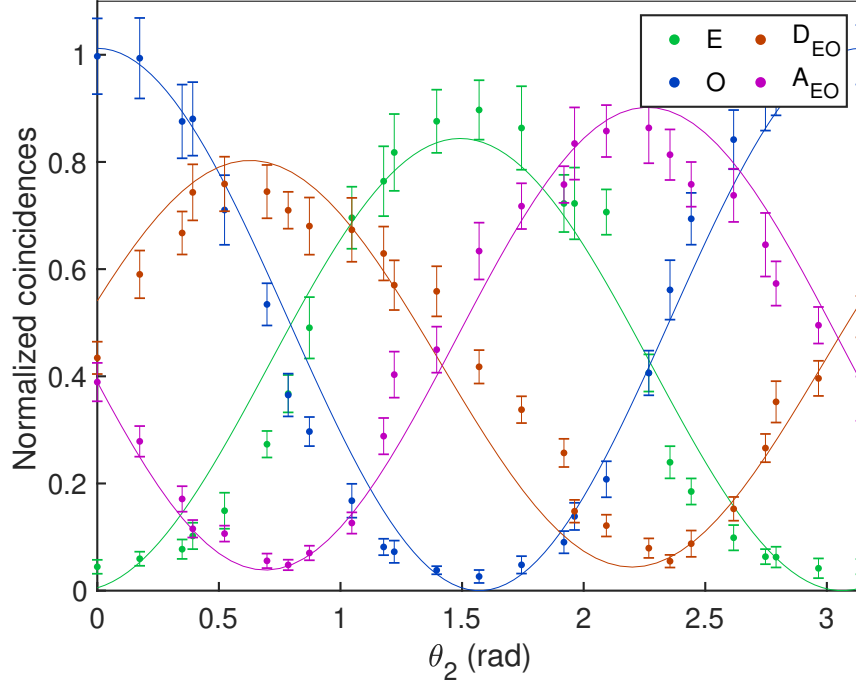


Figure 2.8: OAM correlations corresponding to two orthogonal polarization projections in the collinear SPDC output. Visibility curves are plotted for V port OAM projection angles, $\theta_1 = 0$ (E - green dot), $\theta_1 = \pi/4$ (D_{EO} - red dot), $\theta_1 = \pi/2$ (O - blue dot) and $\theta_1 = 3\pi/4$ (A_{EO} - purple dot). θ_2 is the H port OAM projection angle. Solid curves are respective cosine fits. Error bars indicate statistical uncertainty of one standard deviation.

B. Observation of polarization entanglement through OAM sorting

In this case, we sort the even and odd OAM basis of the signal and idler photon in order to observe the entanglement in polarization. For OAM sorting, we used the double Mach-Zehnder OAM sorting interferometry to separate the photon in even/odd OAM basis. The experimental setup is shown in Figure 2.9. A double Mach-Zehnder type interferometer could be understood as a normal Mach-Zehnder interferometer, folded back such that the input and output beam splitters become the same. Such a configuration will have the stability of a common path interferometer, since both the arms see same optical components, and the ease of inserting independent components in the

interfering arms as in a Mach-Zehnder interferometer. The collinear correlated pairs of photons having even and odd OAM orders are sent to a double Mach-Zehnder interferometer containing two Dove prisms which are kept in the individual paths as given in Figure 2.9. A dove prism flips the OAM from $+m$ to $-m$ during the internal reflection.

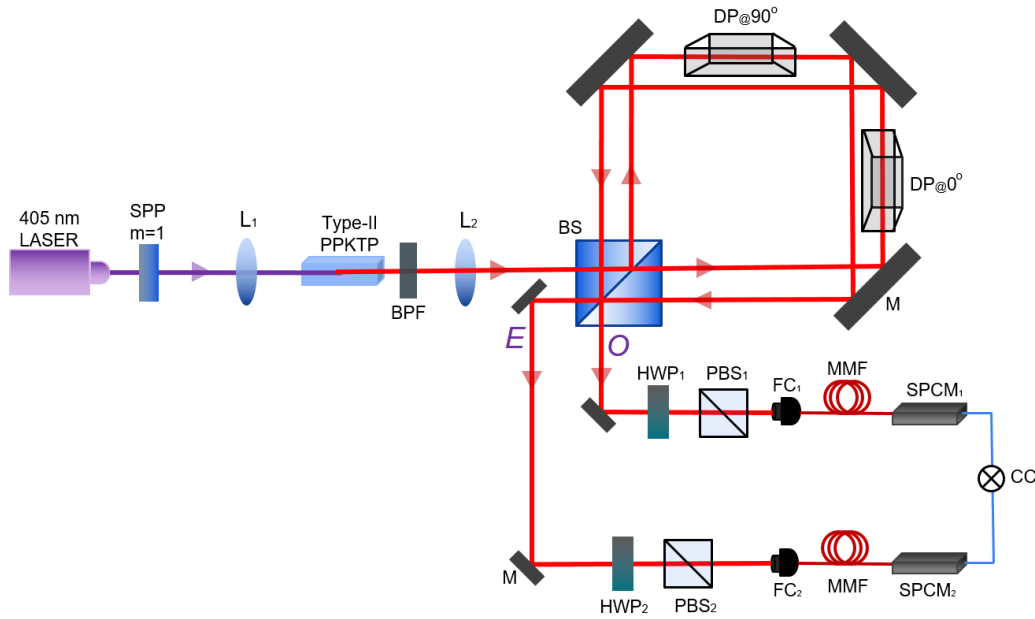


Figure 2.9: Schematic to sort the even-odd states of OAM from a collinear SPDC with pump carrying OAM ($m_p = 1$). The Dove prisms within the double Mach-Zehnder interferometer is kept orthogonal to each other. Half wave plate (HWP) along with polarizer (P) corresponds to the polarization projectors. O refers to the constructive port for odd OAM and E labels the constructive port for even OAM.

When two Dove prisms are kept in the two arms of an interferometer, it introduces an OAM dependent relative phase, $2m\alpha$, where α is the relative rotation of the Dove prisms. Since two Dove prisms are oriented perpendicular to one another, therefore, $\alpha = \pi/2$. This introduces a phase $m\pi$ between the two arms of the interferometer. The relative phase difference would turn out to be $m\pi$ for E output port of the BS (Even port) and $(m+1)\pi$ for O port of the BS (Odd port). As a result, the constructive interference will take place in different output ports for even and odd OAM values. Photons carrying an odd OAM will constructively interfere in the odd port (O) whereas photons

having even OAM will show up in the even port (E). The polarization projections are done using the combination of HWP and PBS kept in each output port. polarization projection measurements are carried out to observe the entanglement visibility. Before making polarization entanglement measurements on these photons, the action of even-odd sorting within our setup needs to be verified. The OAM state of the photons in the output ports of the sorter are measured using the standard technique involving phase-flattening through SLM and coupling to single mode fibers. The single counts

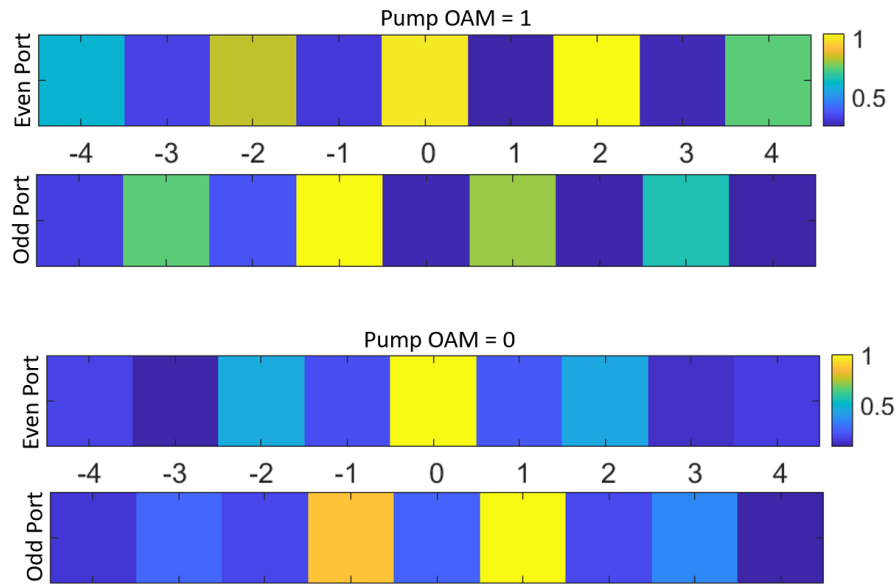


Figure 2.10: Verification of sorting of even and odd OAM states. The top two rows correspond to the singles output in the even and odd ports when pumped with a LG mode of order $m = 1$ and the bottom two rows correspond to that for a pump carrying Gaussian mode. The scale is normalized with respect to the maximum counts.

in each port corresponding to different OAM values are represented in Figure 2.10. When pumped with a Gaussian beam, photons are down converted in pairs of odd-odd or even-even pairs, following the conservation of OAM, and thus the photon pairs end up in the same port. It can be easily seen from the chart that photons carrying even and odd OAM values line up in the corresponding ports and their intensities are defined by the OAM spectrum of the SPDC output. For a pump carrying OAM, $m_p = 1$, the pairs

are generated in even-odd pairs and they go to different ports. This is evident from how the corresponding intensity values are distributed between the two ports. For example, 0 in even port and 1 in odd port show similar intensity since they are generated together and so on. Figure 2.10 shows the effective OAM sorting in the setup. Just after the OAM sorter, a combination of HWP and PBS is kept in each arm for polarization correlation measurement. This time, we used multi-mode fiber (MMF) so that all the higher order OAM modes get coupled into the fiber for the detection. Figure

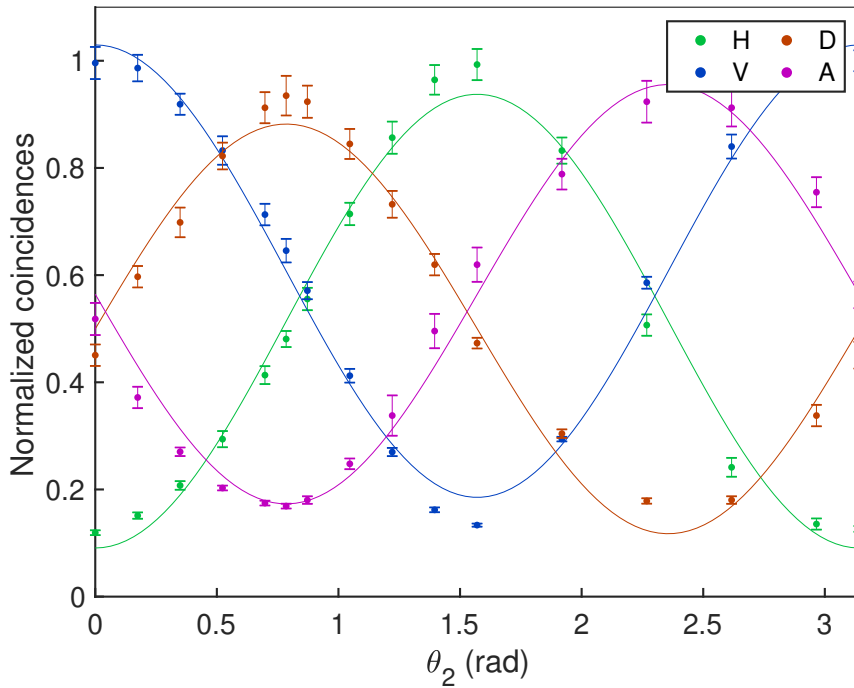


Figure 2.11: Polarization correlations corresponding to projections in the output ports of the even-odd sorted collinear SPDC output. Visibility curves are plotted for odd port polarization projection angles, $\theta_1 = 0$ (H - green dot), $\theta_1 = \pi/4$ (D - red dot), $\theta_1 = \pi/2$ (V - blue dot) and $\theta_1 = 3\pi/4$ (A - purple dot). θ_2 corresponds to even port projections. Solid curves are respective cosine fits. Error bars indicate statistical uncertainty of one standard deviation.

2.11 shows the polarization correlations between the even and odd output ports of the sorter. The indistinguishable photons are efficiently sorted under the label of their orbital angular momentum and polarization correlations are observed in both H/V and

D/A basis. The normalized coincidences are plotted along y -axis with the variation of θ_2 for $\theta_1 = 0^\circ$ (blue), $\theta_1 = 45^\circ$ (red), $\theta_1 = 90^\circ$ (green), and $\theta_1 = 135^\circ$ (purple). The observed visibilities are $77.5 \pm 0.3\%$ (H/V basis) and $71.6 \pm 0.3\%$ (D/A basis). The Bell parameter is estimated to be, $S = 2.11 \pm 0.03$.

It can be seen in the plot that the minima corresponding to different visibility profiles are not going completely to zero. This is due to the use of multi-mode fiber (MMF) instead of single mode fiber (SMF). Since SMF only couples Gaussian mode and in our case, we are using non-zero OAM basis (even/odd) therefore in order to couple all the higher order modes, MMF is required. The reduced visibility can be understood as a phase mismatch among the higher order spatial modes generated in SPDC process collected by the MMF and also the imperfections in the sorting interferometer. Hence, with an improved interferometric sorter and through proper phase compensation between the higher order modes, it is possible to obtain near unity visibility.

2.5 Summary

In this chapter, we have discussed the concept of indistinguishability of photons and entanglement. Photon indistinguishability is a necessity in two photon and multi photon quantum interference, engineering quantum states as well as realizing many quantum information protocols. In quantum interference experiments, the dependence of indistinguishability on the temporal delay between the two photons has been studied. Interference is lost in which-way experiments when the paths of the two photons are made distinguishable. The spatial and temporal indistinguishability between two photons is the necessary criteria for entanglement. We observed that sorting the photon in any degree of freedom destroys the entanglement in that degree of freedom. We

demonstrate the duality in entanglement of a collinear, indistinguishable pair of photons generated in SPDC process. We show polarization entanglement for indistinguishable photons by sorting the photon OAM using a double Mach-Zehnder even-odd sorter. This method can increase the availability of entangled photons since we are not eliminating any photon from the generated output in contrast to the case of limiting them to two-dimensional OAM bases such as $(+m, -m)$ or $(0, m)$. All the down-converted photons are sorted using an even-odd sorter in order to observe the polarization entanglement of otherwise indistinguishable collinear photons. Similarly, we demonstrate OAM entanglement by sorting photons using a simple polarizing beam splitter and executing OAM projections on the photon pairs in the even-odd basis.

Chapter 3

Generation and transformation of polarization-entangled Bell states

God does not play dice with the universe.

-Albert Einstein

3.1 Introduction

Quantum entanglement [8, 23] is one of the most interesting phenomena in quantum world which laid the foundation of many quantum applications such as quantum superdense coding [65, 125], quantum teleportation [22, 60], entanglement swapping [62, 64], and quantum key distribution (QKD) protocols [126]. The simplest way to create an entangled photon pair is spontaneous parametric down-conversion (SPDC) process [50, 127]. In this process, a nonlinear $\chi^{(2)}$ crystal is used to produce two correlated photons. They can be correlated in any degree of freedom such as, polarization, orbital angular momentum (OAM), energy, time, frequency etc. Among these, polar-

ization entangled states are easy to prepare and measure. Hence it is the most widely used resource for all the quantum communication protocols.

A set of all four maximally entangled polarization states in two dimensional Hilbert space are known as Bell states [128]. In many quantum information schemes such as quantum superdense coding, teleportation, and entanglement swapping, the generation and discrimination of all the four maximally entangled states is required. For example, in superdense coding control over basis of maximally entangled state is required. A desired Bell state can be prepared through unitary transformations on an entangled pair of photons generated in SPDC. In this case, transformation of one Bell state into another by using single-qubit gate (Pauli gate) can be used. For example, $|\Psi\rangle^+$ can be transformed into $|\Psi\rangle^-$ and $|\Phi\rangle^+$ with the help of polarization-dependent phase shift (phase-flip) and polarization exchange (bit-flip) respectively. Conventionally, A quarter-wave plate (QWP) (which performs a Pauli-Z transformation) and half-wave plate (HWP) (which performs a Pauli-X transformation) is used for phase-flip and bit-flip respectively [34, 129, 130]. In this work, we show that only a single-half wave plate (HWP) is enough to perform Pauli-X and Pauli-Z transformation, and to perform Pauli-Y transformation, a pair of HWP is required.

This chapter is organized as follows: In section 3.2, we explain the theoretical model of our proposed scheme where we first explain the single qubit gate (Pauli gate) and how these gates are analogous to the rotation of HWP. In section 3.3 we present the experimental setup for both generation and transformation of Bell states. In section 3.4, we discuss the experimental results. We end the paper with concluding remarks in last section 3.5.

3.2 Theory

Consider two photons, signal and idler, are entangled in polarization and propagating along two different directions. Following are four different polarization entangled state,

$$\begin{aligned} |\Psi\rangle^\pm &= \frac{1}{\sqrt{2}}(|H\rangle_s |V\rangle_i \pm |V\rangle_s |H\rangle_i) \\ |\Phi\rangle^\pm &= \frac{1}{\sqrt{2}}(|H\rangle_s |H\rangle_i \pm |V\rangle_s |V\rangle_i), \end{aligned} \quad (3.1)$$

where $|H\rangle$ and $|V\rangle$ are the horizontal and vertical polarization states of photons, respectively. Using Jones vector notation, the polarization states can be represented by column vector,

$$|H\rangle = \begin{pmatrix} 1 \\ 0 \end{pmatrix}, |V\rangle = \begin{pmatrix} 0 \\ 1 \end{pmatrix} \quad (3.2a)$$

$$|D\rangle = \begin{pmatrix} 1 \\ 1 \end{pmatrix}, |A\rangle = \begin{pmatrix} 1 \\ -1 \end{pmatrix}, \quad (3.2b)$$

In Eqn. 3.1, $|\Psi\rangle^-$ is anti-symmetric entangled state and rest are symmetric states. These entangled states are popularly known as Bell states. Using single-qubit quantum logic gate, one Bell state can be easily manipulated and transformed into another Bell state. Such a gate operation transforms input state $|\psi\rangle$ to an output state $|\phi\rangle$ (Figure 3.1). These single-qubit logic gates are X , Y , and Z gate and are analogous to Pauli

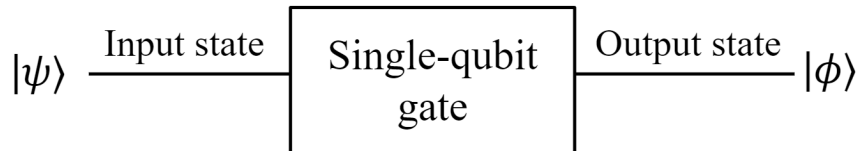


Figure 3.1: Schematic diagram of transformation of state

spin matrices σ_x , σ_y and σ_z . The matrix representation for these gates is given as,

$$I = \sigma_0 = \begin{pmatrix} 1 & 0 \\ 0 & 1 \end{pmatrix}, X = \sigma_x = \begin{pmatrix} 0 & 1 \\ 1 & 0 \end{pmatrix} \quad (3.3a)$$

$$Y = \sigma_y = \begin{pmatrix} 0 & -i \\ i & 0 \end{pmatrix}, Z = \sigma_z = \begin{pmatrix} 1 & 0 \\ 0 & -1 \end{pmatrix} \quad (3.3b)$$

Here, I is the identity gate and it does not change the input state. X gate is known as bit-flip because it flips the state $|H\rangle$ to $|V\rangle$ and vice-versa, whereas Z gate is known as phase-flip because it flips the sign of $|V\rangle$, while leaving $|H\rangle$ unchanged. iY gate is used to flip the bit and phase simultaneously and it can be realized using the property $[\sigma_x, \sigma_z] = 2i\sigma_y$. Hence $\sigma_x\sigma_z = i\sigma_y$ and it is given by,

$$XZ = iY = \begin{pmatrix} 0 & 1 \\ -1 & 0 \end{pmatrix} \quad (3.3c)$$

Now consider our initial state is $|\Psi\rangle^+$ (Eqn. 3.1). Applying Z and X gate operation on signal photon of state $|\Psi\rangle^+$ results $|\Psi\rangle^-$ and $|\Phi\rangle^+$ respectively,

$$Z_s |\Psi\rangle^+ = |\Psi\rangle^- \quad (3.4a)$$

$$X_s |\Psi\rangle^+ = |\Phi\rangle^+ \quad (3.4b)$$

Again, applying Y gate operation on signal photon results $|\Phi\rangle^+$ and $|\Phi\rangle^-$ respectively,

$$iY |\Psi\rangle^+ = X_s Z_s |\Psi\rangle^+ = |\Phi\rangle^- \quad (3.4c)$$

Or one can apply X gate in signal photon and Z gate on idler photon and vice-versa. Hence Y gate operation can also be written as,

$$iY |\Psi\rangle^+ = X_s Z_i |\Psi\rangle^+ = |\Phi\rangle^- \quad (3.4d)$$

These states transformation are illustrated in Figure 3.2. These gates can be exper-

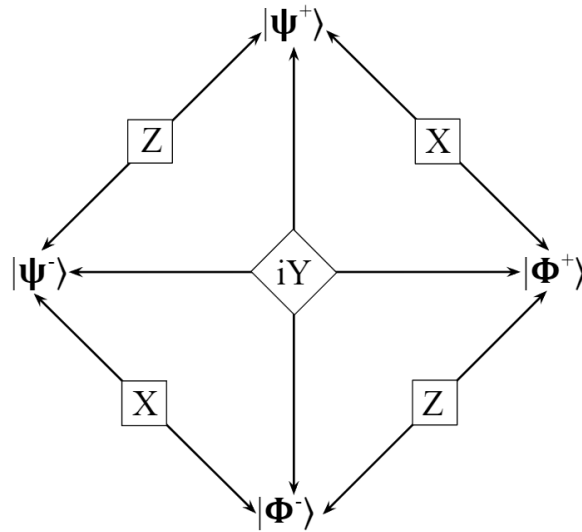


Figure 3.2: Transformation of Bell states using single-qubit logic gates

imentally realized in laboratory by rotating the polarization of photons using HWP. It retards the polarization state of photons by adding a phase difference between the two orthogonal polarization components $|H\rangle$ and $|V\rangle$ and the phase difference depends on wavelength λ of incident photons, birefringence properties (Δn) of the crystal, and thickness d of the HWP:

$$\Delta\phi = \frac{2\pi d \Delta n}{\lambda} \quad (3.5)$$

where Δn is the difference of refractive index along slow axis and fast axis. λ , Δn , and d are chosen in such a way that the phase difference between polarization components

is π . The action of HWP can be represented by Jones matrix notation:

$$\hat{U}_{\text{hwp}}(\theta) = \begin{pmatrix} \cos 2\theta & \sin 2\theta \\ \sin 2\theta & -\cos 2\theta \end{pmatrix} \quad (3.6)$$

where θ is the angle between fast axis and horizontal axis. When the photons of particular polarization transmit through the HWP, the polarization changes according to HWP angle θ . Z and X gate can be realized by aligning the fast axis of HWP at an angle 0° and 45° with respect to horizontal axis. Similarly, Y gate can be realized by using two HWPs at two different angles 0° and 45° .

$$\begin{aligned} \hat{U}_{\text{hwp}}(0^\circ) &= \begin{pmatrix} 1 & 0 \\ 0 & -1 \end{pmatrix} = \sigma_z \\ \hat{U}_{\text{hwp}}(45^\circ) &= \begin{pmatrix} 0 & 1 \\ 1 & 0 \end{pmatrix} = \sigma_x \\ \hat{U}_{\text{hwp}}(0^\circ)\hat{U}_{\text{hwp}}(45^\circ) &= \begin{pmatrix} 0 & 1 \\ -1 & 0 \end{pmatrix} = i\sigma_y \end{aligned} \quad (3.7)$$

Using Eqn. 3.2 and 3.7, we will show that how one can use only HWP to perform all quantum gates,

I. Verification of Z gate:

$$\hat{U}_{\text{hwp}}(0^\circ)|H\rangle = |H\rangle, \quad \hat{U}_{\text{hwp}}(0^\circ)|V\rangle = -|V\rangle, \quad (3.8a)$$

$$\hat{U}_{\text{hwp}}(0^\circ)|D\rangle = |A\rangle, \quad \hat{U}_{\text{hwp}}(0^\circ)|A\rangle = |D\rangle. \quad (3.8b)$$

II. Verification of X gate:

$$\hat{U}_{\text{hwp}}(45^\circ)|H\rangle = |V\rangle, \quad \hat{U}_{\text{hwp}}(45^\circ)|V\rangle = |H\rangle \quad (3.9a)$$

$$\hat{U}_{\text{hwp}}(45^\circ)|D\rangle = |D\rangle, \quad \hat{U}_{\text{hwp}}(45^\circ)|A\rangle = -|A\rangle \quad (3.9b)$$

Eqn. 3.8 shows that apart from QWP, HWP can also be used for phase-flip. Using Eqns 3.8 and 3.9, one can transform Bell states using HWPs only. Table 3.1 shows the transformation of Bell states using HWP.

Input state	Quantum gate	HWP _s	HWP _i	Output state
$ \Psi\rangle^+$	I			$ \Psi\rangle^+$
$ \Psi\rangle^+$	Z	0°		$ \Psi\rangle^-$
$ \Psi\rangle^+$	X	45°		$ \Phi\rangle^+$
$ \Psi\rangle^+$	XZ	0°	45°	$ \Phi\rangle^-$

Table 3.1: Operation of quantum gate and corresponding HWP angles. The gate transforms an input state to an output state.

3.3 Experimental setup

3.3.1 Entangled photon pair generation

Figure 3.3 shows the experimental setup for the generation of polarization entangled Bell state $|\Psi\rangle^+$. Horizontally polarized continuous wave laser (Toptica iBeam smart) of wavelength 405 nm and pump power 2.5 mW is used to pump the nonlinear type-I β -barium borate (β -BBO) crystal of thickness 2 mm and transverse dimensions of 6 mm \times 6 mm with an optic axis oriented at 29.97° to the normal incidence. This will produce two vertically polarized photon pairs of wavelength 810 nm each. A band pass filter (BPF) is used to block 405 nm photons while transmitting the 810 nm photons. Both the photons are separated by prism mirror (PM) in two different arms. Both the photons are again combined at the input port of the 50:50 beam splitter (BS). HWP₁ is used in one of the input arms of beam-splitter (BS) to flip the polarization state of

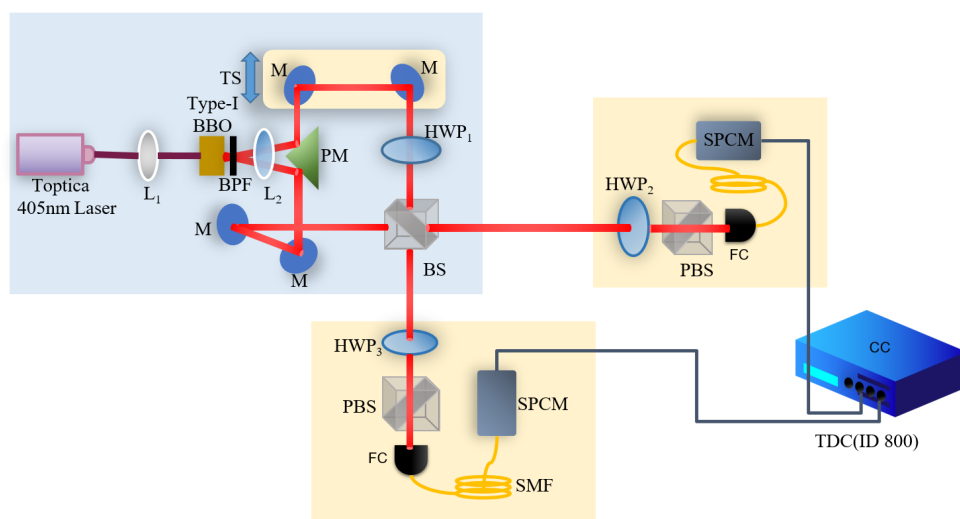


Figure 3.3: Experimental setup for the generation of entangled state $|\Psi\rangle^+$. L_1, L_2 - Lenses, BBO - β -Barium borate crystal, BPF - Band pass filter, PM - Prism mirror, M - Mirror, BS - 50:50 Beam splitter, TS- translation stage, PBS - Polarizing beam splitter, HWP - Half-wave plate, FC - Fiber coupler, SMF - Single mode fiber, SPCM - single photon counting module, CC - Coincidence counter

one photon so that both the photons become orthogonally polarized to each other. A translation stage (TS) is used to compensate the path difference between signal and idler.

For the detection part, we have used combination of HWP and PBS at each output port of BS. After combining at the BS both the photons will exit from two different output ports and get coupled into single mode fiber (SMF) (P1-780A-FC-2, Thorlabs) with the help of fiber couplers (FC) (CFC-5X-B, Thorlabs). These SMFs are connected to the single photon counting module (SPCM) detectors (SPCM-AQRH-16-FC, Excelitas) having a time resolution 350 ps. To measure the number of correlated photon pairs, both the SPCMs are then connected to a coincidence counter (CC), IDQuantique-ID800, having a time resolution of 81 ps. The photon pairs that exit from same output port will not contribute to coincidence counts. This setup can directly produce $|\Psi\rangle^\pm$ state at the output ports of BS by simply adjusting the phase

difference between both the photons.

3.3.2 Transformation of Bell states

Figure 3.4 shows the experimental setup of the transformation of Bell state. First we generated Bell state $|\Psi^+\rangle$ using Figure 3.3 and then in the same setup, we kept HWP_a and HWP_b in the output port of BS as shown in Figure 3.4. We transform state $|\Psi^+\rangle$ into states $|\Psi\rangle^-$ and $|\Phi\rangle^+$ by performing Z and X gate respectively in output port a using HWP_a . One extra HWP_b along with HWP_a is used to produce $|\Phi\rangle^-$ state by performing Y gate operation. In this case both the HWPs, a and b , are rotated at different orientations 0° and 45° respectively. In our case, both HWP is placed at output port a and b , but one can put both HWPs at same output port. Both the cases will give the same result.

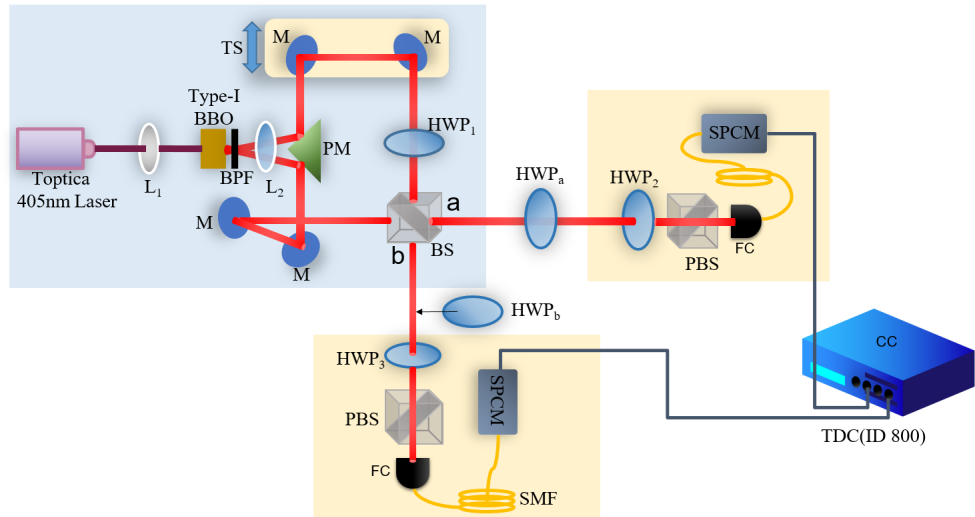


Figure 3.4: Experimental setup for the transformation of entangled state $|\Psi^+\rangle$ into $|\Psi\rangle^-$ and $|\Phi\rangle^+$ by performing Z and X gate operation respectively using HWP_a only. additional HWP_b along with HWP_a is used to transform the state $|\Psi^+\rangle$ into $|\Phi\rangle^-$.

3.4 Results and discussion

In this section, we present experimental results obtained for all the four polarization-entangled Bell states. In Figure 3.4, when HWP_a is aligned to 0° then it will act as Z gate and hence it will flip the sign of $|V\rangle_a$, while leaving $|H\rangle_a$ unchanged. In D/A basis, $|D\rangle_a$ will convert to $|A\rangle_a$ and vice-versa. This will transferred the state from $|\Psi\rangle^+$ to $|\Psi\rangle^-$. Initial entangled state in H/V and D/A basis is given by,

$$|\Psi\rangle^+ = \begin{cases} \frac{1}{\sqrt{2}}(|H\rangle_a|V\rangle_b + |V\rangle_a|H\rangle_b) & H/V \text{ basis} \\ \frac{1}{\sqrt{2}}(|D\rangle_a|D\rangle_b - |A\rangle_a|A\rangle_b) & D/A \text{ basis} \end{cases} \quad (3.10)$$

For $\theta_a = 0^\circ$, output state will be,

$$U_{\text{hwp}}(\theta_a)|\Psi\rangle^+ = |\Psi\rangle^-$$

$$|\Psi\rangle^- = \begin{cases} \frac{1}{\sqrt{2}}(|H\rangle_a|V\rangle_b - |V\rangle_a|H\rangle_b) & H/V \text{ basis} \\ \frac{1}{\sqrt{2}}(|A\rangle_a|D\rangle_b - |D\rangle_a|A\rangle_b) & D/A \text{ basis} \end{cases} \quad (3.11)$$

Now if we again rotate the HWP_a to 45° then it will act as a X gate and hence it will convert $|H\rangle_a$ to $|V\rangle_a$ and vice-versa. Also it will flip the sign of $|A\rangle_a$, while leaving $|D\rangle_a$ unchanged. Therefore, for $\theta_a = 45^\circ$, the state will become,

$$U_{\text{hwp}}(\theta_a)|\Psi\rangle^+ = |\Phi\rangle^+$$

$$|\Phi\rangle^+ = \begin{cases} \frac{1}{\sqrt{2}}(|H\rangle_a|H\rangle_b + |V\rangle_a|V\rangle_b) & H/V \text{ basis} \\ \frac{1}{\sqrt{2}}(|D\rangle_a|D\rangle_b + |A\rangle_a|A\rangle_b) & D/A \text{ basis} \end{cases} \quad (3.12)$$

Now to transform $|\Psi\rangle^+$ state to $|\Phi\rangle^-$ state, we used one more HWP_{*b*} in output port *b* of BS (Figure 3.4). We aligned HWP_{*a*} to 0° and HWP_{*b*} to 45° to get $|\Phi\rangle^-$ state. Therefore, for $\theta_a = 0^\circ$ and $\theta_b = 45^\circ$, the output state will be,

$$U_{\text{hwp}}(\theta_a)U_{\text{hwp}}(\theta_b)|\Psi\rangle^+ = |\Phi\rangle^-$$

$$|\Phi\rangle^- = \begin{cases} \frac{1}{\sqrt{2}}(|H\rangle_a|H\rangle_b - |V\rangle_a|V\rangle_b) & H/V \text{ basis} \\ \frac{1}{\sqrt{2}}(|A\rangle_a|D\rangle_b + |D\rangle_a|A\rangle_b) & D/A \text{ basis} \end{cases} \quad (3.13)$$

We have recorded the measurement in *H/V* and *D/A* basis. Polarization measurements are carried out using a combination of HWP and PBS in each arm. This combination will act as a projection operator. The measurement is performed by fixing the angle of

Coincidence detection	$ \Psi\rangle^+$	$ \Psi\rangle^-$	$ \Phi\rangle^+$	$ \Phi\rangle^-$
HH/VV	-	-	✓	✓
HV/VH	✓	✓	-	-
DD/AA	✓	-	✓	-
DA/AD	-	✓	-	✓

Table 3.2: Theoretical prediction of detecting entangled photon pair in *H/V* and *D/A* bases

Coincidence detection	$ \Psi\rangle^+$	$ \Psi\rangle^-$	$ \Phi\rangle^+$	$ \Phi\rangle^-$
HH/VV	13/14	18/15	698/751	731/784
HV/VH	660/771	763/724	21/14	18/15
DD/AA	798/675	17/14	680/738	17/15
DA/AD	13/16	653/768	14/15	825/735

Table 3.3: Experimental observation of detecting number of entangled photon pairs in *H/V* and *D/A* bases

HWP₂ (α) in one output port, while changing the angle of HWP₃ (β) in another port. The transmitted part of PBS is coupled into a single mode fiber. For example, if we want to measure the diagonal polarization (*D*) of photon then first we will rotate the diagonal polarization (*D*) to horizontal (*H*) with the help of HWP so that photons get

transmitted through the PBS and get coupled into single mode fiber. Table 3.2 shows the theoretical discrimination between all the four Bell state. To verify the theoretical prediction, we have recorded coincidence counts per second in H/V and D/A basis for each Bell state.

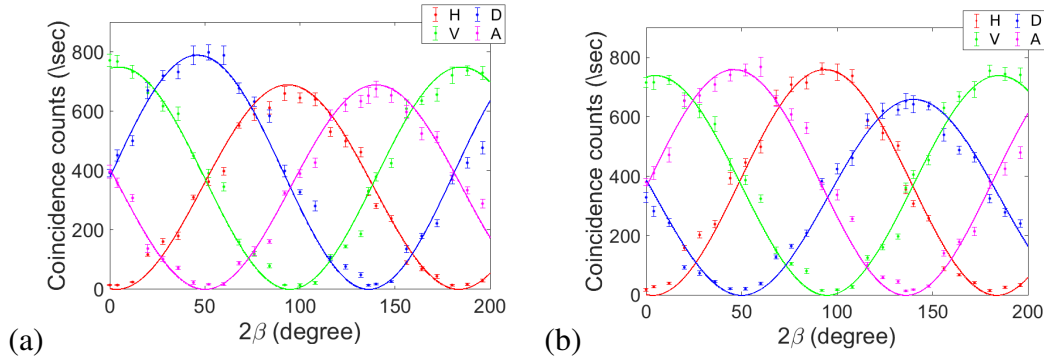


Figure 3.5: Experimental observation of polarization correlations for (a) $|\Psi\rangle^+$ and (b) $|\Psi\rangle^-$ state. Error bars indicate statistical uncertainty of one standard deviation. The coincidence counts (CC) are plotted along y-axis with the variation of 2β for $\alpha = 0^\circ$ (red), $\alpha = 22.5^\circ$ (blue), $\alpha = 45^\circ$ (green), and $\alpha = 67.5^\circ$ (magenta).

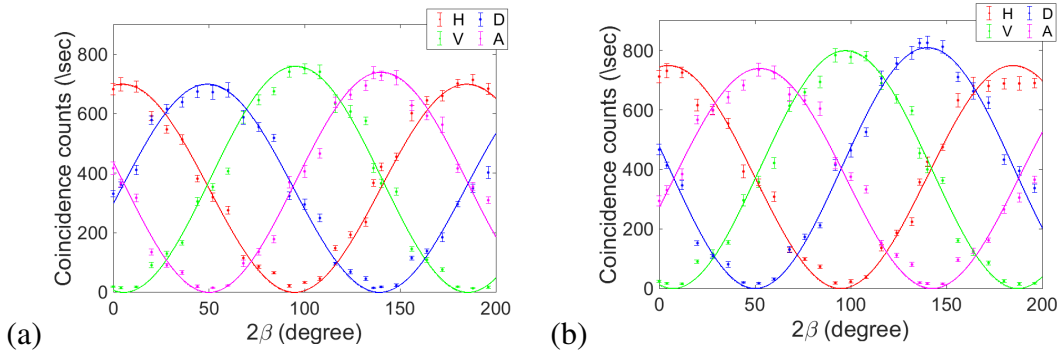


Figure 3.6: Experimental observation of polarization correlations for (a) $|\Phi\rangle^+$ and (b) $|\Phi\rangle^-$ state. Error bars indicate statistical uncertainty of one standard deviation. The coincidence counts (CC) are plotted along y-axis with the variation of 2β for $\alpha = 0^\circ$ (red), $\alpha = 22.5^\circ$ (blue), $\alpha = 45^\circ$ (green), and $\alpha = 67.5^\circ$ (magenta).

Coincidence detection is experimentally measured number of photon pairs for certain polarization state. Table 3.3 shows the experimental data. Our experimental result is matching with the theoretical prediction and by comparing Table 3.2 and 3.3, one

can predict which Bell state is measured. The experimentally observed polarization correlations are given as visibility curves in Figures 3.5 and 3.6. The total coincidence counts per second are plotted in y-axis as a function of HWP₃ angle 2β , while HWP₂ angle 2α is fixed.

Bell state	Avg. Vis.(%)	S Value	Fidelity (F)
$ \Psi\rangle^+$	96.18 ± 5.03	2.72 ± 0.07	0.9625
$ \Psi\rangle^-$	95.66 ± 4.28	2.71 ± 0.06	0.9626
$ \Phi\rangle^+$	95.61 ± 3.75	2.70 ± 0.05	0.9647
$ \Phi\rangle^-$	95.84 ± 3.17	2.71 ± 0.05	0.9608

Table 3.4: Calculated average visibility and Bell-CHSH parameter S .

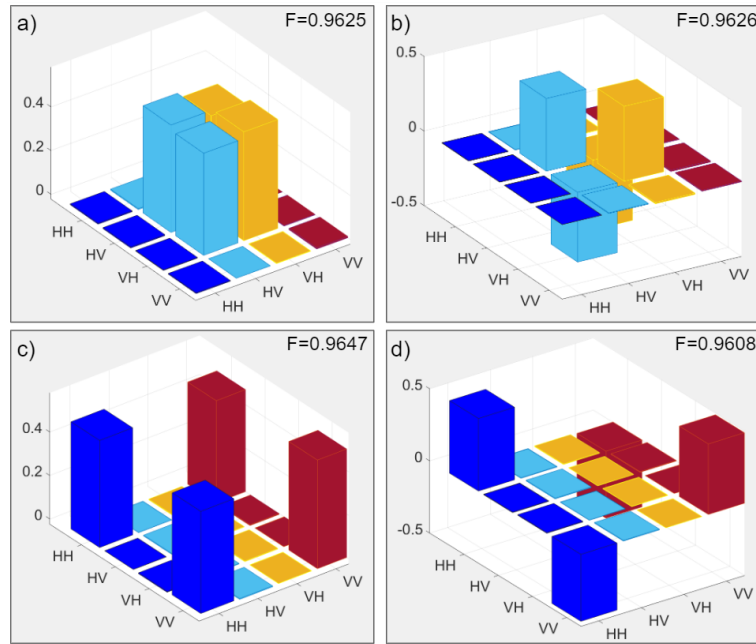


Figure 3.7: Calculated density matrix for entangled states (a) $|\Psi\rangle^+$, (b) $|\Psi\rangle^-$, (c) $|\Phi\rangle^+$, and (d) $|\Phi\rangle^-$. F is the state fidelity which is the measure of state overlap

To check the quality of entanglement, we calculated the Bell-CHSH parameter S . The S value greater than 2 ensures the existence of quantum entanglement between two photons. In our experiment, the average value of visibilities and the estimated Bell-CHSH parameter S for $|\Psi\rangle^+$, $|\Psi\rangle^-$, $|\Phi\rangle^+$, and $|\Phi\rangle^-$ are shown in Table 3.4. Because of the unitary transformation the S value for all the four Bell states is remains

unchanged. Quantum state tomography is performed to verify the theoretical prediction by calculating the state fidelity. The density matrix for all the four Bell states are shown in Figure 3.7. The state fidelity is around $\sim 96\%$ for each Bell state which shows the successful transformation of Bell states using HWPs.

3.5 Conclusion

In this chapter, we have shown that only HWP is enough to perform Pauli Z gate and X gate and it becomes the easiest way to transform entangled states. We first prepared the polarization-entangled Bell state $|\Psi\rangle^+$ using Type-I β -BBO crystal and 50:50 BS and then manipulated the initial state in order to achieve rest of the entangled states. We calculated the Bell-CHSH parameter S for each Bell state and since the transformation is unitary, we found out that S value, coincidence counts, and visibility for all the Bell states remain unchanged. Quantum state tomography is also performed to check the state fidelity with the desired state. The presented result may find applications in quantum communication and quantum information protocols, especially where the control over basis of maximally entangled state is required.

Chapter 4

Optimised entanglement detection for quantum information protocols

Not only does God play dice but... he sometimes confuses us by throwing them where they can't be seen.

—Stephen Hawking

4.1 Introduction

Quantum entanglement [23] has been one of the profound implications of quantum mechanics. It has intrigued generations of scientists involved in the study and development of quantum theory. Most notably, it led Einstein, along with colleagues Podolsky and Rosen, to question the completeness of quantum mechanics [8]. Although he knew quantum entanglement cannot be harnessed for faster-than-light communication, he still objected to the idea of non-locality, i.e. any action performed on one system cannot modify the description of another system that is space-like separated from the former. Later, Bell [9] proved that no local theory can give rise to such strong

correlations and the community at large accepted the nonlocal nature of quantum mechanics. The attention then shifted to what can be achieved by utilising quantum entanglement. This led to several proposals like superdense coding [131], quantum teleportation [60, 61, 61–63], entanglement based quantum cryptography [67–69], supersensitive measurements using interferometric methods [132–138], etc.

In all these applications, one of the primary steps is the characterization of the entanglement present in the system. To elaborate with a practical example, in entanglement based quantum cryptography, the two communicating parties can make sure of no information leakage to an adversary by verifying the entanglement between them. In the ideal case, if they determine that they share a maximally entangled state, they can be sure of the fact that there has been no eavesdropping. Similarly, in all such applications that use entangled states as resource, certification of entanglement is a vital step in the initial setup.

Given the importance of entanglement, its quantification has been an interesting topic. So much so, that there are too many measures of entanglement. The amount of entanglement present in quantum systems is generally quantified in terms of various measures of entanglement like von Neumann entropy [139], logarithmic negativity [140], entanglement of formation, concurrence [10] etc. All these measures are proven entanglement monotones. However, they require a complete quantum state tomography in order to determine the density matrix. After several steps of post-processing of the obtained density matrix, the values of the above quantities can be calculated which signifies the amount of entanglement. Although these measures are faithful and robust, these cannot be calculated in real time. For real time entanglement measurement, the Bell-CHSH inequality [141] continues to be the first choice [11, 11, 34, 128, 142–146]. In this case, a minimum of 16 measurements are required to check for entanglement in

any two qubit system [147]. A violation is obtained for all two qubit entangled states bounded by Tsirelson's bound [148]. Since any measurement on a quantum system collapses the state to an eigenstate of the measured observable, a minimum 16 copies of the initial two - qubit state are required to calculate the value of the Bell-CHSH parameter. This means that if there are multiple shared copies of the state available, 16 copies would be destroyed while checking for entanglement.

In this chapter, we propose a method for calculating the value of Bell-CHSH parameter with only two sets of measurement settings for two qubit entangled states. This leads to optimised use of resources and a much better cost to performance ratio when certifying the amount of entanglement present in the system. This could be particularly useful in quantum cryptographic applications under the general assumptions of the validity of quantum mechanics and its predictions. Our scheme is not suitable for general Bell tests used to determine the physical nature of reality and related questions. We use an already known reformulated version of the Bell-CHSH inequality and show that only two sets of measurement settings leading to a total of 8 measurements are sufficient for the purpose as opposed to the standard requirement of 16 measurements. We also show that it is possible to reliably perform an approximate quantum state estimation using only the proposed two sets of measurements. Although, a full quantum state tomography has to be performed to correctly determine the complete density matrix, for certain applications, these two measurement settings are sufficient to determine both the parity and the phase bits of a two qubit entangled state like in case of quantum teleportation, entanglement swapping and superdense coding.

4.2 Theoretical model

In this section, we will develop the theoretical model of our proposition. But before we get there, it is essential to review the mathematical background associated with the violation of Bell's inequality. In its modified form, the Bell-CHSH parameter, as it came to be known, has the form

$$S = E(\alpha, \beta) + E(\alpha', \beta') + E(\alpha', \beta) - E(\alpha, \beta'), \quad (4.1)$$

such that $|S| \leq 2$ is known as the Bell-CHSH inequality. $E(\alpha, \beta)$ is expressed as

$$E(\alpha, \beta) = P_{00}(\alpha, \beta) + P_{11}(\alpha, \beta) - P_{01}(\alpha, \beta) - P_{10}(\alpha, \beta), \quad (4.2)$$

where $P_{ij}(\alpha, \beta)$'s are probabilities of both the qubits being correlated ($i = j$) or anti-correlated ($i \neq j$) for detector settings α and β when measuring the spatially separated subsystems A and B . $E(\alpha, \beta)$ is then a measure of the correlation between the two qubits. Quantum mechanics predicts that for a maximally entangled state, $|E(\alpha, \beta)|$ is always equal to $1/\sqrt{2}$ if $|\alpha - \beta| = \pi/8$. This means, four measurement settings are required to obtain a violation of the Bell-CHSH parameter. In an experimental implementation, the measurement apparatus is generally composed of a polarizer and a detector. The polarizer can be replaced by a half-wave plate and a polarizing beam splitter.

We will now illustrate how the number of measurement settings can be halved by carefully choosing only two sets of angles. Let us rewrite the detector settings α, α' at

A and β, β' at B in terms of the Pauli operators as follows;

$$\alpha = \sigma_x, \alpha' = \sigma_z, \quad (4.3)$$

$$\beta = \frac{1}{\sqrt{2}}(\sigma_x \pm \sigma_z) \ \& \ \beta' = \frac{1}{\sqrt{2}}(\sigma_x \mp \sigma_z), \quad (4.4)$$

where σ_i 's are the Pauli operators. The Bell parameter S of Eqn. 4.1 then takes the form

$$S \rightarrow S'_{\pm} = \sqrt{2}(\sigma_x \otimes \sigma_x \pm \sigma_z \otimes \sigma_z). \quad (4.5)$$

The expectation value of S' has the range $-2\sqrt{2} \leq S' \leq 2\sqrt{2}$ which is same as before.

In case of the four Bell states

$$|\phi^{\pm}\rangle = \frac{1}{\sqrt{2}}(|00\rangle \pm |11\rangle), \quad (4.6)$$

$$|\psi^{\pm}\rangle = \frac{1}{\sqrt{2}}(|01\rangle \pm |10\rangle). \quad (4.7)$$

the expectation value of S' is obtained as follows

$$\langle \psi^+ | S'_- | \psi^+ \rangle = \langle \psi^- | S'_+ | \psi^- \rangle = -2\sqrt{2} \quad (4.8)$$

$$\langle \phi^+ | S'_+ | \phi^+ \rangle = \langle \phi^- | S'_- | \phi^- \rangle = 2\sqrt{2} \quad (4.9)$$

which means that $|\phi^+\rangle$ and $|\psi^-\rangle$ are the eigenstates of S'_+ while $|\phi^-\rangle$ and $|\psi^+\rangle$ are the eigenstates of S'_- . This implies that in order to violate Bell-CHSH inequality, we only need two sets of measurements. The first set is characterised by σ_x measurement on both the qubits while the second set is characterised by the σ_z measurement, also on both the qubits. Practically, this means that the qubits need to be measured in X basis and Z basis only and the measurement results to be recorded in coincidence. This is *half* the number of measurement settings used in general.

We can extend this calculation for a general case too. Consider a two - qubit pure state of the form

$$|\psi\rangle = a_{00}|00\rangle + a_{01}|01\rangle + a_{10}|10\rangle + a_{11}|11\rangle \quad (4.10)$$

where $a_{i,j}$ are complex coefficients. The above equation can be used to represent all two qubit pure states including entangled states. Calculating $\langle S'_{\pm} \rangle$, we obtain

$$\begin{aligned} \langle S'_{\pm} \rangle &= \sqrt{2}\{(a_{00}^* \pm a_{11}^*)(a_{00} \pm a_{11}) \\ &+ (a_{01}^* \mp a_{10}^*)(a_{10} \mp a_{01})\} \end{aligned} \quad (4.11)$$

This shows that the Bell-CHSH operator of Eqn. 4.11 is applicable for any two qubit pure state. In case of maximally entangled Bell states, either $a_{00} = a_{11} = 1/\sqrt{2}$ and $a_{01} = a_{10} = 0$ or $a_{00} = a_{11} = 0$ and $a_{01} = a_{10} = 1/\sqrt{2}$. Only in these cases, a maximum value is obtained. For the uniform superposition case, when all the coefficients are equal, $\langle S'_{\pm} \rangle = 0$ since in that case the two qubit state is a product state. This formulation will work for any isotropic mixed state too. This one-parameter family of states of play an important role when it comes to quantum communication protocols and are also sometimes referred to as noisy singlets. This family of states best represents any pure polarization entangled state due to the effects of depolarizing channel through which it passes. Consider the state

$$\rho = p|\psi\rangle\langle\psi| + (1-p)\frac{\mathcal{I}}{4} \quad (4.12)$$

where $|\psi\rangle$ can be one of the four Bell states, and $\frac{\mathcal{I}}{4}$ is the maximally mixed state of two qubits. The parameter p is probability. In this case, the expectation value of S'_{\pm} is

given as

$$\text{Tr}(\rho S'_{\pm}) = \pm\sqrt{2}(1+p) \quad (4.13)$$

which shows that a maximum violation is obtained only if $p = 1$, i.e. in case of a pure Bell state.

4.3 Experimental setup and results

In this section, we present the experimental results obtained using entangled photons prepared in the polarization basis. The entangled states are produced at the output of

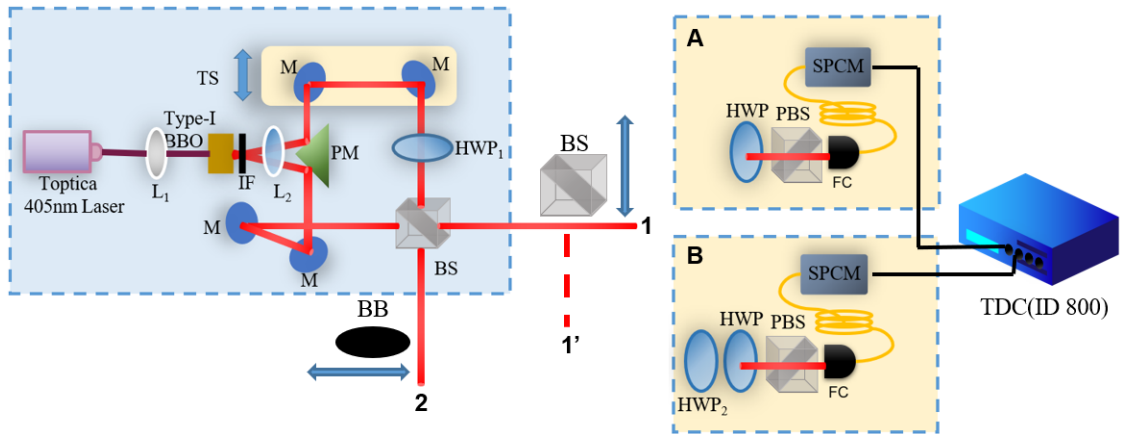


Figure 4.1: Experimental setup used for generating the four Bell states. It is based on the Hong-Ou-Mandel (HOM) interferometer (enclosed in blue dotted box). Photon counting at ports 1 and 2 produces the HOM dip. Boxes A and B are used for polarization entanglement analysis. The blue arrows indicate translation stages. The details are in the text. L_1, L_2 : Lens; BBO : β Barium Borate crystal; TS : Translation Stage; M : Mirror; HWP : Halfwave Plate; BS : Beam Splitter; BB : Beam Blocker; PBS : Polarizing Beam Splitter; FC : Fiber Coupler; SMF : Single Mode Fiber; $SPCM$: Single Photon Counting Module and TDC : Time to Digital Converter.

a Hong-Ou-Mandel interferometer as shown in Figure 4.1. A pump laser is passed through a Type-I β -Barium Borate crystal to produce down-converted photon pairs having the same polarization state. The two photons are then sent in different paths using a prism mirror. A half-wave plate in one of the arms, HWP_1 , is used to rotate

the polarization of one of the photons. The photons are then made incident on different ports of a balanced non-polarizing beam splitter for the Hong-Ou-Mandel interference effect. The quality of the interference can be calculated from the visibility data and can be seen in Figure 4.2.

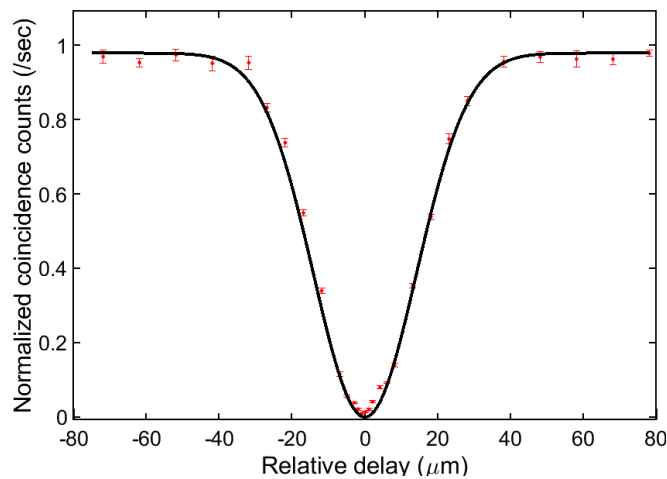


Figure 4.2: Visibility plot of the HOM interference. We recorded a visibility of 98% measured as the ratio between the difference and sum of maximum and minimum coincidences.

This setup directly produces $|\psi^-\rangle$ at the output of interferometer i.e. ports 1 and 2 when one of the photons is orthogonally polarized to that of the other. Box A is used at both the outputs to analyse this state. Using Box A at port 1 and Box B at port 2 results in the generation and analysis of $|\phi^-\rangle$. When both the photons emerge at the same output port of the interferometer, they can be directed to different spatial modes 1 and 1' using another beam splitter. Box A at both 1 and 1', then leads to the generation and analysis of $|\psi^+\rangle$ while Box A at port 1 and Box B at 1' is used for generating and analysing $|\phi^+\rangle$. The detection setup, in a typical case, consists of a HWP, a PBS and single photon detector like single photon counting modules (SPCM) at each output of the PBS. This is the standard setup, as mentioned in the previous section, and is used most commonly in quantum key distribution systems.

Measurement	N_{HH}	N_{VV}	N_{VH}	N_{HV}	S'_+	S'_-	State
$\sigma_x \otimes \sigma_x$	5	5	136	134	-2.70	-0.07	$ \psi^-\rangle$
$\sigma_z \otimes \sigma_z$	1	2	126	170			
$\sigma_x \otimes \sigma_x$	15	11	116	111	-0.23	-2.49	$ \psi^+\rangle$
$\sigma_z \otimes \sigma_z$	126	147	3	3			
$\sigma_x \otimes \sigma_x$	477	526	24	18	0.71	2.67	$ \phi^-\rangle$
$\sigma_z \otimes \sigma_z$	9	9	557	505			
$\sigma_x \otimes \sigma_x$	172	177	26	10	2.47	0.18	$ \phi^+\rangle$
$\sigma_z \otimes \sigma_z$	192	169	8	3			

Table 4.1: Coincidence counts with optical qubits. The numbers are actual counts recorded with a coincidence window of 486 ps and integration time of 1 s.

In the polarization basis, a σ_z measurement means measuring in the $\{|H\rangle, |V\rangle\}$ basis. For this the HWP is aligned at 0° . In this case, HWP does nothing on the polarization state of the photons. The PBS serves as the projection operator. In the case of σ_x measurement, HWP is rotated to 22.5° . In this case, the action of the HWP combined with the PBS is equivalent to a measurement in the $\{|D\rangle, |A\rangle\}$ basis. In our case, the detection setup had a single SPCM. This resulted in the trade-off that we required a total of 8 measurement settings. But this was a setup induced limitation. In case of the standard setup, just two measurement settings are sufficient.

In the Table 4.1, we outline the results of measurements. N_{ij} stands for the total number of coincidence counts or simultaneous detections at the detectors placed in i -th and j -th output ports of the PBS. In our limited setup, N_{ii} was obtained by recording the coincidence counts between the two detectors with the HWPs aligned along the same direction. N_{ij} was obtained by orienting one HWP along the i direction and the other oriented orthogonally along the j direction. We can calculate the value of the Bell-CHSH parameter as defined in Eqn. 4.11 from the normalized coincidence numbers.

These are calculated by dividing the number of coincidences N_{ij} by the sum of all the

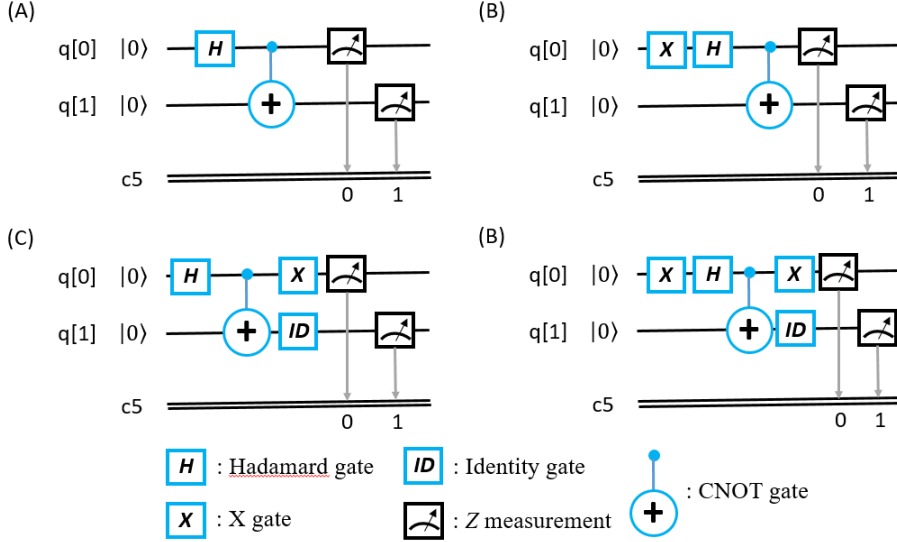


Figure 4.3: Experimental setup used for generating the four Bell states. (A) $|\phi^+\rangle$, (B) $|\phi^-\rangle$, (C) $|\psi^+\rangle$ and (D) $|\psi^-\rangle$. q[0] and q[1] are the qubits. All are initialized to $|0\rangle$ by default.

coincidence events $\sum_{i,j} N_{i,j}$. The expectation value for each measurement setting is then calculated as

$$\langle \sigma_i \otimes \sigma_i \rangle = \frac{(N_{HH} + N_{VV}) - (N_{HV} + N_{VH})}{N_{HH} + N_{VV} + N_{HV} + N_{VH}} \quad (4.14)$$

where $i \in \{x, z\}$. We use Eqn. 4.14 to calculate the value of S'_{\pm} . Using the numbers from the first row, we obtain $S'_+ = -2.70$ and $S'_- = -0.07$. As outlined earlier, $|\psi^-\rangle$ is an eigenstate of S'_+ and this is what we have obtained. Similarly, from the second row, $S'_+ = -0.23$ and $S'_- = -2.49$ for $|\psi^+\rangle$. In case of $|\phi^-\rangle$, we obtain $S'_+ = 0.71$ and $S'_- = 2.67$ from the third row. From the last row, we see that $S'_+ = 2.47$ and $S'_- = 0.18$ for $|\phi^+\rangle$.

Another interesting aspect of the above is that we can use the coincidence data to guess the state if that information is unavailable. Consider a situation, where the only information available to us is that we are dealing with one of the four Bell states. We do not know which one. It is clear from the Table 4.1 that by looking at which combination

of detectors produces maximum coincidences for each measurement setting coupled with which of S'_+ or S'_- produce a violation, we can safely conclude what is the state in question. For illustration, compare the first and second rows of Table 4.1. In both cases, measurement in Z basis produces maximum coincidences between the H and V ports. This tells us we are dealing with the anti-symmetric state. From the first row, we obtain a violation for S'^+ , and from the second row, we obtain a violation for S'^- . This tells us that the data recorded in the former is for the singlet state $|\psi^-\rangle$, and that in latter is for $|\psi^+\rangle$. We can use a similar argument for guessing that state from the data in the next two rows.

Measurement	N_{HH}	N_{VV}	N_{VH}	N_{HV}	S'_+	S'_-	State
$\sigma_x \otimes \sigma_x$	5	5	43	47	-2.29	-0.03	$ \psi^-\rangle$
$\sigma_z \otimes \sigma_z$	5	5	38	52			
$\sigma_x \otimes \sigma_x$	5	3	49	43	-0.17	-2.21	$ \psi^+\rangle$
$\sigma_z \otimes \sigma_z$	52	39	6	3			
$\sigma_x \otimes \sigma_x$	46	46	5	3	0	2.38	$ \phi^-\rangle$
$\sigma_z \otimes \sigma_z$	5	3	51	41			
$\sigma_x \otimes \sigma_x$	48	47	3	2	2.46	0.08	$ \phi^+\rangle$
$\sigma_z \otimes \sigma_z$	42	50	5	3			

Table 4.2: Coincidence counts on IBM Quantum platform. The numbers below are in percentage.

We have also used IBM Quantum to further verify these results. It provides an excellent platform for testing and implementing various strategies. We implemented the circuits of Figure 4.3 to generate the four Bell states and record the measurement outcomes of the two settings. $|\psi^+\rangle$ was generated operating on $q[0]$ with the Hadamard gate. Since all the qubits are initialised to $|0\rangle$ by default, the Hadamard gate (represented by H in Figure 4.3), takes $q[0]$ to $|+\rangle = \frac{1}{\sqrt{2}}(|0\rangle + |1\rangle)$. A C-NOT gate on $q[1]$ with $q[0]$ as the control then produces the required state.

The X gate simply flips the state of the qubit on which it acts from $|0\rangle$ to $|1\rangle$ and vice versa. Also, by default, any measurement on the platform happens in the Z basis. So, the default measurement on both $q[0]$ and $q[1]$ results in the $\sigma_z \otimes \sigma_z$ measurement. The $\sigma_x \otimes \sigma_x$ is equivalent to rotating the state to the X basis and then performing a Z measurement. So the X gate was again applied after the C-NOT gate to rotate the state. This was needed since no other measurement setting is available on IBM Quantum other than the default setting. The results are outlined in Table 4.2. Please

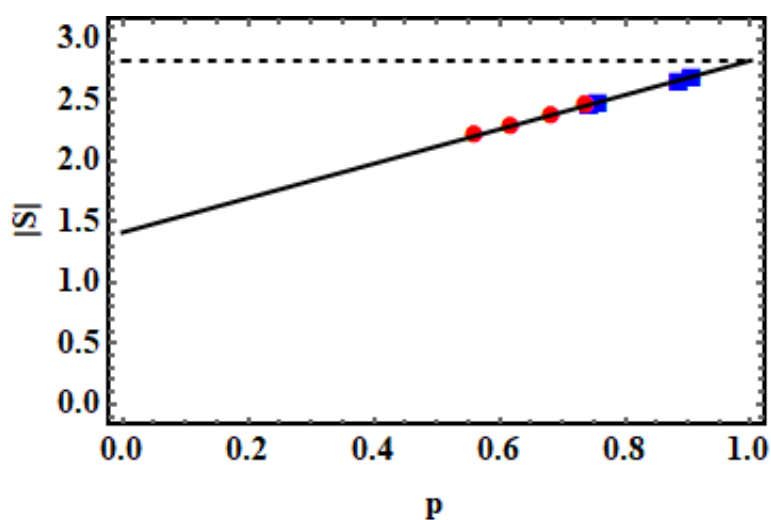


Figure 4.4: A plot of $|S|$ as a function of the parameter p as in Eqn. 4.13 (black line). The black dashed line marks the value $|S| = 2\sqrt{2}$. The blue squares mark the values of $|S|$ obtained from the laboratory, and the red circles mark the same obtained from IBM Quantum experience.

note that the outcomes are recorded as percentages in this case. For each set of data, the experiment was run for 4096 times. Due to the inherent noise in the gate operations, the results obtained in our laboratory consistently outperformed those obtained from IBM Quantum. But even in the presence of noise, we could obtain the Bell violation with only two measurement settings. Although implied, this further establishes the platform independence of our measurement scheme. Also, like before, just by looking at the pair of detectors that produce maximum coincidences and which of the Bell-

CHSH parameters S'_+ or S'_- violate the inequality, we can predict the prepared state.

In Figure 4.4, we show the variation of $|S|$ with p for the one-parameter family of states of Eqn. 4.13. In the same figure, we have marked the values of $|S|$ that we obtained from the optical setup and the IBM Quantum Experience. This helps us to directly read out the amount of noise in the generated state as quantified by the parameter p .

4.4 Discussion

The scheme that we present here is directed at quantum cryptographic protocols like entanglement-based quantum key distribution protocols. In these protocols, a violation of the Bell-CHSH inequality is used to determine the security of communication. These protocols are carried out under the assumptions that general postulates of quantum mechanics, namely, the no-cloning theorem and monogamy of entanglement are valid. A violation of Bell-CHSH inequality in such a scenario is used to establish that the communicating parties share maximum quantum correlation, and there has been no tampering by an eavesdropper. A subset of the measurement results is used in estimating the value of the Bell-CHSH parameter and check for entanglement between the two qubits. In our scheme, we have shown that a smaller subset can be used to reliably estimate the amount of entanglement. This leads to optimised use of the qubits for the generation of secure key bits.

4.5 Conclusion

In this chapter, we have presented a more efficient method of obtaining a violation of the Bell-CHSH parameter for a two qubit entangled state. We show that the total number of measurement settings required to obtain a violation can be halved. Ad-

ditionally, from the form of the Bell-CHSH parameter that is being violated, we can easily guess the entangled state, without the need to perform a full state tomography. This method can have implications for laboratory demonstrations and real world applications. Since, a lesser number of measurements are required to calculate the entanglement as well as to guess the input state, this could be a more efficient method of verifying entanglement in device independent quantum key distribution systems where the resource, i.e the entangled qubits are extremely valuable. A lesser number of measurements would imply a large resource at disposal for generating the key bits thereby having a direct effect on key rates. We have verified our scheme through experiments performed on optical qubits in the laboratory as well on the IBM Quantum platform.

Chapter 5

BBM92 quantum key distribution for an atmospheric channel of 200 meters

Quantum phenomena do not occur in a Hilbert space. They occur in laboratory.

-Asher Peres

5.1 Introduction

In classical communication, the security of encryption keys for parties communicating with each other is an ongoing challenge. Even after 50 years of digital communication, the security depends upon the hardness of breaking the encryption, which may compromise the security of encrypted messages sent through a public channel once a quantum computer intercepts them. With the development of quantum computers having sufficient numbers of good quality qubits becoming a practical reality, the demand for secure communication has increased. It has already been realized that by using Shor's algorithm [149–151], one can break the encryption used in key distribution be-

tween communicating parties [126]. Quantum Key Distribution (QKD), on the other hand, relies on the principles of quantum mechanics, like uncertainty principle, no-cloning theorem and monogamy of entanglement to securely distribute keys between the communicating parties [70, 152]. These principles make QKD safe even against a quantum computer while making no assumptions on Eve's technological capability.

Every QKD protocol has distance limitations as the loss and disturbance in the channel increases with the transmission distance. Entanglement-based QKD (EB-QKD) are ideal for long-distance quantum communication like satellite-to-ground, as it can make two far apart ground stations communicate securely. Also, the security is not compromised irrespective of the satellite distributing entangled photon pairs is trusted or not. It must be noted that the satellite-to-ground EB-QKD has already been performed [153, 154]. The current limitation of using EB-QKD is the low key rate, as the entangled photon pairs are generally produced via spontaneous parametric down-conversion (SPDC) [155, 156] process which is not very efficient. The two factors contributing to low key rates are low-efficiency of the photon-pair generation, and loss of photons in the communication channel. Low efficiency can be compensated with the high-brightness, high-fidelity photon-pair sources. On the other hand, one of the ways to mitigate the effect of channel is by studying its effect on parameters controlling the QKD. The controlled and quantitative studies to observe the influence of atmospheric conditions such as the presence of particulate matter (PM) or aerosols have not been considered earlier. In this study, we account the presence of aerosols and show its effect on the secure key rate.

Atmospheric aerosols, solid or liquid particles suspended in air, are produced by natural sources and anthropogenic emissions. Mineral dust and sea salt are produced from natural sources while sulfate, nitrate, black carbon and organic carbon are emit-

ted primarily from emissions of fossil fuel and biomass burning/biofuels and/or converted into particles through a gas-to-particle conversion mechanism. Atmospheric aerosols can scatter and absorb the incident radiation. The dry and long summer of Ahmedabad, a metropolitan city and urban environment, contains a relatively higher amount of aerosols [157]. Here, we report the implementation of BBM92 protocol at the indigenously developed communication channel facility at PRL, and the effect of dust/atmospheric channel on the secure key rate. This is the first attempt, in India, to implement such studies, and eventually will form a strong base for the future long-distance quantum communication. For carrying out satellite-to-ground based communication, entanglement-based QKD (EBQKD), such as BBM92 protocol is the most suitable as it does not require a trusted node [158, 159]. The chapter is structured as follows: Section 5.2 contains preliminaries about the BBM92 protocol, the entangled photon-pair source, and the indigenous facility built to study the atmospheric channel. Section 5.3 contains the results obtained and the related discussion. And finally, we end the chapter with concluding remarks in section 5.4.

5.2 Background

BBM92 is a QKD protocol which involves pairs of entangled photons and can be regarded as an entangled photon version of the BB84 protocol. BB84 is a prepare and measure QKD protocol where Alice randomly generates polarization states using random number generators (RNGs) whereas in BBM92 the randomness is inherent to the entangled photon pairs. The basic block diagram of the BBM92 protocol is shown in Figure 5.1.

In this protocol, a common sender Charlie generates a pair of entangled photons and sends them to Alice and Bob through a quantum channel. Quantum channels can

be free-space, water or optical fibre. Alice and Bob independently perform their measurements in a random basis. Once the measurement is done, both declare their basis choices through the public channel. Only those measurements contribute to key for

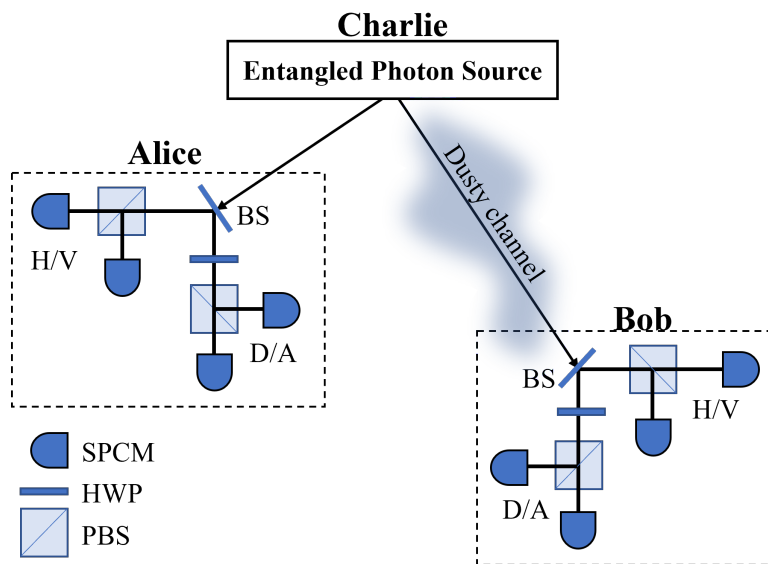


Figure 5.1: The block diagram of implemented BBM92 protocol.

which Alice and Bob have chosen the same basis, and the rest of the measurements are discarded. The key formed after this process is called sifted key. To compensate for any secrecy loss during the basis reconciliation through classical channel, error correction (EC) and privacy amplification (PA) is performed on sifted key to get a secure key. In our experiment, the quantum channel between Charlie and Alice is not exposed to atmospheric aerosols as both are co-located in the same room. However, the quantum channel between Charlie and Bob experiences the free-space dusty atmospheric channel of 35 m and 200 m.

5.2.1 Entangled photon-pair source

The high-efficient, high-brightness, in-house developed polarization-entangled photon-pair source was set up using PPKTP crystal placed in a Sagnac interferometer. The

schematic of the experimental setup is shown in Figure 5.2 [160]. A continuous-wave laser at the wavelength of 405 nm and output power of ~ 5 mW is used to pump a 30 mm long Type-0 PPKTP crystal of period $\Lambda = 3.425 \mu\text{m}$. A lens L_1 of focal length 400 mm is used to focus the pump beam on the crystal to generate entangled photons using a novel experimental scheme based on polarization Sagnac interferometer consisting of a dual-wavelength polarizing beam splitter cube (D-PBS), two half-wave plates HWP₃, HWP₄, and two high reflecting ($R > 99\%$) mirrors M_1 , M_2 at 810 nm. The working principle of this setup is well explained in the article [160].

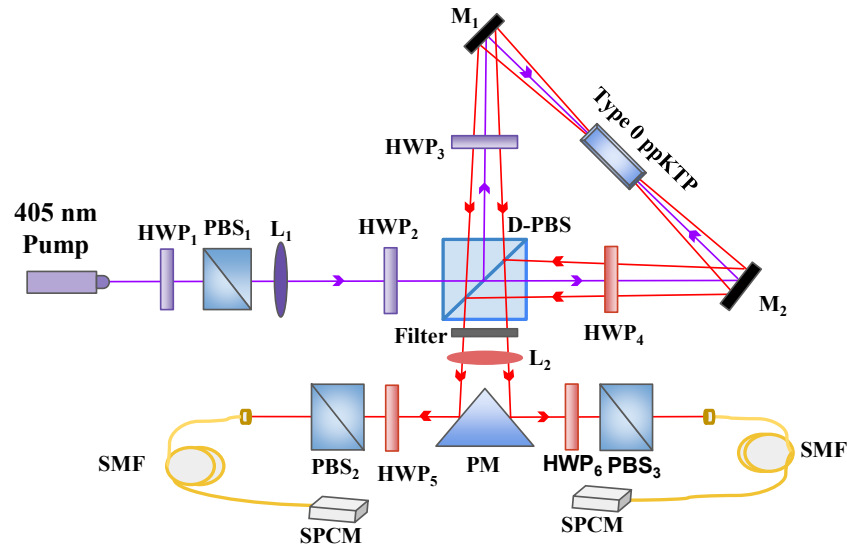


Figure 5.2: Schematic diagram of the polarization entangled photon pairs source. Dual polarizing beam splitter D-PBS operates at both 405 nm and 810 nm. Half wave plates HWP_{1,2,3} and HWP_{4,5,6} operate at 405 nm and 810 nm respectively. Lens L_1 : 400 mm, lens L_2 : 200mm, M_1 and M_2 : high reflecting mirrors at 810 nm, Filter: bandpass filter of bandwidth 10 nm centered at 810 nm, PM: prism mirror, SMF: single-mode fiber, SPCM: single-photon counting modules.

Since both the clockwise and counter-clockwise pump beams follow the same path but in opposite directions inside Sagnac interferometer and the PPKTP crystal is placed symmetric to the D-PBS, the implemented scheme is robust against any optical path changes to produce SPDC photons in orthogonal polarizations with ultra-stable phase.

The analyzer comprises a PBS and a HWP plate, and is used to measure the polarization entanglement of the generated photon pairs. The polarization entangled state generated from this method is

$$|\Psi\rangle = \frac{1}{\sqrt{2}} (|HH\rangle + |VV\rangle). \quad (5.1)$$

5.2.2 Communication channel and their positioning

Our communication channel consists of arrangements on two buildings, located nearby, in the Thaltej campus of PRL. The sending and receiving ends are located on the same

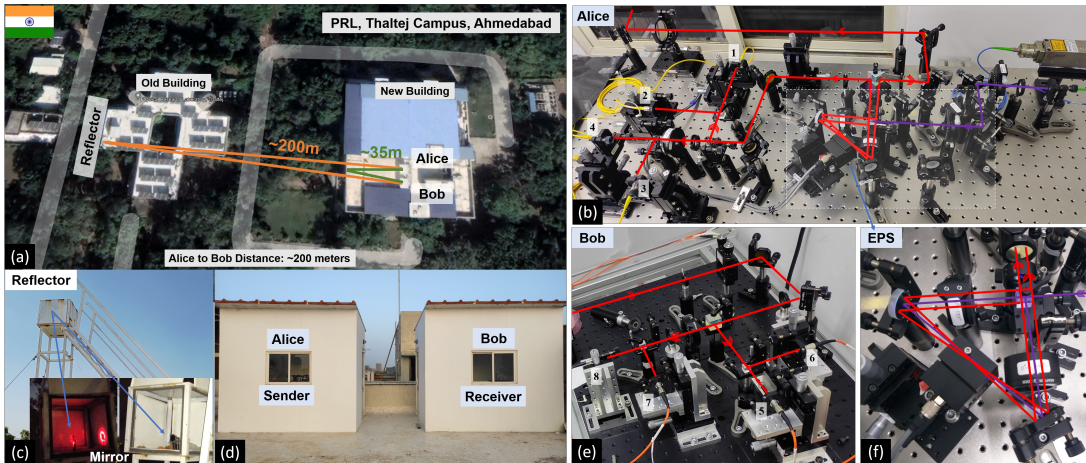


Figure 5.3: Arrangement of various components in the channel. It includes the location of Alice and Bob, and their setups. (a) Aerial view of free space entanglement based QKD channel (Image courtesy: Google earth), (b) optical setup of Alice. Red solid lines indicate the direction of entangled photon pair. Out of each pair generated, one stays with Alice and another goes to Bob (c) non-LOS channel consist of one reflecting mirror, (d) front view of Alice and Bob room, (e) optical setup of Bob, (f) preparation of entangled photon pair source (EPS).

terrace in two separate rooms. There are two reflectors - one for a path length of 35 m and another for 200 m on the other building to reflect back the photons. The reflector consists of a 1-inch diameter mirror placed on a structure dedicated to this purpose.

The channels run through a free-space open atmosphere to study the effect of aerosols/dust on the protocols. The schematic of the building structure and the placement of the equipment is shown in Figure 5.3. Charlie who prepares entangled photon-pairs and Alice are co-located in our arrangement, while Bob is placed in the nearby room. Out of each photon pair generated, one stays at the receiving end with Alice and the another travels through the quantum channel consisting of going to the reflector and getting reflected to reach the receiving end to Bob, as shown in the protocol diagram (Figure 5.1). The complete optical setup is shown in Figure 5.4. The experiment was performed at night (11 PM to 5 AM Indian Standard Time), in order to ensure that there is no interference due to the direct sunlight.

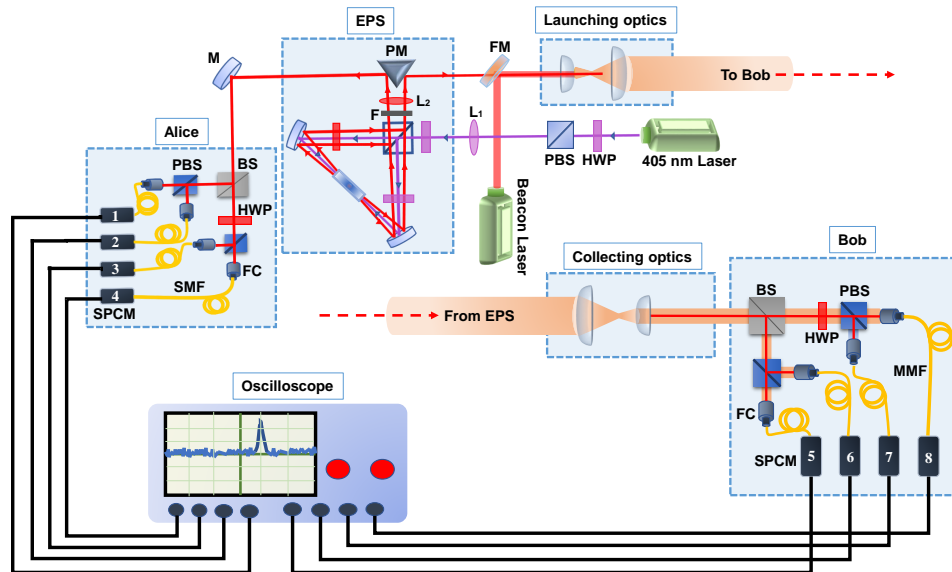


Figure 5.4: Schematic of the complete experimental setup that includes both optical and electronic arrangements. EPS: entangled photon source, FM: flip mirror, PM: prism mirror, M: mirror, F: filter, FC: fiber coupler, BS: beam splitter, PBS: polarization beam splitter, HWP: half wave plate, SMF: single-mode fiber, MMF: multi-mode fiber, SPCM: single-photon counting modules.

5.3 Results and Discussion

To study the effect of aerosols/dust present in the atmospheric channel on the secure key rate, we performed the experiment for 35 m channel on 8 May 2021 and 200 m channel on 10 May 2021. The atmospheric conditions for these two days are summarized in Table 5.1. The extinction coefficient (Ext.) in the table represents the loss of photons due to absorption and scattering, which depends on the concentration of atmospheric aerosols, their size distribution, and refractive index. Aerosol characteristics reported here are measured in Aerosol Monitoring Laboratory, PRL. The extinction coefficient is measured using CAPS PM monitor (Aerodyne Research Inc., USA) and aerosol size distribution and PM less than 2.5 micrometer diameter are measured using an aerosol spectrometer (GRIMM Aerosol Technik, Germany). From the Table 5.1, the extinction coefficient on 10 May 2021 is lower by $\sim 37\%$, leading to clear atmosphere and more transmissivity through channel. Also, the value of particulate matter (PM_{2.5}) has lower concentration. Thus, choosing these two different days have provided the variability in the atmospheric conditions, most suitable for this study. In Ahmedabad, the higher values occur due to lower wind speed and shallow atmospheric boundary layer [157].

Date	Ext. ($[\text{Mm}]^{-1}$)	PM _{2.5} ($\mu\text{g}/\text{m}^3$)
8 May 2021	$\gamma_{35} = 76.41 \pm 7.78$	2.87 ± 0.26
10 May 2021	$\gamma_{200} = 48.67 \pm 6.70$	1.68 ± 0.24

Table 5.1: Extinction coefficient (Ext.) and particulate matter (PM_{2.5}) concentrations are averages of hourly data from 12 midnight to 5 AM obtained from the Aerosol Monitoring Laboratory, PRL. The extinction coefficients data correspond to 525 nm. The data is fitted with the Angstrom power law for urban aerosols (model) corresponding to 70% relative humidity (appropriate for April-May) and found that wavelength exponent for extinction coefficients between 525 and 800 nm is about 1.5. Mm: Mega meter.

The channel transmissivity was measured by sending a beacon laser beam of 810

nm through the channel and was measured to be 94% for 35 m and 70% for 200 m. The power of laser was measured before the launching optics and after the collecting optics to estimate the channel transmissivity on both days. The use of a beacon laser was crucial for precise alignment and also for further corrections required due to the breeze in the weather on both days. From Figure 5.4, one can observe that eight detectors are used in the experiment, four each for Alice and Bob. Analogous to any classical communication protocol, BBM92 also requires timing synchronization between communicating parties to distribute keys correctly. We connected the SPCM4 and SPCM8 to time-tagger ID900, and found the time-difference between Alice and Bob is 120 ns for ~ 35 m and 666 ns for ~ 200 m channels based on the histogram obtained between the two channels (Figure 5.5). The coincidences were measured with the time-window of 1 ns.

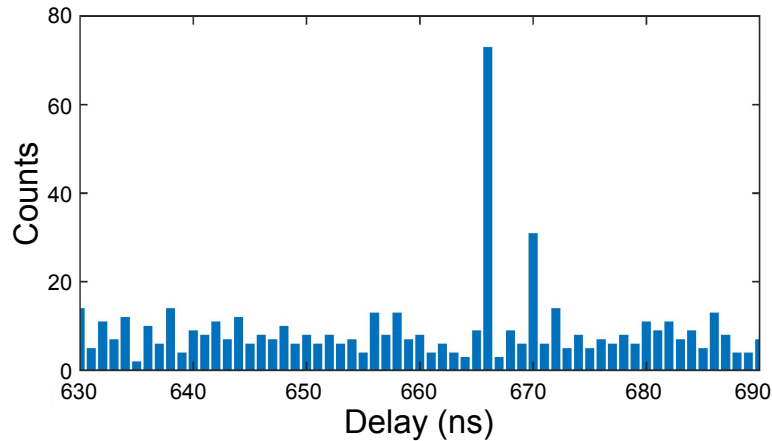


Figure 5.5: Time delay between Alice and Bob for 200 meters as observed from coincidence histogram.

We started with the effect of channel on the entanglement distribution between Alice and Bob, and measured the H/V and D/A polarization visibilities. The brightness of the entangled photon source is $0.3 \text{ KHzmW}^{-1}\text{nm}^{-1}$ and the fidelity is 92.76%. The graphs corresponding to these measurements are shown in Figures 5.6 - 5.7. The

visibilities obtained for 35 m channel on 8 May 2021 were 93.17%, 93.71%, 85.39% and 83.12% for H/V and D/A , respectively. The mean of these visibilities is 88.85%. For 200 m channel on 10 May 2021, the respective visibilities were 92.16%, 93.72%, 88.76% and 89.34%. The mean of these visibilities is 90.99%. The parameters obtained for both the distances are summarized in Table 5.2. The S value greater than 2 ensures that secure key distribution can be done over the given channel. It shows that the atmosphere plays a role as visibilities are higher for 200 m, because of the lower extinction coefficients on May 10, despite the channel length being longer. The total count rate is a combined effect of channel losses and the length of the channel.

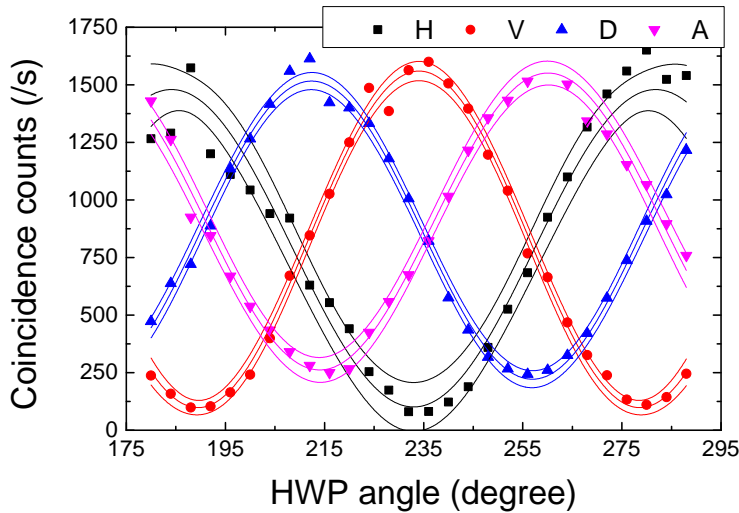


Figure 5.6: Obtained H/V and D/A graphs for 35 m channel taken on 8 May 2021. Solid lines are theoretical fit and lines of 98% confidence interval.

The quantum bit-error-rate (Q) and sifted key rate (SKR) can be calculated as [161, 162]

$$Q = \frac{1 - \text{Visibility}}{2}. \tag{5.2}$$

The value of Q for 35 m is 5.58% and for 200 m it is 4.50%. The sifted key rate can

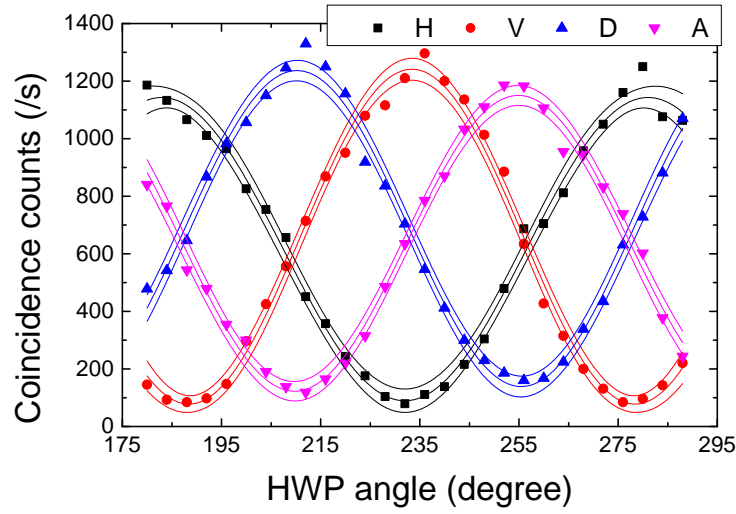


Figure 5.7: Obtained H/V and D/A graphs for 200 m channel taken on 10 May 2021. Solid lines are theoretical fit and lines of 98% confidence interval.

be calculated from the coincidence counts rates (cc) as

$$R_{sif} = 4 \times cc. \quad (5.3)$$

The factor 4 accounts for the total of all four coincidences (HH , VV , DD , and AA), as the correct number of coincidences will contribute to total sifted key rate. The secret key rate after the error correction is given by

$$R_{sec} = n \left(\frac{1}{2} - 2 \times Q - s \right), \quad (5.4)$$

where n is the number of bits left after error correction, and s is the security parameter [163]. The lower value of R_{sec} is a direct consequence of worse atmospheric conditions, which is also consistent with the visibilities. The different key rates obtained for both the distances are summarized in Table 5.2. The measured channel transmission is 0.94 for 35 m and 0.70 for 200 m on the two dates of the experiment. As the atmospheric condition follows Beer-Lambert law [164], the transmission T of the channel

Parameters	35 m	200 m
Channel transmission (%)	94	70
CHSH Bell parameter (S)	2.51±0.06	2.54±0.06
Mean visibility (%)	88.85±5.39	90.99±5.89
QBER (%)	5.58	4.50
Sifted key rate (kbps)	6.37	4.89
Key rate after EC (kbps)	6.01	4.20
Key rate after PA (kbps)	2.33	1.71
Secure key rate (kbps)	2.33	1.71

Table 5.2: Summary of the parameters obtained for 35 m channel on 8 May 2021, and 200 m channel on 10 May 2021.

can be written in terms of the number of photons sent (N_{In}) and the number of photons received (N_{Out}) on the other end of the free space atmospheric channel as

$$T = \frac{N_{Out}}{N_{In}} = Sc \exp(-1.5 \times \gamma L), \quad (5.5)$$

where Sc is the scaling parameter, γ is the extinction coefficient of the atmosphere, and L is the propagation length. The scaling parameter contains all the losses, except the effect from atmosphere. With the transmission information, we obtained the values $Sc_{35} = 0.944$ and $Sc_{200} = 0.710$.

Comparing the atmospheric conditions including the channel lengths for 8 May and 10 May, the transmission (T) ratios f can be written as

$$f = \frac{Sc_{35} \exp(-1.5 \times \gamma_{35} 35)}{Sc_{200} \exp(-1.5 \times \gamma_{200} 200)} = 1.34. \quad (5.6)$$

From our channel and experiments, the similar ratios are observed for the coincidence rates (cc), sifted key rate (R_{sif}) and secured key rates (R_{sec}), as shown by

$$\frac{cc_{35}}{cc_{200}} = 1.28, \quad (5.7)$$

$$\frac{R_{sif\ 35}}{R_{sif\ 200}} = 1.30, \text{ and} \quad (5.8)$$

$$\frac{R_{sec\ 35}}{R_{sec\ 200}} = 1.36. \quad (5.9)$$

The similar values show that the Beer-Lambert law is suitable for considering the atmospheric aerosols and is consistent with the quantum parameters observed from the channel. One of the reasons is the linear dependence of sifted key rate on the coincidences observed per second. Moreover, the free space channel does not introduce any polarization changes to the photons [165, 166]. To obtain the key rates for any other day, the new factor f need to be calculated from Eqn. 5.6 and similarly the other parameters can be obtained using Eqns 5.7.

To determine the secure key, the time tags for all the eight channels have been recorded using the eight-channel digital oscilloscope (Tektronix MSO68B 6-BW-2500). The oscilloscope has a bandwidth of 2.5 GHz, and it was used to record the TTL pulses coming from single-photon detectors with a sampling rate of 1.25 GS/s with an integration time of 40 ms to measure the key rate. The recorded data contains the voltage sample, and from that, the rising edge of TTL pulses provides the arrival time. The post-processing includes basis reconciliation, error estimation, error correction, and privacy amplification, which are implemented in MATLAB. We have implemented a low-density parity-check (LDPC) error correction code [167] with a code rate of 0.5 for error correction. Choice of LDPC matrices closely depends on QBER and directly affects the secure key rate. Higher QBER means it takes more parity bits to correct those errors and thus, reduces the key rate.

Once error-corrected keys are generated, privacy amplification [168] is done via 2-universal Toeplitz hash function. During privacy amplification, the length of the hashed output is chosen pertaining to the parity bits used in error correction, QBER,

and security parameter which decides the final length of the secure key.

5.4 Conclusion

In conclusion, we have implemented, BBM92 protocol, an entanglement-based QKD protocol, over 35 m and 200 m free-space atmospheric channel, and simultaneously studied the effect of aerosols on the secure key rate. This is the first study of its kind where the extinction coefficient of atmospheric aerosols is used to study the variation of entanglement, QBER, and key rate. We also found that the key rate follows the extinction coefficient of the atmospheric aerosols on that particular day. As the key rate depends on the channel length, the larger the channel, the smaller will be the key rate. Further experiments are planned to study the effect for longer duration and to check the validity of models for estimating the key rate due to atmospheric conditions for the satellite-based quantum communications [169]. The presented results may find application in setting up quantum communication network using satellites and the placement of entangled photo-pair sources.

Chapter 6

Engineering higher dimension entanglement

Entanglement is not one but rather the characteristic trait of quantum mechanics

-Erwin Schrodinger

6.1 Introduction

Qubit entanglement or two dimensional entanglement has been used in many quantum information protocols.[165, 166, 170]. Using d-dimensional or qudit entanglement over qubit enables access to larger Hilbert space [171] and is a valuable resource for secure and efficient quantum information processing [172]. In recent years, entanglement of more than two-dimensions has attracted interest owing to a larger information capacity [35–37]. It provides the best security in quantum information protocols which cannot be matched using qubit based system. Higher dimensional entangled state (HD-ES) can be constructed in many of the photon's degrees of freedom (DOFs)

for example, in orbital angular momentum (OAM), path, frequency, photon number and temporal modes. HD-ES in OAM has been gaining more attention due to their easy scalability in dimension [173, 174].

The most commonly method to generate OAM entanglement is spontaneous parametric down-conversion (SPDC) process. In this process, one high energy photon creates two low energy photons named signal and idler via second order nonlinear process. According to OAM conservation law, OAM of the pump photon should be equal to the sum of the signal and idler photon's OAM ie. $m_p = m_s + m_i$, where m_p , m_s and m_i is the OAM of pump, signal, and idler respectively. The photon pair generated through SPDC shows infinite dimensional entangled state in OAM degree of freedom. Dimensionality of the entanglement can be adjusted by the choice of basis selection. Output of the SPDC process can be written as $\sum C_{m_s, m_i} |m_s\rangle |m_i\rangle$ followed by OAM conservation law. Here C_{m_s, m_i} is the probability amplitude for the occurrence of the state $|m_s\rangle |m_i\rangle$. The width of the OAM spectrum is known as spiral bandwidth (SB) [175]. For the maximally entangled state (MES), $C_{m_s, m_i} = 1/\sqrt{d}$ where d is the dimensionality of the entangled state. The higher dimensional entangled states can be achieved by controlling the spiral bandwidth of two photons generated through SPDC process [176].

6.2 Orbital angular momentum of light

Laguerre-Gaussian (LG) beams carry a well defined orbital angular momentum [177]. LG beams are characterized by a radial index and an azimuthal index. These are phase singular beams and has a helical transverse phase profile. Mathematically, these are

represented by,

$$LG_m^p(r, \phi) = \frac{C_{m,p}}{w} \left(\frac{r\sqrt{2}}{w} \right)^{|m|} L_{|m|}^p \left(\frac{2r^2}{w^2} \right) \exp \left(-ik \frac{r^2}{2R} \right) \exp \left(-\frac{r^2}{w^2} \right) \exp(-im\phi) \quad (6.1)$$

where $\{r, \phi\}$ are polar coordinates, p is the radial index and m is the azimuthal index of the Laguerre polynomial represented by $L_{|m|}^p$, $C_{m,p}$ is the mode amplitude, k is the magnitude of wave vector, w and R are the beam waist and radius of curvature of the wavefront respectively. Unlike the wavefront of a plane wave, the wavefront of LG beams are helical in shape as shown in Figure 6.1 and the twisting of helix is described by the parameter, known as topological charge, m . In Eqn. 6.1, azimuthal phase term

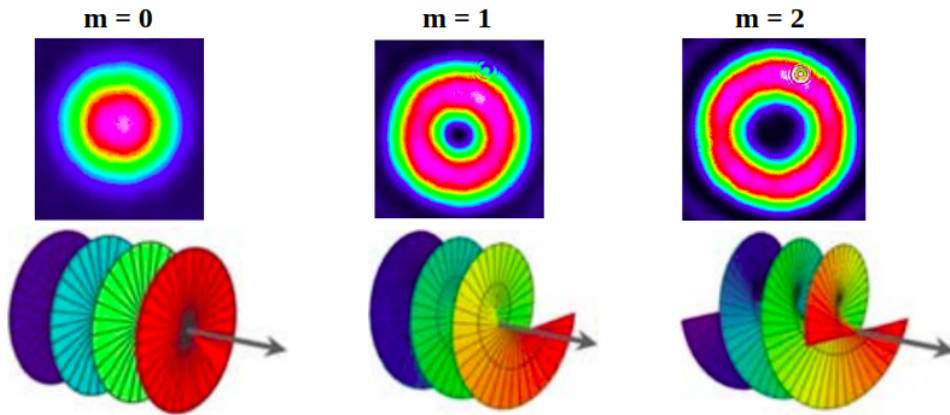


Figure 6.1: Intensity distribution and wavefront of optical vortices of order $m = 0, 1,$ and 2

$e^{-im\phi}$ describes m -intertwined helical phase structure where the energy flows spirally around the beam axis during the propagation. The transverse profile of these beams (assuming radial index $p = 0$ for simplicity) are characterised by a hollow centre surrounded by a bright ring, that is why these beams are also known as optical vortices (OV). The radius of the bright ring increases with increasing azimuthal index. Intensity and phase distribution of LG mode of order $m = -2, -1, 0, 1, 2$ is shown in Figure 6.2. The order of LG mode can be +ve or -ve depending upon the direction of energy flow.

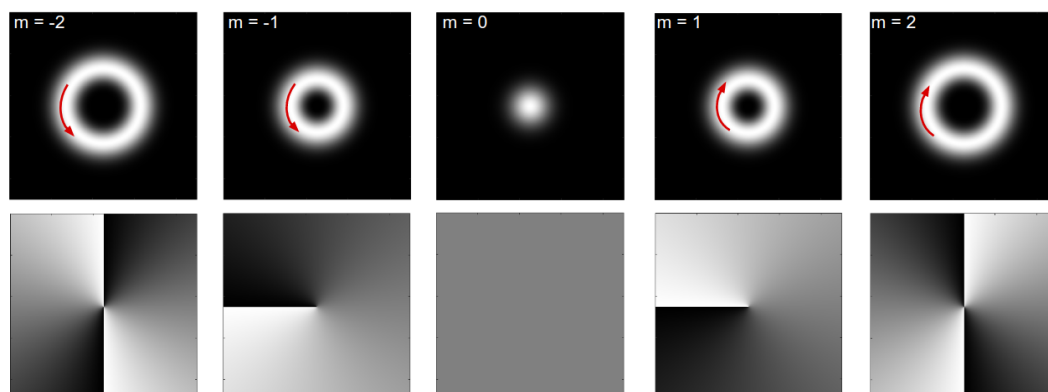


Figure 6.2: Intensity (top row) and phase distribution (bottom row) of various LG modes. The red curved arrow shows the direction of energy flow of vortex around the beam axis

The bottom row of Figure 6.2 shows the phase jump of of the vortex beam. There are $2\pi m$ phase jumps for LG mode of order m .

6.2.1 Generation of OAM carrying light beam

There are mainly three methods to generate OAM modes of light:

- Spiral phase plate (SPP)
- Computer generated holograms (CGH)
- Spatial light modulators (SLM)

Spiral phase plate (SPP)

Spiral phase plates (also known as ‘vortex lens’) are used to generate vortex beams. These SPPs are constructed from the pieces of dielectric material in the form of transparent disc whose thickness varies in a spiral pattern with azimuthal angle [178]. The spirally varying thickness will imprint a phase gradient on light passing through it.

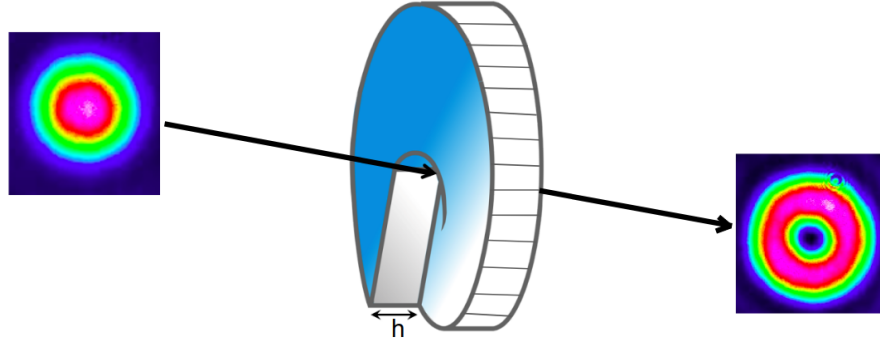


Figure 6.3: Generation of optical vortex beam using SPP

For a given wavelength λ , the azimuthal phase shift is given by,

$$\delta = \frac{(n-1)t}{\lambda} \phi \quad (6.2)$$

where t is the optical thickness at an azimuthal angle ϕ and n is the refractive index of SPP material. When the total phase shift around the SPP is $2\pi m$, where m is an integer, then the output beam will have an OAM $m\hbar$. In Eqn 6.2, for $\phi = 2\pi$ thickness t will be maximum. The maximum optical thickness ('step height') h can be written as,

$$h = \frac{m\lambda}{n-1} \quad (6.3)$$

Computer generated holograms (CGH)

The second method to generate vortex beam is phase holograms. Computer generated holograms (CGHs) are the diffraction gratings printed on a transparent holographic sheet [179]. The diffraction gratings are the interference pattern formed by a reference plane wave and the object beam that has to be generated. When the object beam is the Laguerre-Gauss (LG) beam, the interference pattern or hologram looks like a fork pattern.

The superposition of a plane wave and an object beam is often known as field transmission function and it is written as,

$$f(x, y) = \exp(ik_x x) + \exp(im\phi), \quad (6.4)$$

where k_x is the x -component of the wave-vector, m is the order of the object LG beam and $\phi = \tan^{-1}(y/x)$. The pattern imprinted on the transparent holographic sheet is proportional to,

$$g(x, y) = |f(x, y)|^2 \quad (6.5)$$

$$= 2(1 + \cos(k_x x \pm m\phi)). \quad (6.6)$$

The Eqn. 6.6 results in an interference pattern with a fork kind of dislocation (Figure 6.4). When the hologram of order m is illuminated with Gaussian beam, an optical

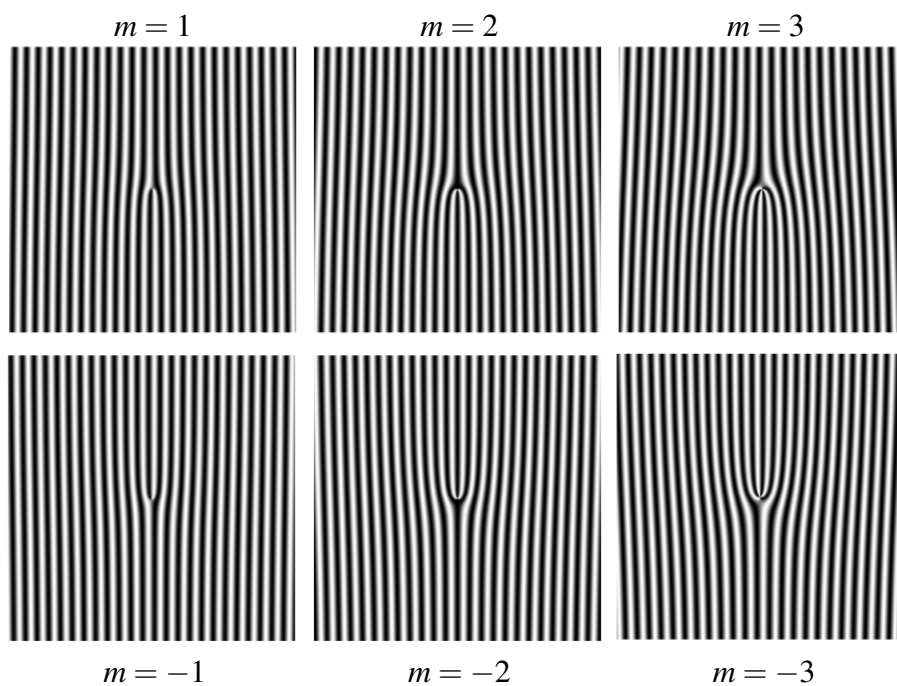


Figure 6.4: Computer generated holograms for LG mode of order $m = \pm 1, \pm 2, \pm 3$

vortex of order m is formed at the first diffraction order.

Spatial light modulators (SLM)

Spatial light modulator (SLM) is a device that can modulate amplitude and phase of the light beam spatially. One can imprint the hologram pattern on the SLM and can easily generate the vortex beam [180]. Phase change is achieved by layers of liquid crystals (LC) trapped between pixelized electrodes on CMOS chip, which enable each layer of liquid crystals to align in a particular direction (Figure 6.5). This modulator is then set between a transparent plate and a silicon plate, so that the light is reflected back in the same direction. The computer generated hologram (CGH) is transferred

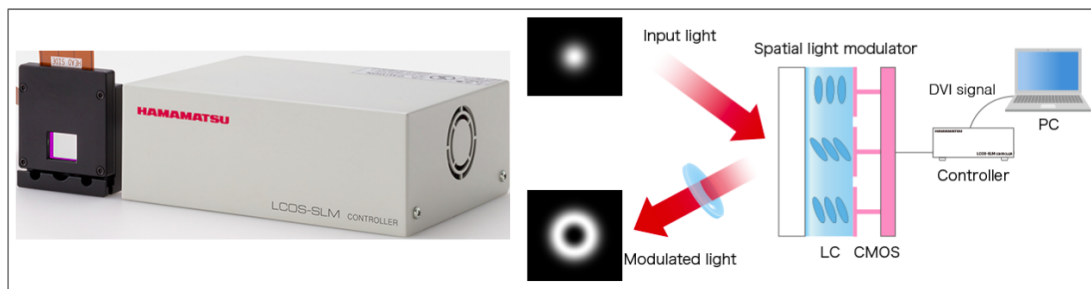


Figure 6.5: Working principle of spatial light modulator (SLM)

into the SLM through a computer. The graphics card installed in computer generates a video signal corresponding to the desired CGH. The electric field of the video signal changes the refractive index of the liquid crystal molecules and aligns them to form a desired hologram. When the SLM is illuminated by a laser beam, an optical vortex is generated at the first diffracted order.

6.2.2 Detection of OAM

There are various methods to detect and analyse the OAM content of light:

- Phase-flattening technique [181]
- Tilted-lens technique [182]
- Double-slit interference technique [183]
- Interferometry technique [184]

Among all these techniques, the phase-flattening technique is the easiest way to analyse the OAM content of light and it works well in classical as well as in quantum domain. The idea is to flatten the azimuthal phase of the input beam via projective measurement. In this technique, when the input LG beam of order m is projected onto a conjugate LG mode of order $-m$ using a SLM, then the helical phase of the input beam is cancelled by the forked grating of conjugate mode on the SLM. Due to azimuthal phase cancellation, a Gaussian mode is generated at the far-field intensity distribution. The Gaussian mode can be coupled into the single mode fiber (SMF) for the detection of OAM content of input LG mode. This method is known as ‘Phase flattening’.

6.3 Generation of OAM entanglement

SPDC process follows OAM conservation law which means that ‘sum of the OAM of signal and idler photon (m_s and m_i) must be equal to the OAM of pump photon (m_p)’.

$$m_p = m_s + m_i, \quad (6.7)$$

The photon pairs generated through SPDC maintain OAM correlation which leads to the OAM entanglement [31]. The output of the SPDC process in OAM degree of

freedom can be written as,

$$|\Psi\rangle_{\text{spdc}} = \sum_{m_s=-\infty}^{+\infty} C_{m_s, m_p - m_s} |m_s\rangle |m_p - m_s\rangle, \quad (6.8)$$

where m_p is the OAM of the pump photon and m_s is the OAM of the signal photon. The OAM of the idler photon is calculated from the conservation equation $m_p = m_s + m_i$ which gives $m_i = m_p - m_s$. The normalized expansion coefficient $C_{m_s, m_p - m_s}$ is the probability amplitude for the creation of the photon pair carrying OAM $m_s\hbar$ and $(m_p - m_s)\hbar$. It can be calculated by projecting the conjugate azimuthal modes in signal and idler photons:

$$C_{m_s, m_p - m_s} = \langle m_s | \langle m_p - m_s | \Psi_{\text{spdc}} \rangle, \quad (6.9)$$

For a Gaussian pump $m_p = 0$, the two photon state in the OAM basis is given by,

$$\begin{aligned} |\Psi\rangle_{\text{spdc}} = & C_{0,0} |0\rangle_s |0\rangle_i + C_{1,-1} |1\rangle_s |-1\rangle_i + C_{-1,1} |-1\rangle_s |1\rangle_i \\ & + C_{2,-2} |2\rangle_s |-2\rangle_i + C_{-2,2} |-2\rangle_s |2\rangle_i + \dots \end{aligned} \quad (6.10)$$

Eqn. 6.10 represents the multi-dimensional OAM entangled state of two photons. Photon pairs in SPDC process are the coherent superposition of many different OAM values allowed by the conservation of orbital angular momentum. It means that none of the photon in state (Eqn. 6.10) possess a well defined OAM after SPDC process. To measure the OAM of the twin photon, signal and idler, one has to use phase flattening technique. This will give a number of coincidence counts for photon pairs to be in a particular OAM state $|m\rangle_s |-m\rangle_i$. The probability of detecting both the photons in $|m\rangle_s |-m\rangle_i$ and $|-m\rangle_s |m\rangle_i$ state is equal,

$$C_{m_s, -m_i} = C_{-m_s, m_i}. \quad (6.11)$$

Before measuring the OAM entanglement of the photon pairs, first we have to confirm that SPDC conserves orbital angular momentum. Then we show that the OAM correlation obtained from the SPDC process can not be explained by classical correlation.

6.3.1 Experimental setup

The basic experimental setup for the generation and measurement of OAM correlation is given in Figure 6.6. To confirm the OAM conservation in SPDC process we

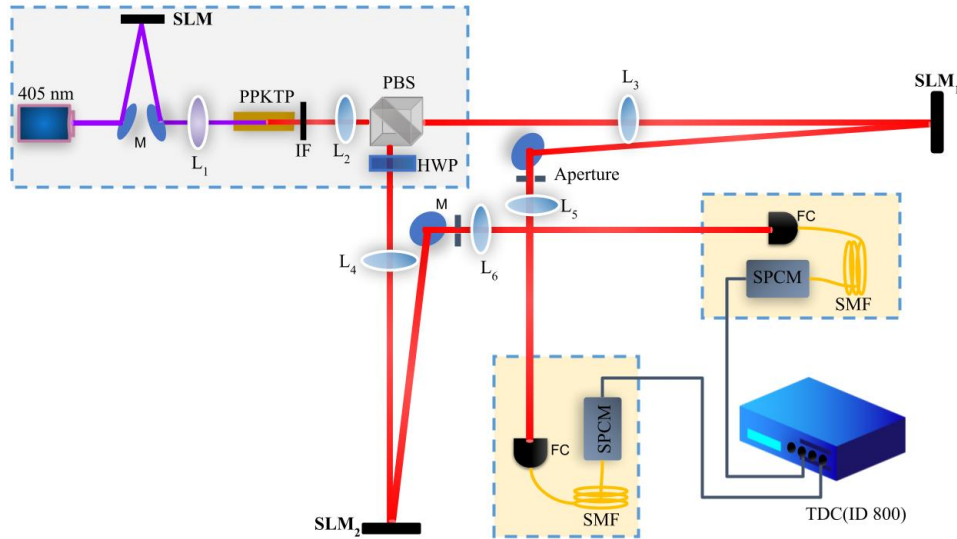


Figure 6.6: Experimental setup for measuring the OAM correlation in SPDC. SLM is used to change the spatial mode of Pump. Lens L_1 is used to focus the pump at the center of Type-II PPKTP crystal.

used three different cases with the pump photon having three different OAM values $-\hbar$, 0 , and $+\hbar$. An ultra violet (UV) diode laser of wavelength 405 nm is used to pump the second order nonlinear Type-II PPKTP crystal of length 30 mm. SLM (Hamamatsu, LCOS-SLM) is used to change the pump orbital angular momentum. Lens L_1 is used to focus the pump at the center of the crystal to generate twin photons, signal and idler. A interference filter (IF) (810 ± 5) nm is used to block the pump beam after the crystal and pass down the signal and idler of wavelength 810 nm. Both the

photons, signal and idler, split into two different directions after passing through the PBS. These signal and idler photons then are imaged to the SLM₁ and SLM₂ using 4f-imaging. SLM₁ and SLM₂ are used to do projective measurement by projecting the signal and idler to a conjugate LG mode so that resultant output will become Gaussian. The SLM plane is imaged to the fiber couplers (FC) in each arm. The fiber coupler are attached to the SMF which are then connected to the single photon counting module (SPCM-AQRH-16-FC, Excelitas). Both the SPCMs are connected to the coincidence counter (IDQ quantique ID800) to measure number of correlated photon pairs.

6.3.2 Results

We first study the OAM spectrum for the pump beam carrying OAM $-\hbar$, 0 , and $+\hbar$. Figure 6.7 shows the experimentally measured coincidence counts per second by performing the projective measurement of OAM in signal and idler arms ranging from $m = -4$ to $+4$. The diagonal element of OAM spectra is consistent with OAM con-

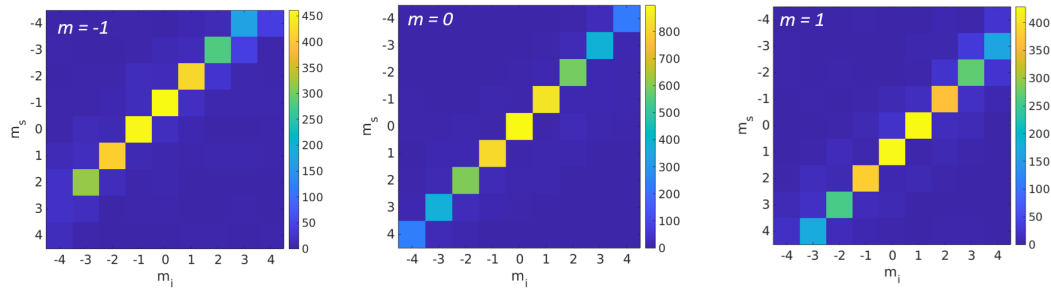


Figure 6.7: Experimentally measured OAM correlation in SPDC for the pump having (a) $m = -1$ (b) $m = 0$, and (c) $m = 1$

servation. We observed that for the Gaussian pump, signal and idler photons always carry equal and opposite OAM charge so that the net OAM becomes zero. But the probability is maximum for the combined twin photon state $|0\rangle_s |0\rangle_i$. In case of pump beam being in LG mode of order ± 1 , the maximum probability shifted to the state

$|\pm 1\rangle_s |0\rangle_i$ and $|0\rangle_s |\pm 1\rangle_i$.

Since the output of SPDC process gives a multi-dimensional entangled state where the OAM value can run from $-\infty$ to $+\infty$. Therefore, qubits in OAM space can be considered as qudits. But the demonstration of OAM entanglement for multi-dimension is a complicated task. Therefore, for the simplicity, we selected a two dimensional OAM subspace from the infinite OAM Hilbert space via post selection. Using Eqn. 6.10 for the Gaussian pump, the qubit OAM entangled state can be obtained by applying projection operator on state $|\Psi\rangle_{\text{SPDC}}$,

$$\begin{aligned} |\Psi\rangle_{\text{ent}} &= (|1\rangle_s | -1\rangle_i \langle 1|_s \langle -1|_i + | -1\rangle_s |1\rangle_i \langle -1|_s \langle 1|_i) |\Psi\rangle_{\text{SPDC}} \\ &= C_{1,-1} |1\rangle_s | -1\rangle_i + C_{-1,1} | -1\rangle_s |1\rangle_i, \end{aligned} \quad (6.12)$$

Since in SPDC process, $C_{1,-1} = C_{-1,1}$, therefore

$$|\Psi\rangle_{\text{ent}} = \frac{1}{\sqrt{2}} (|1\rangle_s | -1\rangle_i + | -1\rangle_s |1\rangle_i). \quad (6.13)$$

The Eqn. 6.13 is a two-qubit OAM entangled state in ± 1 OAM basis.

6.4 Engineering higher dimension entangled state

A state with more than two dimensions is known as qudit. Unlike qubit which has only two states $|0\rangle$ and $|1\rangle$, qudit has $|0\rangle, |1\rangle, |2\rangle, \dots, |d-1\rangle$ states. A Single qudit state can be written as,

$$|\Psi\rangle = C_0 |0\rangle + C_1 |1\rangle + C_2 |2\rangle + \dots + C_{d-1} |d-1\rangle, \quad (6.14)$$

where

$$|C_0|^2 + |C_1|^2 + |C_2|^2 + \dots + |C_{d-1}|^2 = 1, \quad \langle i|j \rangle_{i \neq j} = 0, \quad i, j = 0, 1, 2, \dots, d-1 \quad (6.15)$$

The information of the states $|0\rangle, |1\rangle, |2\rangle, \dots, |d-1\rangle$ is stored in the amplitude coefficients $C_0, C_1, C_2, \dots, C_{d-1}$.

The two-qudit entangled state can be written as,

$$|\Psi\rangle_{\text{HD-ES}} = \sum_{j=0}^{d-1} C_{jj} |j\rangle_s |j\rangle_i, \quad (6.16)$$

For the maximally entangled state, the value of the amplitude coefficient C_{jj} must be equal for each state i.e.

$$C_{jj} = \frac{1}{\sqrt{d}}. \quad (6.17)$$

The photon pairs generated through SPDC show in principle infinite dimensional entangled state in OAM degree of freedom. Dimensionality of the entanglement is decided by the selection of bases. The output of the SPDC process can be written as $\sum C_{m_s, m_i} |m_s\rangle |m_i\rangle$ based on the conservation of OAM. Here C_{m_s, m_i} is the probability amplitude for the occurrence of the state $|m_s\rangle |m_i\rangle$. The number of the OAM modes generated in SPDC process is known as spiral bandwidth (SB), which is obtained from the full-width-half-maximum (FWHM) of the OAM spectrum. Since for the maximally entangled state (MES), $C_{m_s, m_i} = 1/\sqrt{d}$, therefore to achieve a desired d-dimensional entangled state, one has to broaden the spiral bandwidth of two entangled photons such that the value of amplitude coefficient C_{m_s, m_i} for the d-dimension OAM basis becomes $1/\sqrt{d}$.

6.4.1 Controlling OAM spectrum of two photon entangled state

For generating a d-dimensional entangled state, OAM is one of the natural choice of the bases. As it is known, the SPDC photons are entangled in OAM degree of freedom,

$$|\Psi\rangle_{spdc} = \sum_{m_s} C_{m_s, m_i} |m_s\rangle |m_i\rangle, \quad (6.18)$$

In order to control the OAM spectrum of SPDC photons, we need to calculate C_{m_s, m_i} . The amplitude coefficient C_{m_s, m_i} can be written as an overlap integral of pump, signal and idler field,

$$C_{m_s, m_i} = \int \int dk_{s\perp} dk_{i\perp} \Phi(k_{s\perp}, k_{i\perp}) [LG_{m_s}(k_{s\perp})]^* [LG_{m_i}(k_{i\perp})], \quad (6.19)$$

where $LG_{m_s}(k_{s\perp})$ and $LG_{m_i}(k_{i\perp})$ are Laguerre-Gaussian (LG) mode profile of signal and idler (Eqn. 6.1). $k_{s\perp}$ and $k_{i\perp}$ are the transverse wave vectors of signal and idler that satisfies the momentum conservation,

$$k_{p\perp} = k_{s\perp} + k_{i\perp}, \quad (6.20)$$

The above integral of C_{m_s, m_i} depends on the momentum co-ordinates of signal and idler. The pump beam profile and the phase matching condition is included in the Φ -function $\Phi(k_{s\perp}, k_{i\perp})$ and it can be written as,

$$\Phi(k_{s\perp}, k_{i\perp}) = E(k_{s\perp} + k_{i\perp}) W(k_{s\perp}, k_{i\perp}), \quad (6.21)$$

where $W(k_{s\perp}, k_{i\perp})$ shows the phase matching condition and is given by,

$$W(k_{s\perp}, k_{i\perp}) = \sqrt{\frac{2L}{\pi^2 k_p}} \operatorname{sinc}\left(\frac{L|k_{s\perp} - k_{i\perp}|^2}{4k_p}\right) \exp\left(-i\frac{L|k_{s\perp} - k_{i\perp}|^2}{4k_p}\right), \quad (6.22)$$

where L is the length of the crystal. $E(k_{s\perp} + k_{i\perp})$ is the Fourier transform of the spatial distribution of pump profile at the input face of the crystal and is given by,

$$E(k_{s\perp}, k_{i\perp}) = \frac{w_p}{\sqrt{2\pi}} e^{-\frac{w_p^2}{4}|k_{s\perp} + k_{i\perp}|^2}, \quad (6.23)$$

where w_p is the pump beam waist. Now using Eqn. 6.22 and 6.23 in Eqn. 6.21, the function $\Phi(k_{s\perp}, k_{i\perp})$ can be rewritten as,

$$\Phi(k_{s\perp}, k_{i\perp}) = \frac{w_p}{\sqrt{2\pi}} e^{-\frac{w_p^2}{4}|k_{s\perp} + k_{i\perp}|^2} \sqrt{\frac{2L}{\pi^2 k_p}} \text{sinc}\left(\frac{L|k_{s\perp} - k_{i\perp}|^2}{4k_p}\right) \exp\left(-i\frac{L|k_{s\perp} - k_{i\perp}|^2}{4k_p}\right), \quad (6.24)$$

After solving the above equation for Gaussian pump profile, we will get

$$|C_{m_s, -m_i}|^2 \propto \left(\frac{2\gamma_i \gamma_s}{1 + \gamma_i^2 + \gamma_s^2}\right)^{2|m|}, \quad (6.25)$$

where γ_s (and γ_i) is the ratio between pump waist and signal waist w_p/w_s (and w_p/w_s). If we further choose the beam waist of signal and idler to be equal then $\gamma_s = \gamma_i = \gamma$ and the above equation simplifies to [176],

$$|C_{m_s, -m_i}|^2 \propto \left(\frac{2\gamma^2}{1 + 2\gamma^2}\right)^{2|m|}. \quad (6.26)$$

This shows that for a given nonlinear crystal and pump profile, the amplitude coefficient $C_{m_s, -m_i}$ depends on the length of the crystal (L), the pump beam waist w_p and the chosen waist of the LG mode (w_s and w_i). Through the normalization of Eqn. 6.26, it turns out that the amplitude can be shown to depend on the normalized parameter [175],

$$\bar{w}_p = \frac{w_p}{\sqrt{\lambda_p L}} \quad (6.27)$$

where λ_p is the wavelength of the pump beam. The amplitude coefficient $C_{m_s, -m_i}$ is directly proportional to w_p and inversely proportional to w_s and w_i . Thus, larger pump waist (or smaller signal and idler waist) increases the size of the spiral bandwidth of two photon entangled state. Therefore, by manipulating the pump beam waist at the center of the crystal, one can achieve $C_{m_s, -m_i} = 1/\sqrt{d}$ for d-dimensional entangled state.

6.4.2 Results and discussion

In our experiment (Figure 6.6), the wavelength of the pump is $\lambda_p = 405$ nm, and the crystal length is $L = 30$ mm. Therefore a pump beam waist of $w_p = 110$ μm corresponds to a normalized value of $\bar{w}_p = 1$. This gives an important scaling rule for spiral bandwidth. Now we want to see the effect of pump beam waist on the size of spiral bandwidth. For this we recorded the coincidence counts of photon pair generated in SPDC process for various pump waist. The probability of detecting the photon pair in $|m_s\rangle |m_i\rangle$ state is given by:

$$P_{m_s, m_i} = |C_{m_s, m_i}|^2 \quad (6.28)$$

We plotted the OAM spectrum of two photon state for Gaussian pump shown in Figure 6.8. We observe that the size of OAM spectrum increases by increasing the pump waist w_p . This means that that the number of higher OAM modes are increasing during the SPDC process with w_p . The reason behind the change in size of OAM spectrum can be explained as follows: The relation between angular momentum (m) and linear momentum (p) is given by,

$$m = r \times p, \quad (6.29)$$

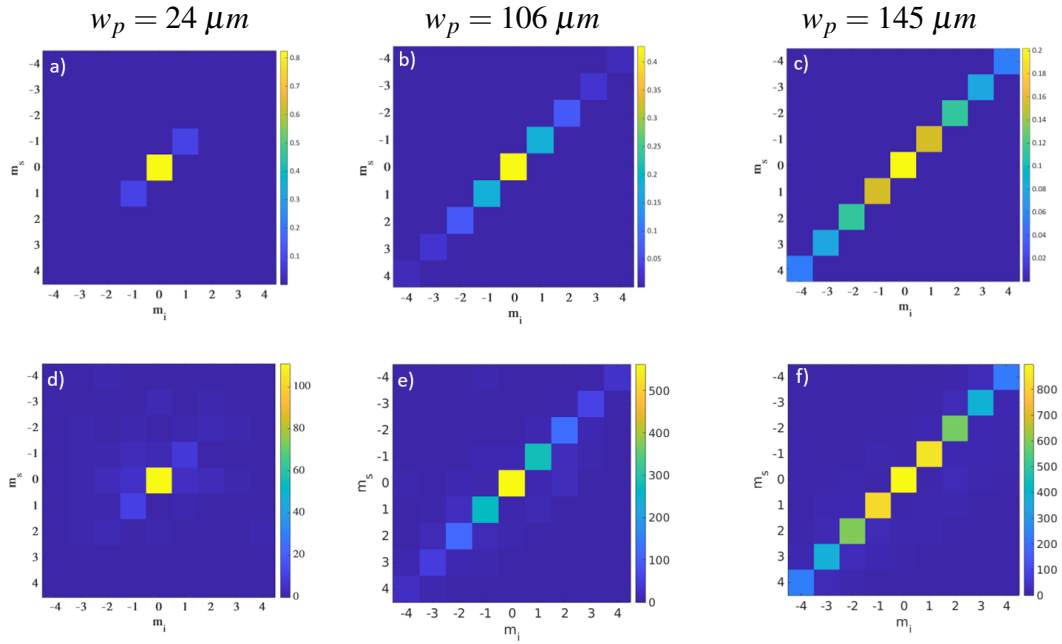


Figure 6.8: Bottom row (d-f) shows experimentally recorded OAM spectrum of signal and idler for different pump waist of Gaussian mode and top row (a-c) is corresponding theoretical results. OAM spectrum is expanding with pump waist

where r is the radial co-ordinate and linear momentum p can be written in terms of wave vector k ,

$$p = \hbar k, \quad (6.30)$$

Let's consider two different cases, narrow beam waist and large beam waist. When we pump the center of the crystal with narrow beam waist then this implies that there is a smaller spread in the momentum space inside the crystal. This means that uncertainty in the momentum is also small. This reduced uncertainty in the momentum leads to the reduced uncertainty in angular momentum space (Eqn. 6.29),

$$\begin{aligned} \Delta m &= r \times \Delta p \\ &= r \times \hbar \Delta k. \end{aligned} \quad (6.31)$$

This shows that uncertainty in angular momentum is directly proportional to the uncertainty in linear momentum. Similarly, for larger pump waist, the uncertainty in momentum space will also be larger at the center of the crystal. This leads to the larger distribution of OAM spectrum which satisfies conservation of momentum.

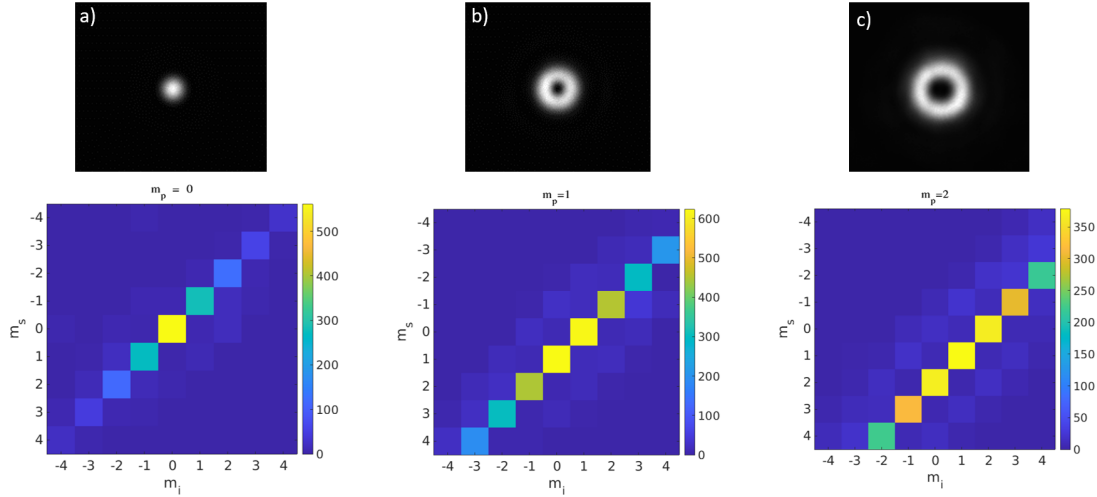


Figure 6.9: (Bottom row) Experimentally observed OAM spectrum (Bottom row) for (a) Gaussian pump with $w_p = 106\mu\text{m}$ (b) LG mode of order 1 with $w_p = 196\mu\text{m}$ and (c) LG mode of order 2 with $w_p = 267\mu\text{m}$

Since the size of the LG mode increases with order, therefore OAM spectrum also expands with order of the LG mode. Figure 6.9 shows the expansion of OAM spectrum for LG mode $m = 0, 1, 2$. In this case, the size of the Gaussian beam is $w_p = 106\mu\text{m}$ and size of the LG mode of order 1 and 2 is $196\mu\text{m}$ and $267\mu\text{m}$ respectively. The narrowest OAM spectrum can be achieved for,

$$\begin{aligned} w_p &= \sqrt{\frac{L}{k_p}} \\ &= \sqrt{\frac{\lambda L}{2\pi}}. \end{aligned} \quad (6.32)$$

In our case, for $L = 30\text{ mm}$, $\lambda = 405\text{ nm}$, the beam size is $w_p = 32.4\mu\text{m}$. Any LG mode with beam size $w_p = 32.4\mu\text{m}$ gives a narrow OAM spectrum. We chosen beam

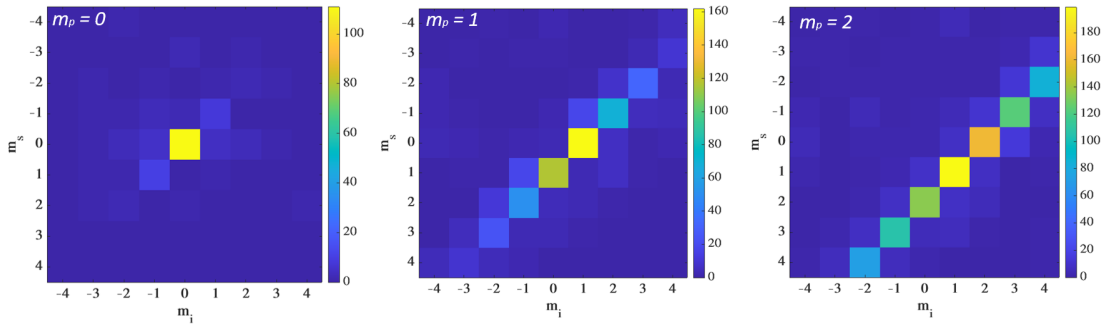


Figure 6.10: Observed OAM spectrum for narrow beam waist for $m = 0, 1, 2$. Size of OAM spectrum is expanding for higher order OAM. Here beam waist of Gaussian pump is $24 \mu\text{m}$.

waist of $24 \mu\text{m}$ for Gaussian mode, and recorded the spectrum as shown in Figure 6.10. Since the beam size differs for different order of LG mode, that is why the spectrum started expanding as we move to higher order pump mode (Figure 6.10). Since from Eqn 6.32, OAM spectrum is narrow for $32 \mu\text{m}$ pump waist, therefore, for this beam size, if we choose the pump beam as a coherent superposition of LG mode $|\Psi\rangle_{\text{pump}} = \sum_m C_m |m\rangle$ then we can achieve a pure d-dimension OAM entangled state. Here we opted $m = 0, 2$ and -2 with narrow beam waist in order to achieve a pure qutrit entangled state. Pump input state is given by,

$$|\Psi\rangle_{\text{pump}} = C_0 |0\rangle + C_2 |2\rangle + C_{-2} |-2\rangle, \quad (6.33)$$

When the narrow pump beam with superposition of $m = 0, \pm 2\hbar$ incidents on the non-linear crystal, the output state will become,

$$|\Psi\rangle_{\text{SPDC}} = \frac{1}{\sqrt{3}} (|0\rangle_s |0\rangle_i + |1\rangle_s |1\rangle_i + |-1\rangle_s |-1\rangle_i) \quad (6.34)$$

This is a 3-dimensional two qutrit entangled state in $m = 0, \pm 1$ basis. The experimentally recorded OAM spectrum for the pump superposition state given in Eqn 6.33 is shown in Figure 6.11. Now since the size of the beam increases with the order of

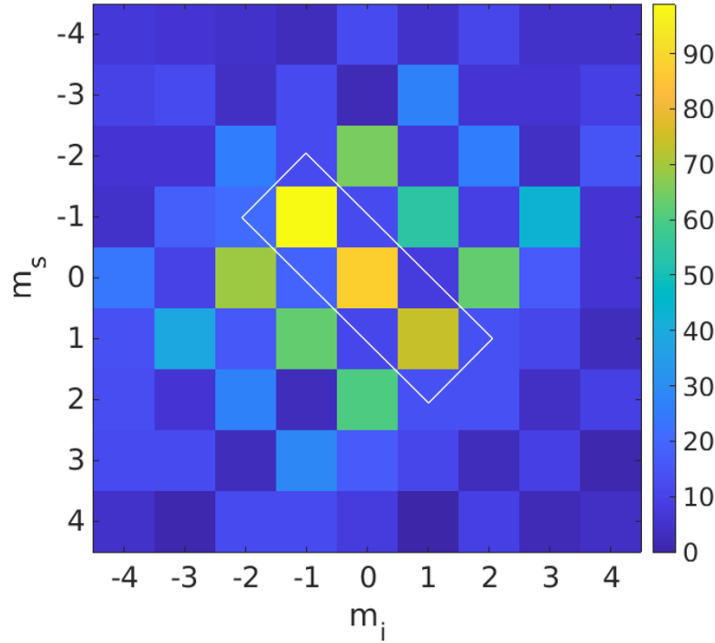


Figure 6.11: Generation of qutrit entangled state using narrow pump waist with superposition of Gaussian mode ($m = 0$) and LG mode ($m = \pm 2\hbar$). Higher order OAM are arising due to the waist mismatch of each mode in superposition state of pump.

the LG mode, it is difficult to achieve the same beam waist for each mode in superposition state given in Eqn 6.33. Also the projection and alignment of small beam waist ($w_p = 24 \mu m$) of signal and idler on SLM is little sensitive. That is why other higher order OAM modes are also visible in OAM spectrum of two photon state as shown in Figure 6.11.

6.4.3 Effect of coupling efficiency on OAM spectrum

We also observed that the size of the OAM spectrum can be manipulated by coupling efficiency at the detection stage [185]. Coupling the bi-photon mode in SMF is quantified by coupling efficiency parameter η_{fc} , where fc stand for fiber coupling. η_{fc} is the ratio of the probability to find the pair of photons over a square root of the product of probabilities to find individual signal and idler photon independently. The general

expression for the coupling efficiency for bi-photon mode is given by,

$$\eta_{fc} = \frac{C_{si}}{\sqrt{C_s C_i}} \quad (6.35)$$

In experiment, C_{si} is the coincidence counts of photon pair and C_s , C_i are the single counts of signal and idler respectively. The mode field diameter (MFD) of the SMF

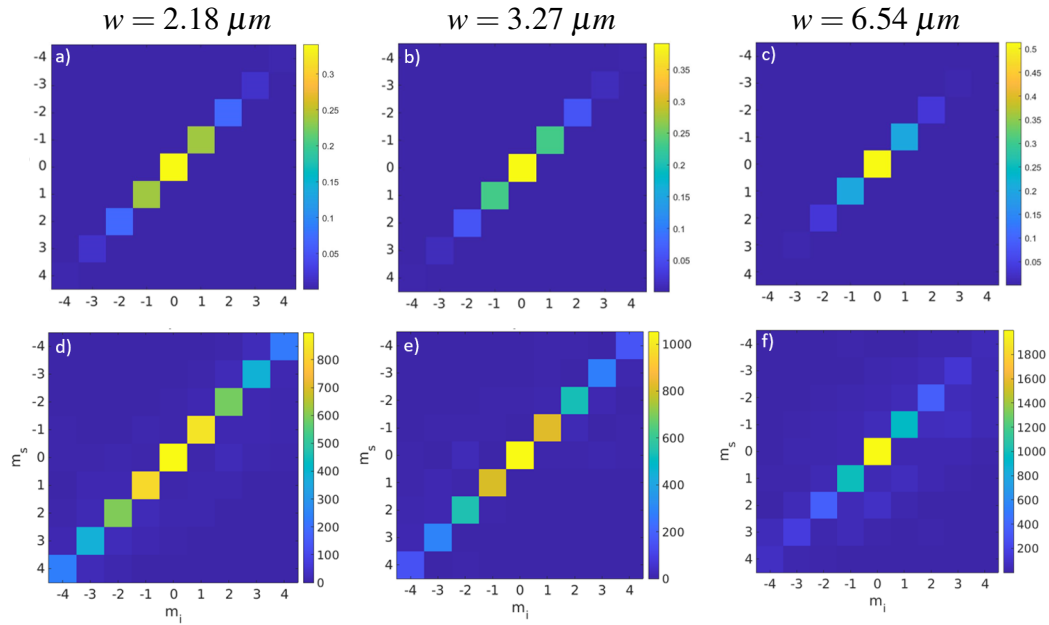


Figure 6.12: Effect of coupling efficiency on OAM spectrum for Gaussian pump for various beam size of signal/idler (w) at fiber position. Mode field diameter (MFD) of SMF is $5 \mu m$. Top row (a-c) shows the theoretical results and bottom row (d-f) shows experimentally recorded data.

used in the experiment is $5 \mu m$. The coupling efficiency η_{fc} depends on the ratio between the beam waist radius of the SMF (σ) and the size of signal/idler waist ($w_s = w_i = w$) at the fiber position,

$$\eta_{fc} \propto \frac{\sigma}{w}, \quad (6.36)$$

The coupling efficiency differs for different OAM modes due to the different beam waist of each mode [181]. In experiment, we use various beam waists of signal and idler at the tip of the SMF to study the effect on OAM spectrum. The size of beam is

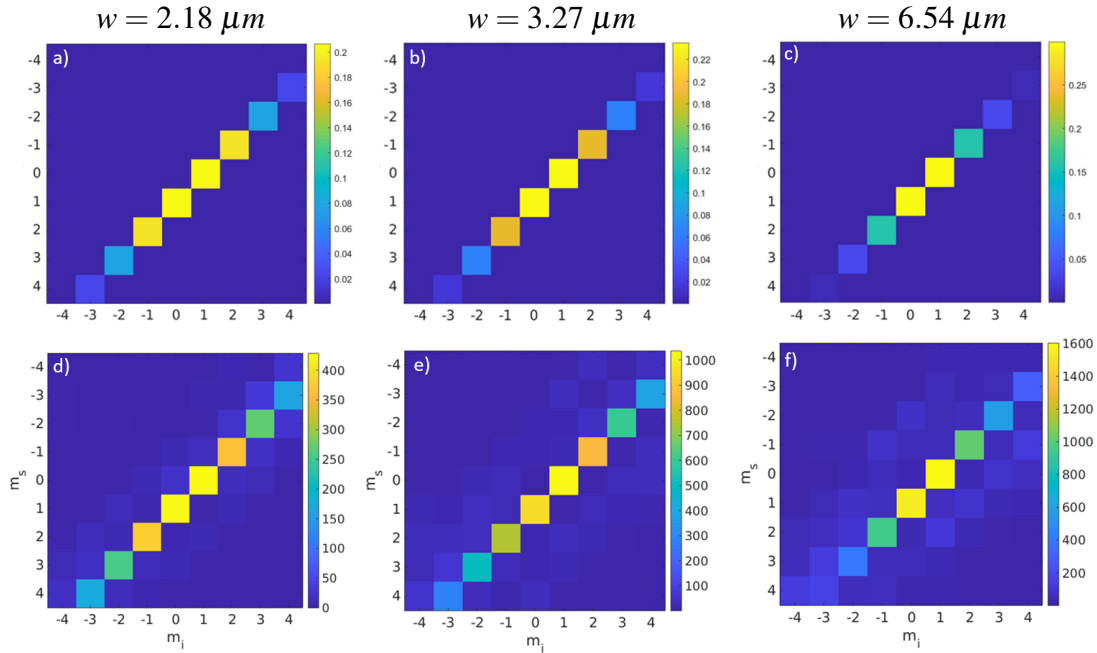


Figure 6.13: Effect of coupling efficiency on OAM spectrum for LG mode pump ($w_p = 150 \mu m$) of order $m = 1$ for various beam size of signal/idler (w) at fiber position. Mode field diameter (MFD) of SMF is $5 \mu m$. Top row (a-c) shows the Theoretical results and bottom row (d-f) shows experimentally recorded data.

controlled with the help of 4f-imaging (Figure 6.6). We recorded the data for the pump beam of order $m = 0$ and 1. The results are shown in Figures 6.12 and 6.13. The beam waist of SPDC photons at the center of the crystal depends upon the pump waist,

$$w_s = w_i = \sqrt{2}w_p, \quad (6.37)$$

Initially, we fixed the beam waist of pump at $150 \mu m$ and demagnified the signal/idler waist at fiber position for the maximum coupling. In the plot shown in Figures 6.12 and 6.13, it is clear that the size of the OAM spectrum is reducing with the increase in the size of signal/idler at fiber position. This happens because the higher order OAM modes will have lesser coupling in comparison to Gaussian mode due to their larger size. Since the coupling efficiency differs for different OAM mode, the measured OAM spectrum does not represent the true OAM distribution of biphoton

mode. Please note that imperfect projection on SLM, Experimental inaccuracies, and statistical fluctuations of coincidence counts may also manipulate the OAM spectrum

6.4.4 Entanglement verification

To verify the entanglement of d-dimension state, qudit state tomography needs to be performed [55]. One can also calculate the CGLMP Bell inequality to verify the entanglement [44]. But as we move towards high dimension state, the number of measurements increases exponentially and performing tomography becomes complicated task. Hence as a proof-of-principle, one can opt the visibility graph to observe the qudit entanglement.

The qutrit entangled state is given by,

$$|\Psi\rangle_{\text{qutrit}} = \frac{1}{\sqrt{3}} \left(|0\rangle_s |0\rangle_i + e^{i\theta} |1\rangle_s |1\rangle_i + e^{i\phi} |-1\rangle_s |-1\rangle_i \right) \quad (6.38)$$

where θ is the relative phase between OAM 0 and 1, and ϕ is the relative phase between OAM 0 and -1. For qubit, we show the visibility graph to verify the entanglement. In the same way, we can verify the qudit entanglement by visibility plot. Consider the qutrit entangled state $|\Psi\rangle_{\text{qutrit}}$ (Eqn. 6.34). If we rotate the OAM state by an angle α then rotated OAM basis can be written as:

$$|jk_\alpha\rangle = \cos \alpha |j\rangle + \sin \alpha |k\rangle \quad (6.39)$$

where j and k are the OAM state ($j \neq k$) and $j, k = 0, 1, -1$. Now probability of coincidence detection is given by,

$$P_{jk,jk}(\alpha, \beta) = |\langle jk_\alpha |_s \langle jk_\beta |_i |\Psi\rangle_{\text{qutrit}}|^2 \quad (6.40)$$

Solving explicitly, we obtain,

$$P_{01,01}(\alpha, \beta) = P_{0-1,0-1}(\alpha, \beta) = P_{1-1,1-1}(\alpha, \beta) = \frac{1}{3} \cos^2(\alpha - \beta) \quad (6.41)$$

For the full state tomography of two qudit entangled state, a total of $[d(2d - 1)]^2$ measurements are required, where d is the dimension of the state. But the process becomes complicated as we move to higher dimension state. We record the coincidence of signal and idler photons by projective measurement. The visibility plot for qutrit entangled state is shown in Figure 6.14 and 6.15. The normalized coincidence

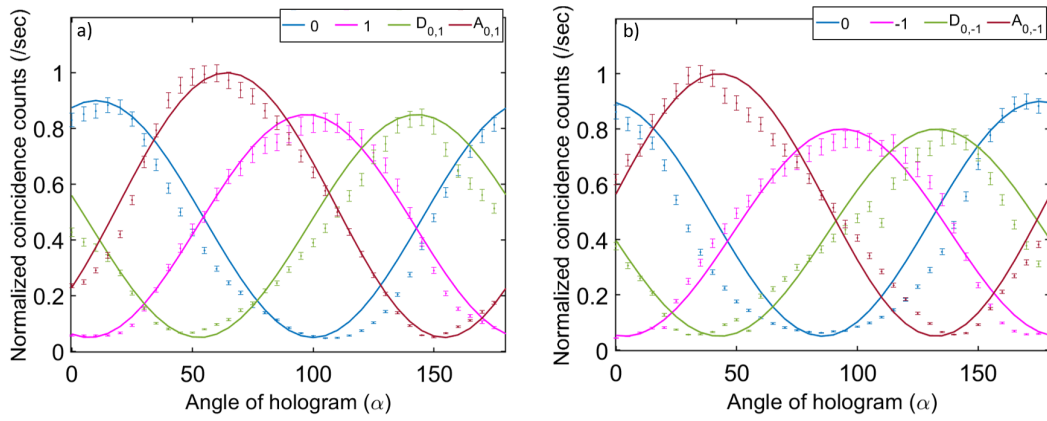


Figure 6.14: Normalized coincidence counts as a function of hologram angle α . The angle of hologram β on SLM₂ is fixed while those on SLM₁ is rotated from 0 to π . OAM correlations are corresponding to a) $m = 0/1$ basis, and b) $m = 0/-1$ basis. The normalized coincidences are plotted along y-axis with the variation of α for $\beta = 0^\circ$ (blue), $\beta = 45^\circ$ (green), $\beta = 90^\circ$ (magenta), and $\beta = 135^\circ$ (red).

counts are plotted in y-axis as function of hologram angle (α). we measure the coincidence counts two OAM basis $m = 0, 1$, and -1 and their superposition basis such as $D_{m_s, m_i}/A_{m_s, m_i}$ and $L_{m_s, m_i}/R_{m_s, m_i}$, where m_s and m_i can have values 0, 1 and -1. For example, $D_{1, -1}$ represents the state $|\psi\rangle = 1/\sqrt{2}(|1\rangle + |-1\rangle)$ and $L_{1, -1}$ represents the state $|\psi\rangle = 1/\sqrt{2}(|1\rangle + i|-1\rangle)$. The average visibility for m_s/m_i , $D_{m_s, m_i}/A_{m_s, m_i}$, and $L_{m_s, m_i}/R_{m_s, m_i}$ basis is recorded to be 88.82%, 87.51%, and 79.68% respectively. CGLMP-Bell's inequality is calculated to be 2.45 ± 0.05 and the entanglement witness

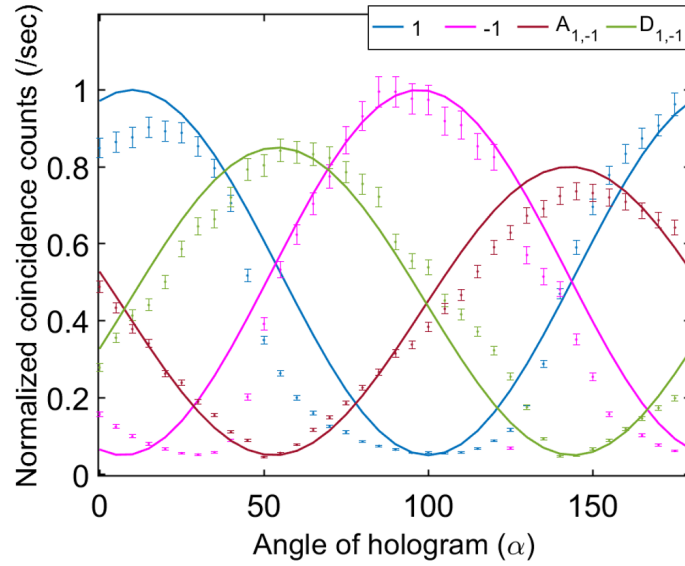


Figure 6.15: Normalized coincidence counts as a function of hologram angle α . The angle of hologram β on SLM₂ is fixed while those on SLM₁ is rotated from 0 to π . OAM correlations are corresponding to $m = 1/-1$ basis. The normalized coincidences are plotted along y-axis with the variation of α for $\beta = 0^\circ$ (blue), $\beta = 45^\circ$ (green), $\beta = 90^\circ$ (magenta), and $\beta = 135^\circ$ (red).

W is estimated to be 1.67. In case of qutrit, a total 225 measurements are required to perform the tomography. Similarly one can generate the ququart entangled state. But the further characterization of entangled state will become more complicated.

6.5 Conclusion

In summary, we have studied the effect of beam waist and fiber coupling on the size of the OAM spectrum of bi-photon state generated through SPDC process. We have experimentally verified that the pump waist play important role in engineering the higher dimension entangled state. We concluded that the larger beam waist (or loosely focused pump beam) is the best choice to get the broad OAM spectrum. We have also shown that the coupling efficiency can easily manipulate the OAM spectrum. The study carried out in this chapter will be very useful in generating better source of qudit entangled state for quantum information processing.

Chapter 7

Scattering of hybrid entangled state

An experiment is the question which science poses to nature, and a measurement is the recording of nature's answer.

-Max Planck

7.1 Introduction

A transmission channel of quantum information could be free-space or optical fibers [186, 187]. The transmission in either of these channels is decided mainly based on the robustness of the photonic degree of freedom along the channel. Polarization qubits suffer decoherence while transmitting through optical fibers, but are faithfully transmitted through atmosphere due to non-birefringent nature. The spatial degree of freedom of photons is affected by atmospheric turbulence [188], but can be effectively transmitted and analysed through a combination of single-mode fibers and a SLM. Thus, a source of photonic hybrid entangled state [43, 53], in which different degrees of freedom of photons are entangled to each other, can be advantageous as it reduces the loss of states entangled in different degrees of freedom while being transmitted

through the channel. These states are also useful in the easy implementation of quantum computing gates in different dimensions [189]. Here, we intend to prepare hybrid entangled states of polarization and OAM using SPDC photons. We study the higher dimensional hybrid entangled states (qubit-qudit) generated in SPDC and the effect of scattering on hybrid entangled state. We experimentally showed that the entanglement between polarization and OAM is remains preserved even after scattering.

7.2 Classical non-separable states

In general, quantum entanglement utilizes the entanglement between two particles of similar nature or similar degree of freedom (DoF). However, entanglement can be established between two different DoFs, where one DoF of the system cannot be measured without affecting the other. The non-separable nature of these states are explained in both classical as well as quantum domain. In classical domain, some classes of vector beams such as Poincare beams and vector vortex beams [190] show non-separable nature between the polarization and OAM of the beam [191]. Generally, a classical non-separable state in polarization and OAM degree of freedom is generated using a polarizing Sagnac interferometer [191]. Figure 7.1 shows the experimental scheme. In this case, a diagonally polarized Gaussian beam is fed into the Sagnac interferometer where a PBS splits the horizontal and vertical polarization in two directions, clockwise and counter-clockwise. Both the orthogonally polarized Gaussian beams counter propagate. A spiral phase plate (SPP) of order m converts the Gaussian beam to a vortex beam of order m and $-m$ for horizontal and vertical polarized light respectively. Both the beams combine at the same PBS to form the non-separable state,

$$|\Psi\rangle_{ns} = \frac{1}{\sqrt{2}} (|H\rangle |m\rangle + |V\rangle |-m\rangle). \quad (7.1)$$

At the output of the Sagnac interferometer, a QWP, HWP, and PBS is used for the measurement of the non-separable state. Projection of particular polarization state gives the information about OAM state corresponding to that polarization. The main

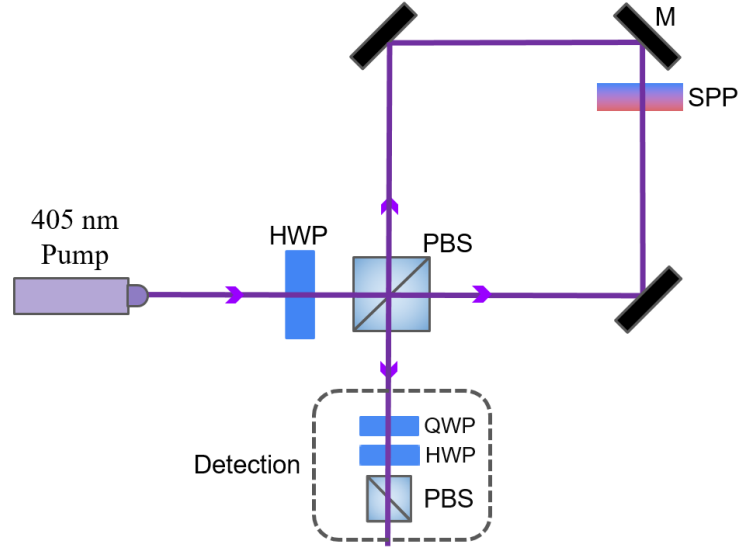


Figure 7.1: Sagnac interferometry based classical non-separable state

drawback of Sagnac interferometry based non-separable state is that it produces only one kind of entangled state mentioned in Eqn 7.1. To generate any arbitrary classical non-separable state, we propose an easier method. In this method, if the input beam is diagonally polarized Gaussian then by using SPP and SLM one can generate any arbitrary non-separable state. The experimental setup is shown in Figure 7.2. Since SLM does not change the spatial mode of vertical polarized light, it will not add any OAM value to it. Therefore in the final state, both horizontal and vertical polarized beams will have different OAM values. The final state can be written as,

$$|\Psi\rangle_{ns} = \frac{1}{\sqrt{2}} (|H\rangle |m_{SPP} + m_{SLM}\rangle + |V\rangle |m_{SPP}\rangle). \quad (7.2)$$

By changing the value m_{SLM} one can generate the non-separable state of any order. This method is easy to use as compared to Sagnac interferometry which requires a

perfect alignment.

7.2.1 Experimental setup and results

The experimental setup for the generation of classical non-separable state is shown in Figure 7.2. Toptica TopMode (405 nm) laser is used. The horizontal polarized light

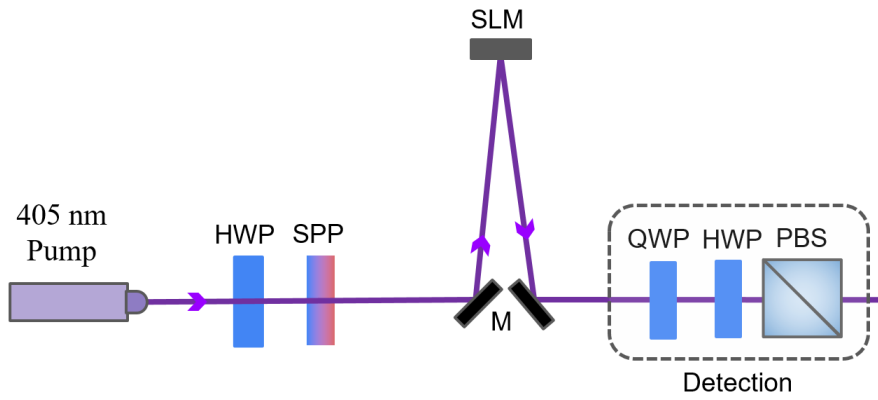


Figure 7.2: Experimental setup to generate classical non-separable state. SLM does not modulate the spatial mode of vertical polarized light. Therefore, At the output of SLM, H and V polarized light will have different OAM mode

with Gaussian mode ($|H\rangle|0\rangle$) is converted into the diagonal polarization ($|D\rangle|0\rangle$) after passing through the HWP which is kept at an angle 22.5° with respect to the fast axis. A SPP of order m is kept in the path of the light beam. After propagating through the SPP, the state of the light will become,

$$\begin{aligned} |\Psi\rangle &= |D\rangle|m_{\text{spp}}\rangle \\ &= |H\rangle|m_{\text{spp}}\rangle + |V\rangle|m_{\text{spp}}\rangle, \end{aligned} \quad (7.3)$$

The output of the SPP is then imaged onto the SLM. Since the liquid crystal molecules inside the SLM are aligned in a horizontal direction, it does not affect the vertically polarized light. The SLM will only change the spatial profile of horizontal polarized

light. The order of the LG mode can be easily controlled by the SLM through a computer. The final state of light beam after reflecting back from the SLM is written as,

$$|\Psi\rangle = |H\rangle |m_{\text{SPP}} + m_{\text{SLM}}\rangle + e^{i\phi} |V\rangle |m_{\text{SPP}}\rangle. \quad (7.4)$$

where ϕ is the relative phase delay between H and V polarized lights.

In this experiment, we used SPP of order $|m_{\text{SPP}}| = 2$. We generated various non-separable state by changing the order of LG mode m_{SLM} with the help of SLM. For the detection of the state, combination of QWP, HWP and PBS is used. The combination of HWP and PBS act as a polarizer. We measure the spatial distribution of light beam by projecting it to the different polarizations such as linear polarization (H , V , D , and A) and circular polarization (R and L). The intensity distribution for various non-separable states is given in the Figure 7.3. We also measured the Stokes parameters to

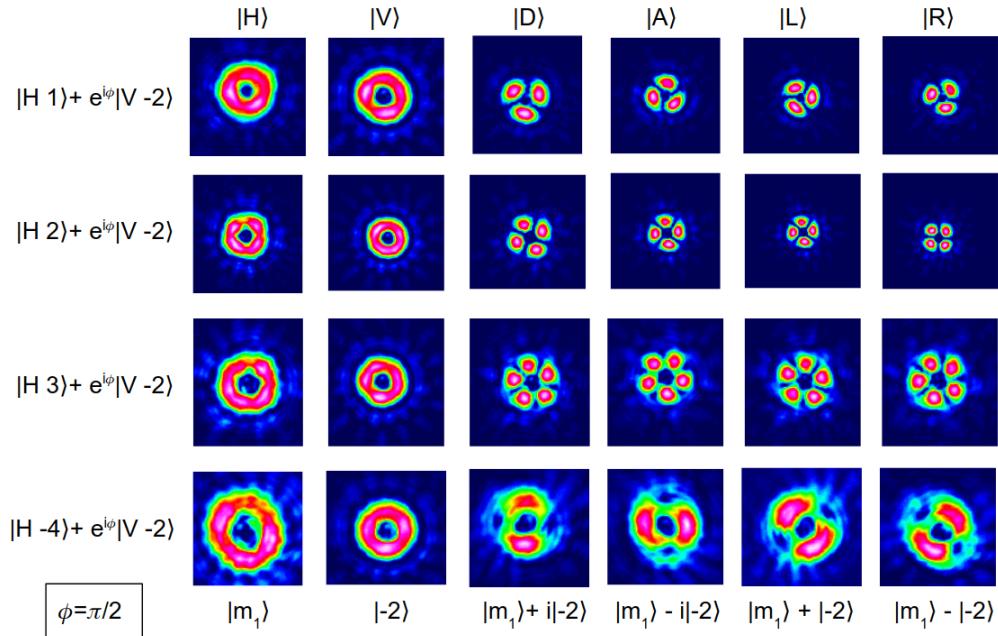


Figure 7.3: Experimentally generated classical non-separable state of different OAM. SPP of order $m = -2$ is used. m_1 is the order of OAM associated with horizontally polarized light. ϕ is the relative phase between H and V polarized light

calculate the degree of polarization. It is defined as,

$$\begin{aligned} S_0 &= I_H + I_V, & S_1 &= I_D - I_A \\ S_2 &= I_L - I_R, & S_3 &= I_H - I_V, \end{aligned} \quad (7.5)$$

where I_x is the intensity of x-polarized light beam. The degree of polarization (DOP) can be written in terms of Stokes parameter,

$$DOP = \sqrt{S_1^2 + S_2^2 + S_3^2}, \quad (7.6)$$

The *DOP* range from 0, corresponding to the completely mixed polarized state (unpolarized light), and 1 for completely polarized state. To characterize the non-separability of the state, linear entropy (S_L) can also be calculated. It can be represented in terms of *DOP* [191],

$$S_L = 1 - DOP^2. \quad (7.7)$$

The linear entropy measures the amount of mixedness present in the state. For a maximally entangled/non-separable system, the individual subsystem will always be in a mixed state. The maximum amount of mixedness present in subsystem leads to the maximum non-separability of the system. Thus, one can measure the degree of non-separability by measuring the linear entropy S_L of the subsystem. The linear entropy S_L can range from 0, corresponding to the product state, and 1, corresponding to the maximally non-separable state.

	<i>DOP</i>	Linear entropy S_L
Separable state	0.94	0.12
Non-separable state	0.05	0.99

Table 7.1: Experimentally recorded parameters, *DOP* and S_L for classical separable state and non-separable state.

The values of DOP and S_L are given in Table 7.1 for separable and non-separable states. Without SPP and $m_{SLM} = 0$ (Eqn. 7.4), the light beam is just a superposition of two orthogonal polarizations with Gaussian mode which results in a completely polarized state (separable state). That is why, DOP is maximum (0.94) without SPP and the linear entropy is $S_L = 0.12$, which represents the product state of polarization and Gaussian mode. When we introduce the SPP and $m_{SLM} \neq 0$, the H and V polarized components of light will correspond to different LG modes. H polarized light is associated with LG mode of order $|m_{SPP} + m_{SLM}\rangle$ and V polarized is associated with LG mode of order $|m_{SPP}\rangle$ (Eqn. 7.4). In this case, the state is completely unpolarized (or mixed polarized). Therefore the DOP is minimum (0.05) and the linear entropy is maximum (0.99) which shows the non-separability of the state in polarization and LG mode. We also recorded the spatial distribution of beam by projecting it to the different polarization states (Figure 7.3). Due to the non-separability of the state, OAM state of the beam varies according to the projection of different polarization states.

7.3 Polarization entanglement using SPDC

In general, any Type-II crystal or two Type-I crystals stacked together with their optic axis orthogonal to each other can be used to generate the polarization entangled state. The polarization entangled source with two crystal stacking have limitations in terms of the requirement of additional compensation in signal and/or idler as well as the limitation of crystal thickness for more brightness. To overcome these drawbacks, new interferometric schemes involving single nonlinear crystal were introduced for the generation of polarization entangled photon pairs [160, 192] - Single Crystal Interferometric Source (SCIS). An experimental schematic of SCIS with Type-I Beta-Barium Borate (β -BBO) crystal is given in Figure 7.4. In this, the crystal is kept exactly at the center of the polarizing Sagnac interferometric loop. A HWP is introduced outside the

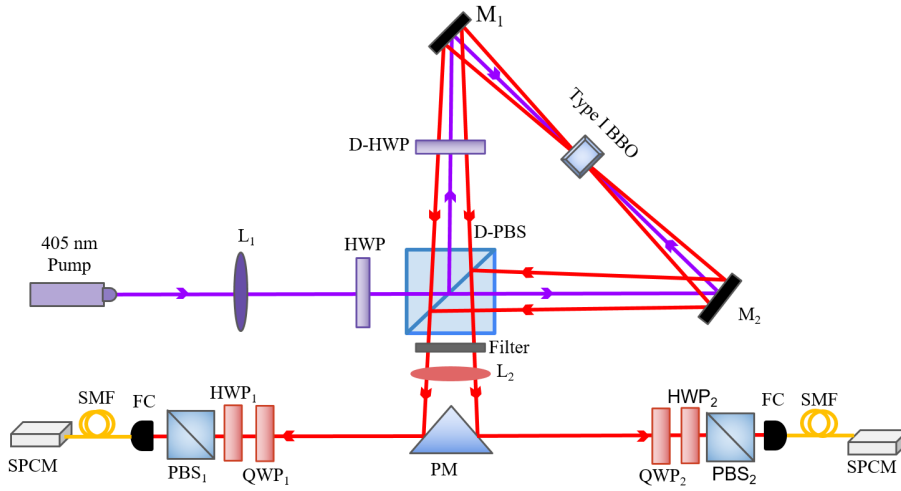


Figure 7.4: Experimental setup to produce polarization entangled state

interferometer in the pump beam path to adjust the amount of reflected and transmitted pump power. A horizontally polarized pump $|H\rangle_p$ will transmit through the D-PBS in clockwise direction and further pass through the crystal to produce vertically polarized down converted photon pairs ($|V\rangle_s$ and $|V\rangle_i$) in non-collinear fashion. They will pass through the D-HWP which is kept inside the interferometer and oriented at 45° with respect to the fast axis. D-HWP will convert them into horizontally polarized photons ($|H\rangle_s$ and $|H\rangle_i$). These photons will be transmitted through D-PBS and come out of the interferometer. On the other hand, a vertically polarized pump $|V\rangle_p$ will reflect through the D-PBS in counter-clockwise direction and become horizontally polarized $|H\rangle_p$ after passing through the same D-HWP. When the pump passes through the crystal the photon pairs (signal and idler) having orthogonal polarization to the pump ($|V\rangle_s$ and $|V\rangle_i$) will be generated from the other face of the crystal in non-collinear fashion. These photons will be reflected at the D-PBS and come out of the interferometer. These photons pair will combine at the D-PBS with the other pair coming from clockwise direction in the interferometer and the output state will be,

$$|\Psi\rangle_{out} = \frac{1}{\sqrt{2}} \left(|H\rangle_s |H\rangle_i + e^{i\phi} |V\rangle_s |V\rangle_i \right). \quad (7.8)$$

where ϕ is the relative phase between H and V polarized SPDC ring. The polarization state of the signal and idler photons will become indistinguishable which will lead to the polarization entanglement.

7.4 Orbital angular momentum distribution in SPDC

Any type of second order nonlinear SPDC crystal can be easily used to produce the OAM entanglement. The basic experimental setup of OAM entanglement is given in Figure 7.5. During the SPDC process OAM is conserved which means that the

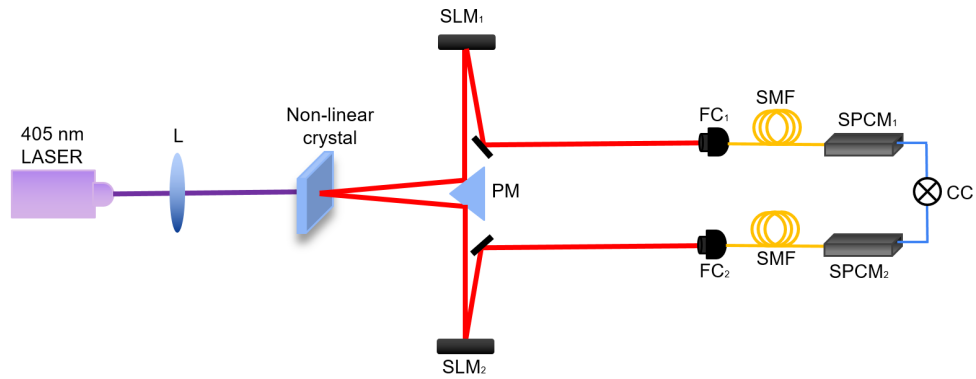


Figure 7.5: Basic experimental setup to observe orbital angular momentum distribution in SPDC

sum of OAM of signal and idler equals to the OAM of pump. This will lead to the indistinguishability of photons in OAM degree of freedom. As a result, the photon pair is entangled in OAM. The SPDC state in OAM degree of freedom can be written as,

$$|\Psi\rangle_{\text{spdc}} = \sum_{m=-\infty}^{+\infty} C_{m,m_p-m} |m\rangle_s |m_p - m\rangle_i. \quad (7.9)$$

where m_p , m_s , and $(m_p - m)_i$ are the OAM of pump, signal, and idler respectively, and C_{m,m_p-m} is the probability amplitude of detecting the state in $|m\rangle_s |m_p - m\rangle_i$. By post selecting the signal and idler state in particular OAM bases, one can detect the

entanglement in those bases [31].

7.5 Generation of hybrid entangled states

Consider a classical non-separable state in polarization and OAM as pump whose state can be written as,

$$|\Psi\rangle_{ns} = \frac{1}{\sqrt{2}} (|H\rangle |m_1\rangle + |V\rangle |m_2\rangle). \quad (7.10)$$

When the pump is input to the polarizing Sagnac interferometer (Figure 7.4), the horizontally polarized part associated with an OAM, m_1 , will be transmitted and the vertical part associated with an OAM, m_2 , will be reflected at the D-PBS. The generated SPDC photons from either sides of the crystal combine at the D-PBS to give the state,

$$|\Psi\rangle_{\text{Output}} = \sum_{m,m'=-\infty}^{+\infty} (C_{m,m_1-m} |H,m\rangle_s |H,m_1-m\rangle_i + C_{m',m_2-m'} |V,m'\rangle_s |V,m_2-m'\rangle_i), \quad (7.11)$$

where, $|H,m\rangle_s$ state represents horizontal polarized signal photons associated with OAM, m , and $|V,m'\rangle_s$ is vertically polarized idler photon having OAM, m' . Since SPCS process follows OAM conservation law, then m and m' can take any OAM value followed by the conservation law. So if we couple only Gaussian mode of one photon, say signal, using single mode fiber (SMF) then all the OAM value will transfer to the partner photon. Therefore, now the idler photon will have a particular OAM value with certainty which is equal to the OAM of pump photon. Therefore, by putting $m = m' = 0$, Eqn. 7.11 will become,

$$|\Psi\rangle_{\text{output}} = \frac{1}{\sqrt{2}} (|H,0\rangle_s |H,m_1\rangle_i + |V,0\rangle_s |V,m_2\rangle_i), \quad (7.12)$$

Since the idler photon is having non-zero OAM value, we have to couple it into a multi-mode fiber (MMF). Hence for the detection of hybrid entangled state, signal photon is

coupled into the SMF to measure the polarization state with Gaussian mode and idler photon is coupled into the MMF to measure the OAM state. Therefore, Eqn 7.12 can be further written as,

$$|\Psi\rangle_{\text{output}} = \frac{1}{\sqrt{2}} (|H\rangle_s |m_1\rangle_i + |V\rangle_s |m_2\rangle_i). \quad (7.13)$$

In this way, a classical non-separable state can be easily transferred into quantum hybrid entangled state.

7.5.1 Scattering of hybrid Entanglement

The hybrid entangled state between polarization and OAM allows the generation of qubit-qudit entangled state for quantum information processing [187]. The state is given by,

$$|\Psi\rangle_{\text{hybrid}} = \frac{1}{\sqrt{2}} (|H\rangle_s |m_1\rangle_i + |V\rangle_s |m_2\rangle_i), \quad (7.14)$$

where m_1 and m_2 are the OAM states of photon which can range from $-\infty$ to $+\infty$. Since the polarization state of photon is less affected by atmospheric turbulence, we use only OAM degree of freedom to propagate through turbulence. In this case, one of the photons which is used to measure the OAM state (here idler) propagates through the turbulence, while the other photon which is used to measure the polarization state (signal) is left unperturbed. Since we are performing experiment in lab, we used ground glass plate (GGP) to perturb the OAM state of idler. Ground glass plate is an optical diffuser which is used to scatter the light. There are various GGPs with different grits which provide the range from fine to coarse scattering. GGP with finer grit (e.g. 1500) allows higher transmission, whereas coarse grit (e.g. 120) allows lower transmission due to the high diffusion. After scattering through GGP, we collect the scattered pho-

tons with the help of plano-convex lens at the focus. The hybrid entangled state after scattering can be rewritten as:

$$|\Psi\rangle_{\text{scattered}} = \frac{1}{\sqrt{2}} \left(|H\rangle_s |m_1\rangle_{i_{\text{scattered}}} + |V\rangle_s |m_2\rangle_{i_{\text{scattered}}} \right). \quad (7.15)$$

Now we want to study the quality of entangled state after scattering and loss of correlated photon pairs due to scattering. To characterize both the states, with and without scattering, $|\Psi\rangle_{\text{scattered}}$ and $|\Psi\rangle_{\text{hybrid}}$, quantum state tomography should be performed. This will give a comparison between both the states.

7.5.2 Experimental setup and results

The experimental setup used to generate hybrid entangled state and to study the effect of scattering on it is given in Figure 7.6. Topica TopMode (405 nm) laser is used to

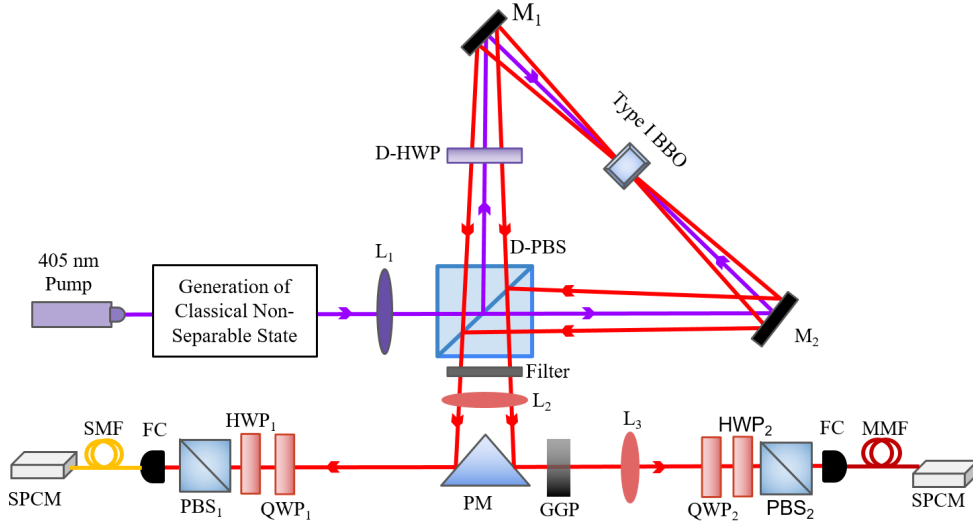


Figure 7.6: Experimental setup to generate quantum hybrid entangled state using Type-I BBO crystal. Multimode fiber (MMF) is used to detect OAM of the idler photons and single mode fiber is used to detect the polarization of signal photon with Gaussian mode. Ground glass plate (GGP) used for scattering.

generate the classical non-separable state $|\Psi\rangle_{ns} = \frac{1}{\sqrt{2}} \left(|H\rangle |2\rangle + e^{i\phi} |V\rangle |-2\rangle \right)$ using

SPP and SLM. Generation of state $|\Psi\rangle_{ns}$ is shown in Figure 7.2. To transform this state into hybrid entangled state we used polarizing Sagnac interferometry setup. In this, Type-I β -Barium Borate (BBO) crystal of thickness 2 mm with an optic axis oriented at 29.97° to the normal incidence is kept at the center line of the interferometry loop. The orientation of the crystal is kept in such a way that only horizontal polarized light will produce pair of photons after interacting with the crystal. A dual half wave plate (D-HWP) at an angle 45° with respect to the fast axis is kept in the reflected arm of the D-PBS. When we fed the classical non-separable state into Sagnac interferometry loop, the vertically polarized part will reflect through the D-PBS in counter-clockwise direction and become horizontal polarized after passing through the D-HWP kept inside the interferometer. This will generate vertically polarized photon pair $(|V\rangle_s |V\rangle_i)$ after passing through the Type-I BBO crystal. These photon pairs will be reflected at the D-PBS and come out from the interferometer. Again, horizontal polarized part of the non-separable state will transmit through the D-PBS in a clockwise direction and further pass through the crystal to produce a vertically polarized photon pairs. These photon pairs will pass through the D-HWP to convert into the horizontally polarized photons $(|H\rangle_s |H\rangle_i)$ so that they can easily transmit through the D-PBS.

Now, both the photon pairs coming from clockwise and counter-clockwise directions will combine at the D-PBS and exit from the same port of D-PBS. After coming out from the interferometer, both the photon pairs will become indistinguishable in polarization and OAM degrees of freedom and give rise to the desired entangled state. With the help of prism mirror (PM), signal and idler photon are further separated in two different directions to perform the measurement. The signal is coupled into SMF to measure the polarization state with Gaussian mode and idler is coupled into MMF to measure the OAM state.

To study the scattering effect on hybrid entangled state, only one of the photons is sent through the scattering media, while other is unperturbed. A ground glass plate (GGP) (grit 1500) is kept in the arm of idler photon. This will scatter the spatial mode of idler photon. The scattered photons are then collected by a two inch plano-convex lens to measure OAM state of photon at the focus.

State	Number of coincidence counts		
	H/V basis	D/A basis	L/R basis
$ H\rangle 2\rangle + V\rangle -2\rangle$			
Before Scattering	2487/20	2132/129	154/2091
After Scattering	115/4	100/10	7/104

Table 7.2: Recorded coincidence counts for entangled state with and without scattering. The integration time is 1 sec for before scattering and 3 sec for after scattering

We have recorded the data with and without scattering. For signal, we measure in H/V , D/A and L/R basis and for idler, we measure in two opposite OAM basis ($2\hbar$ and $-2\hbar$) and their superposition basis such as $D_{2,-2}/A_{2,-2}$ and $L_{2,-2}/R_{2,-2}$. For example, $D_{2,-2}$ represents the state $|\psi\rangle = 1/\sqrt{2}(|2\rangle + |-2\rangle)$ and $L_{2,-2}$ represents the state $|\psi\rangle = 1/\sqrt{2}(|2\rangle + i|-2\rangle)$. We observe that after the scattering, the number of photon pairs are reduced but the correlation between polarization and OAM DoF is remains preserved. The decay of correlated photon pair is shown in Table 7.2. We measured the coincidence counts without GGP with 1 sec integration time. The coincidence window is 2.43 ns. After scattering through GGP, the measured coincidence counts (CC) were very small (30 CC/sec) so we increased the integration time by 3 sec. Before scattering, the visibility for H/V , D/A , and L/R basis is recorded to be 98.26%, 87.90%, and 85.49% respectively. After scattering, the visibility for H/V , D/A , and L/R basis is recorded to be 92.81%, 83.69%, and 86.69% respectively, which is enough to violate the Bell's inequality. This shows that the hybrid entangled state is not affected by the scattering and entanglement is preserved. We further performed the quantum state tomography to compare both the results. The reconstructed density matrices for

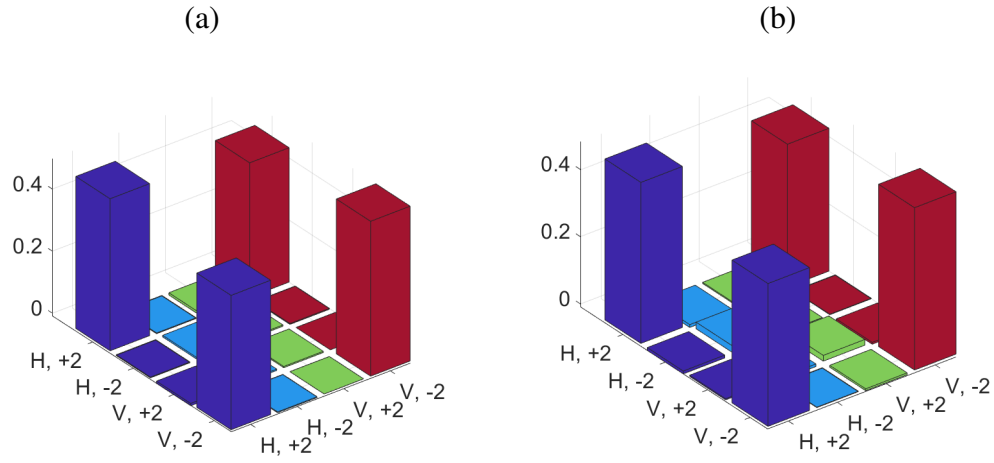


Figure 7.7: Density matrices of the measured hybrid entangled state (a) before scattering and (b) after scattering

both the cases are shown in Figure 7.7. To verify the presence of entanglement, we measured the Bell's inequality (S), state fidelity (F), and entanglement witness (W) for both the cases, before and after scattering. All these parameters are given in Table 7.3. The entanglement witness (W) is the sum of two visibilities in two different mutually unbiased bases (D/A and L/R),

$$W = \text{Vis}_{D/A} + \text{Vis}_{L/R} \begin{cases} \leq 1 & \text{Product state} \\ > 1 & \text{Entangled state} \end{cases} \quad (7.16)$$

The value of entanglement witness more than 1 verifies the presence of entanglement in the system. For maximally entangled state, the visibility must be 100% so that $W = 2$. In our experiment, the entanglement witness is 1.73 for hybrid state and 1.70

	Bell parameter S	Entanglement witness W	Fidelity F
Before Scattering	2.63 ± 0.02	1.73 ± 0.03	0.9286
After Scattering	2.49 ± 0.06	1.70 ± 0.08	0.9072

Table 7.3: Recorded parameters for with and without scattering.

for scattered hybrid state. The state fidelity is 0.9286 for hybrid state and 0.9072

for scattered state. Similarly, the value of Bell parameter for both the cases is also indicating that the quality of the hybrid entangled state is unaffected by any kind of turbulence.

7.6 Conclusion

In conclusion, we found a new method to generate classical non-separable state using polarization and OAM degrees of freedom. The new setup is simple as compared to Sagnac interferometry. We verified the presence of non-separable state by measuring the DOP and linear entropy. We further transformed this classical non-separable state into quantum hybrid entangled state. We kept GGP in the path of one photon from the entangled photon pair to study the scattering effect on the hybrid entangled state. We scatter the OAM state of photon and observe that the entanglement is still preserved under the scattering. The density matrices of entangled state with and without the scattering show the presence of entanglement. These results would play an important role in quantum key distribution protocol.

Chapter 8

Summary and future scope

Please note that Research is a never ending process!

-Prof. R.P. Singh, Thesis supervisor

8.1 Summary of the work done

This thesis deals with the study of entangled photons and their application in quantum information processing (QIP), especially in quantum key distribution (QKD) protocols. We first study the concept of indistinguishability of photons. The spatial and temporal indistinguishability leads to the quantum entanglement between two photons. We perform the experiments to study the qubit as well as qudit entanglement in d-dimension and their characterization using quantum state tomography (QST). We use spontaneous parametric down-conversion (SPDC) process to generate the bi-photon entangled state. To prove that the generated state is bi-photon, we performed the Hong-Ou-Mandel (HOM) interference. In collinear SPDC process, where both the photons propagate along z-direction, it is difficult to observe the entanglement in polarization as well as in orbital angular momentum without losing a single photon pair.

Therefore, we use the concept of entanglement duality to observe the entanglement in both degrees of freedom without any loss. Then we use the polarization entangled photons to implement the BBM92 protocol over atmospheric channels of 35 meters and 200 meters. In this study, we experimentally show that the key rate depends on extinction coefficient of atmospheric aerosols and channel length. The transmission of qubit could be through free space or optical fiber. Since the polarization qubit suffers decoherence when transmit through fibers, that is why we choose free space channel so that polarization could be transmitted faithfully through atmosphere due to its non-birefringent nature. However, OAM carrying photons with their spatial modes could be affected by atmospheric turbulence. Therefore to further study the effect of turbulence on entangled state, we choose hybrid entangled photons, where polarization and OAM of photons are entangled with each other. The hybrid entangled state can be used to enhance the security against eavesdropper in QKD protocol. We first generated the hybrid entangled state and then we put a ground glass plate (GGP) in one of the photons path to scatter the spatial profile of photons. We compare both the results, before and after scattering, and we observe that the entanglement is preserved after scattering through the GGP.

In chapter 1, we have covered the basic concepts about qubit, quantum entanglement and their applications, state tomography, etc., along with the brief outline of each chapter. In chapter 2, we use the SPDC process to generate non-collinear twin photons and study the indistinguishability of twin photons. We setup the Hong-Ou-Mandel experiment to quantify the indistinguishability. We coupled only Gaussian mode of twin photon to ensure the spatial indistinguishability. The visibility of the bi-photon interference with respect to temporal delay is observed to be 98.3% and the FWHM of the dip is measured as $146 \mu\text{m}$ and $68 \mu\text{m}$ for 3 nm and 10 nm bandpass filters respectively. We also study the effect of polarization distinguishability at the dip of

bi-photon interference. The visibility of the interference is maximum when both the photons have same polarization. The visibility of the dip becomes zero when both the photons are orthogonal to each other. Then we use co-linear case of SPDC to observe the entanglement in polarization and orbital angular momentum (OAM). Here we introduced the entanglement sorting scheme to observe the entanglement in one degree of freedom while sorting them in another degree of freedom. The distinguishability in one variable does not affect the entanglement in other variable. We first observe the OAM entanglement by sorting the photon in polarization. The average visibility of OAM entanglement in E/O and D_{EO}/A_{EO} basis is 86.8% and the Bell parameter S is estimated to be 2.46 ± 0.08 . Similarly, we observed the polarization entanglement by sorting the photons in even/odd OAM basis. For even/odd OAM sorter we use the double Mach-Zehnder interferometry. In this case all the even order OAM and odd order OAM will exit from two different output ports of 50:50 BS. At the output port of BS, the photons are entangled in polarization. The observed average visibility in H/V and D/A basis is 74.55 % and the estimated Bell parameter is $S = 2.11 \pm 0.03$.

In chapter 3, we generated all the four Bell states using HWPs only. We accomplished the Pauli X, Y, and Z gate operations using HWPs in order to transform the Bell states from one to another. We also performed the quantum state tomography for each Bell state. The measured fidelity of each state is more than 96%. In chapter 4, we reformulated the Bell-CHSH inequality in order to reduce the total number of measurement settings. The reformulated Bell-CHSH parameter can also be used to guess the Bell states. We have verified the scheme through experiment performed in laboratory as well as on the IBM quantum platform.

In chapter 5, we implemented the BBM92 QKD protocol using polarization entangled state outside the laboratory over 35 meters and 200 meters free space atmosph-

pheric channel. The transmissivity of the channel for 35m and 200m is 0.94 and 0.71 respectively. The brightness of the entangled photon source is measured to be $0.3 \text{ KHz mW}^{-1}\text{nm}^{-1}$ and the fidelity was 92.76%. The key rate was inversely proportional to the channel length and extinction coefficient of the atmospheric aerosols. The observed secure key rate for 35m and 200m is 2.33 kbps and 1.71 kbps respectively.

In chapter 6, we study the OAM spectrum of entangled photons in detail. The photon pairs generated in SPDC process in principle have infinite dimensional entanglement in OAM degree of freedom. By tailoring the OAM spectrum of photon pairs one can engineer the higher dimension entanglement according to their choice. In this chapter, we shown that the pump size and crystal length are the two main parameters that affect the width of OAM spectrum. Additionally, coupling efficiency can also manipulate the OAM spectrum with change in the size of signal/idler at the fiber position. We generated the qutrit entangled state and verified using the visibility plot.

In chapter 7, we introduced novel method to generate the classical non-separable state in polarization and OAM degree of freedom which can be easily transformed into quantum hybrid entangled state using SPDC process. In this chapter, we study the effect of scattering on hybrid entanglement. We scatter those photons which are used to measure the OAM state while other photon is left undisturbed. We perform the quantum state tomography of the entangled state with and without scattering and observe that the entanglement is remains preserved under the scattering. The fidelity of entangled state before and after scattering is recorded to be 92% and 90% which shows the presence of entanglement.

8.2 Scope for future work

Increasing the security against eavesdropper and information capacity per photon in entanglement-based QKD protocol has been a hot topic of modern research. In chapter 5, we have already explored the BBM92 protocol using two dimensional entangled state *i.e.* polarization entanglement. Since the higher dimension entangled state have more advantage over two dimension entangled state in terms of increasing the key rate and security against any third party, OAM degree of freedom can be a good candidate due to their easy scalability in dimension. In chapter 6, we have already explored the OAM entangled state up to dimension three. Now we would like to extend the work for the generation of qudit entangled state of more than three dimensions. In chapter 7, we have studied the scattering of hybrid entangled state. Since it involves two degrees of freedom, it will surely boost the security in QKD protocol. We have shown that the hybrid entanglement is preserved under scattering. Thus, it can also be useful against atmospheric turbulence for free space communication. We would like to perform the QKD protocol using hybrid entanglement. Also, the recently started satellite based quantum communication projects in the country are gaining more attention. I would like to extend my research work in this field.

List of Publications

Thesis related Publications

Published

1. **Sarika Mishra**, Ayan Biswas, Satyajeet Patil, Pooja Chandravanshi, Vardaan Mongia, Tanya Sharma, Anju Rani, Shashi Prabhakar, S Ramachandran, and Ravindra Pratap Singh, “BBM92 quantum key distribution over a free space dusty channel of 200 meters”, *Journal of Optics* **24**, 074002 (2022).

DOI: <https://doi.org/10.1088/2040-8986/ac6f0b>

2. Nijil Lal, **Sarika Mishra**, and R.P. Singh, “Indistinguishable photons”, *AVS Quantum Science* **4**, 021701 (2022).

DOI: <https://doi.org/10.1116/5.0083968>

Under Review

3. Nijil Lal, **Sarika Mishra**, Anju Rani, Anindya Banerji, C. Perumangattu, and R.P. Singh, “Polarization-orbital angular momentum duality assisted entanglement observation for indistinguishable photons”, arXiv preprint arXiv:2104.11784 (2022).

4. Anindya Banerji, **Sarika Mishra**, Ayan Biswas, Nijil Lal, Shashi Prabhakar, and R.P. Singh, “Optimised entanglement detection for quantum information protocols” Quantum Information Processing (QINP) (2022)
5. **Sarika Mishra** and R.P. Singh, “Generation and transformation of polarization-entangled Bell states using linear optics” (2022)

Under preparation

6. **Sarika Mishra** and R.P. Singh, “Scattering of hybrid entangled state”
7. **Sarika Mishra**, Aviv Karnieli, Joshua F.C., Eyal Rozenberg, Ofir Yesharim, Shashi Prabhakar, Ady Arie, and R.P. Singh, “On demand higher dimension entanglement”

Other Publications

8. Ayan Biswas, **Sarika Mishra**, Satyajeet Patil, Anindya Banerji and R. P. Singh, “Use of Non Maximal entangled state for free space BBM92 quantum key distribution protocol” (2022)

Bibliography

- [1] G. N. Lewis, *The conservation of photons*, Nature **118**, 874–875 (1926).
- [2] A. Einstein, *Über einen die erzeugung und verwandlung des lichtet betreffenden heuristischen gesichtspunkt*, Annalen der Physik **322**, 132–148 (1905).
- [3] M. Planck, *On the theory of the energy distribution law of the normal spectrum*, Verh. Deut. Phys. Ges **2**, 237–245 (1900).
- [4] A. H. Compton, *A quantum theory of the scattering of x-rays by light elements*, Physical review **21**, 483 (1923).
- [5] R. Brown and R. Q. Twiss, *Correlation between photons in two coherent beams of light*, Nature **177**, 27–29 (1956).
- [6] R. H. Brown and R. Q. Twiss, *2. a test of a new type of stellar interferometer on sirius*, in “A Source Book in Astronomy and Astrophysics, 1900–1975,” (Harvard University Press, 2013), pp. 8–12.
- [7] H. J. Kimble, M. Dagenais, and L. Mandel, *Photon antibunching in resonance fluorescence*, Physical Review Letters **39**, 691 (1977).
- [8] A. Einstein, B. Podolsky, and N. Rosen, *Can quantum-mechanical description of physical reality be considered complete?* Physical review **47**, 777 (1935).

- [9] J. S. Bell, *On the einstein podolsky rosen paradox*, Physics Physique Fizika **1**, 195 (1964).
- [10] J. F. Clauser, M. A. Horne, A. Shimony, and R. A. Holt, *Proposed experiment to test local hidden-variable theories*, Physical review letters **23**, 880 (1969).
- [11] A. Aspect, P. Grangier, and G. Roger, *Experimental realization of einstein-podolsky-rosen-bohm gedankenexperiment: a new violation of bell's inequalities*, Physical review letters **49**, 91 (1982).
- [12] C.-K. Hong, Z.-Y. Ou, and L. Mandel, *Measurement of subpicosecond time intervals between two photons by interference*, Phys. Rev. Lett. **59**, 2044 (1987).
- [13] Z. Ou and L. Mandel, *Violation of bell's inequality and classical probability in a two-photon correlation experiment*, Physical review letters **61**, 50 (1988).
- [14] P. Kok, W. J. Munro, K. Nemoto, T. C. Ralph, J. P. Dowling, and G. J. Milburn, *Linear optical quantum computing with photonic qubits*, Reviews of modern physics **79**, 135 (2007).
- [15] F. Flamini, N. Spagnolo, and F. Sciarrino, *Photonic quantum information processing: a review*, Rep. Prog. Phys. **82**, 016001 (2018).
- [16] N. Sangouard and H. Zbinden, *What are single photons good for?* Journal of Modern Optics **59**, 1458–1464 (2012).
- [17] T. Northup and R. Blatt, *Quantum information transfer using photons*, Nature photonics **8**, 356–363 (2014).
- [18] A. M. Fox, M. Fox *et al.*, *Quantum optics: an introduction*, vol. 15 (Oxford university press, 2006).

- [19] J. B. Altepeter, E. R. Jeffrey, and P. G. Kwiat, *Photonic state tomography*, *Advances in Atomic, Molecular, and Optical Physics* **52**, 105–159 (2005).
- [20] G. S. Agarwal, *Quantum optics* (Cambridge University Press, 2012).
- [21] A. Aspect, J. Dalibard, and G. Roger, *Experimental test of bell's inequalities using time-varying analyzers*, *Phys. Rev. Lett.* **49**, 1804–1807 (1982).
- [22] D. Bouwmeester, J.-W. Pan, K. Mattle, M. Eibl, H. Weinfurter, and A. Zeilinger, *Experimental quantum teleportation*, *Nature* **390**, 575–579 (1997).
- [23] R. Horodecki, P. Horodecki, M. Horodecki, and K. Horodecki, *Quantum entanglement*, *Reviews of modern physics* **81**, 865 (2009).
- [24] L. K. Shalm, D. R. Hamel, Z. Yan, C. Simon, K. J. Resch, and T. Jennewein, *Three-photon energy–time entanglement*, *Nature Physics* **9**, 19–22 (2013).
- [25] M. Bourennane, M. Eibl, C. Kurtsiefer, S. Gaertner, H. Weinfurter, O. Gühne, P. Hyllus, D. Bruß, M. Lewenstein, and A. Sanpera, *Experimental detection of multipartite entanglement using witness operators*, *Physical review letters* **92**, 087902 (2004).
- [26] D. M. Greenberger, M. A. Horne, and A. Zeilinger, *Going beyond bell's theorem*, in “Bell's theorem, quantum theory and conceptions of the universe,” (Springer, 1989), pp. 69–72.
- [27] J.-W. Pan, D. Bouwmeester, M. Daniell, H. Weinfurter, and A. Zeilinger, *Experimental test of quantum nonlocality in three-photon greenberger–horne–zeilinger entanglement*, *Nature* **403**, 515–519 (2000).
- [28] J. C. Howell, R. S. Bennink, S. J. Bentley, and R. W. Boyd, *Realization of the einstein-podolsky-rosen paradox using momentum-and position-entangled pho-*

- tons from spontaneous parametric down conversion*, Physical Review Letters **92**, 210403 (2004).
- [29] P. G. Kwiat, A. M. Steinberg, and R. Y. Chiao, *High-visibility interference in a bell-inequality experiment for energy and time*, Physical Review A **47**, R2472 (1993).
- [30] S. Franke-Arnold, S. M. Barnett, E. Yao, J. Leach, J. Courtial, and M. Padgett, *Uncertainty principle for angular position and angular momentum*, New Journal of Physics **6**, 103 (2004).
- [31] A. Mair, A. Vaziri, G. Weihs, and A. Zeilinger, *Entanglement of the orbital angular momentum states of photons*, Nature **412**, 313–316 (2001).
- [32] M. Holland and K. Burnett, *Interferometric detection of optical phase shifts at the heisenberg limit*, Physical review letters **71**, 1355 (1993).
- [33] I. Marcikic, H. de Riedmatten, W. Tittel, V. Scarani, H. Zbinden, and N. Gisin, *Time-bin entangled qubits for quantum communication created by femtosecond pulses*, Physical Review A **66**, 062308 (2002).
- [34] P. G. Kwiat, K. Mattle, H. Weinfurter, A. Zeilinger, A. V. Sergienko, and Y. Shih, *New high-intensity source of polarization-entangled photon pairs*, Physical Review Letters **75**, 4337 (1995).
- [35] N. K. Langford, R. B. Dalton, M. D. Harvey, J. L. O’Brien, G. J. Pryde, A. Gilchrist, S. D. Bartlett, and A. G. White, *Measuring entangled qutrits and their use for quantum bit commitment*, Physical review letters **93**, 053601 (2004).

- [36] A. Vaziri, G. Weihs, and A. Zeilinger, *Experimental two-photon, three-dimensional entanglement for quantum communication*, Physical Review Letters **89**, 240401 (2002).
- [37] A. C. Dada, J. Leach, G. S. Buller, M. J. Padgett, and E. Andersson, *Experimental high-dimensional two-photon entanglement and violations of generalized bell inequalities*, Nature Physics **7**, 677–680 (2011).
- [38] P. G. Kwiat, *Hyper-entangled states*, Journal of modern optics **44**, 2173–2184 (1997).
- [39] S. P. Walborn, *Breaking the communication barrier*, Nature Physics **4**, 268–269 (2008).
- [40] J. T. Barreiro, N. K. Langford, N. A. Peters, and P. G. Kwiat, *Generation of hyperentangled photon pairs*, Physical review letters **95**, 260501 (2005).
- [41] L. Neves, G. Lima, A. Delgado, and C. Saavedra, *Hybrid photonic entanglement: Realization, characterization, and applications*, Physical Review A **80**, 042322 (2009).
- [42] H. Jeong, A. Zavatta, M. Kang, S.-W. Lee, L. S. Costanzo, S. Grandi, T. C. Ralph, and M. Bellini, *Generation of hybrid entanglement of light*, Nature Photonics **8**, 564–569 (2014).
- [43] E. Nagali and F. Sciarrino, *Generation of hybrid polarization-orbital angular momentum entangled states*, Optics express **18**, 18243–18248 (2010).
- [44] D. Collins, N. Gisin, N. Linden, S. Massar, and S. Popescu, *Bell inequalities for arbitrarily high-dimensional systems*, Physical review letters **88**, 040404 (2002).

- [45] D. C. Burnham and D. L. Weinberg, *Observation of simultaneity in parametric production of optical photon pairs*, Physical Review Letters **25**, 84 (1970).
- [46] C. Hong and L. Mandel, *Experimental realization of a localized one-photon state*, Physical Review Letters **56**, 58 (1986).
- [47] C. Gerry, P. Knight, and P. L. Knight, *Introductory quantum optics* (Cambridge university press, 2005).
- [48] R. W. Boyd, *Nonlinear optics* (Academic press, 2020).
- [49] V. G. Dmitriev, G. G. Gurzadyan, and D. N. Nikogosyan, *Handbook of nonlinear optical crystals*, vol. 64 (Springer, 2013).
- [50] S. Karan, S. Aarav, H. Bharadhwaj, L. Taneja, A. De, G. Kulkarni, N. Meher, and A. K. Jha, *Phase matching in β -barium borate crystals for spontaneous parametric down-conversion*, Journal of Optics **22**, 083501 (2020).
- [51] F. Steinlechner, M. Gilaberte, M. Jofre, T. Scheidl, J. P. Torres, V. Pruneri, and R. Ursin, *Efficient heralding of polarization-entangled photons from type-0 and type-ii spontaneous parametric downconversion in periodically poled ktiopo 4*, JOSA B **31**, 2068–2076 (2014).
- [52] P. G. Kwiat, E. Waks, A. G. White, I. Appelbaum, and P. H. Eberhard, *Ultra-bright source of polarization-entangled photons*, Physical Review A **60**, R773 (1999).
- [53] M. Jabir, N. Apurv Chaitanya, M. Mathew, and G. Samanta, *Direct transfer of classical non-separable states into hybrid entangled two photon states*, Scientific Reports **7**, 1–7 (2017).

- [54] D. F. James, P. G. Kwiat, W. J. Munro, and A. G. White, *On the measurement of qubits*, in “Asymptotic Theory of Quantum Statistical Inference: Selected Papers,” (World Scientific, 2005), pp. 509–538.
- [55] R. T. Thew, K. Nemoto, A. G. White, and W. J. Munro, *Qudit quantum-state tomography*, *Physical Review A* **66**, 012303 (2002).
- [56] E. Toninelli, B. Ndagano, A. Vallés, B. Sephton, I. Nape, A. Ambrosio, F. Capasso, M. J. Padgett, and A. Forbes, *Concepts in quantum state tomography and classical implementation with intense light: a tutorial*, *Advances in Optics and Photonics* **11**, 67–134 (2019).
- [57] P. Zoller, T. Beth, D. Binosi, R. Blatt, H. Briegel, D. Bruss, T. Calarco, J. I. Cirac, D. Deutsch, J. Eisert *et al.*, *Quantum information processing and communication*, *The European Physical Journal D-Atomic, Molecular, Optical and Plasma Physics* **36**, 203–228 (2005).
- [58] P. Kok and B. W. Lovett, *Introduction to optical quantum information processing* (Cambridge university press, 2010).
- [59] C. Monroe, *Quantum information processing with atoms and photons*, *Nature* **416**, 238–246 (2002).
- [60] C. H. Bennett, G. Brassard, C. Crépeau, R. Jozsa, A. Peres, and W. K. Wootters, *Teleporting an unknown quantum state via dual classical and einstein-podolsky-rosen channels*, *Physical review letters* **70**, 1895 (1993).
- [61] B. Yurke and D. Stoler, *Einstein-podolsky-rosen effects from independent particle sources*, *Physical review letters* **68**, 1251 (1992).

- [62] M. Zukowski, A. Zeilinger, M. A. Horne, and A. K. Ekert, " *event-ready-detectors*" *bell experiment via entanglement swapping*. Physical Review Letters **71** (1993).
- [63] S. Bose, V. Vedral, and P. L. Knight, *Multiparticle generalization of entanglement swapping*, Physical Review A **57**, 822 (1998).
- [64] J.-W. Pan, D. Bouwmeester, H. Weinfurter, and A. Zeilinger, *Experimental entanglement swapping: entangling photons that never interacted*, Physical review letters **80**, 3891 (1998).
- [65] K. Mattle, H. Weinfurter, P. G. Kwiat, and A. Zeilinger, *Dense coding in experimental quantum communication*, Physical Review Letters **76**, 4656 (1996).
- [66] P. G. Kwiat, K. Mattle, H. Weinfurter, and A. Zeilinger, *Polarization-entangled photons and quantum dense coding*, Optics and Photonics News **7**, 14–15 (1996).
- [67] A. K. Ekert, *Quantum cryptography and bell's theorem*, in "Quantum Measurements in Optics," (Springer, 1992), pp. 413–418.
- [68] C. H. Bennett, G. Brassard, and N. D. Mermin, *Quantum cryptography without bell's theorem*, Physical review letters **68**, 557 (1992).
- [69] T. Jennewein, C. Simon, G. Weihs, H. Weinfurter, and A. Zeilinger, *Quantum cryptography with entangled photons*, Physical review letters **84**, 4729 (2000).
- [70] A. K. Ekert, *Quantum cryptography based on Bell's theorem*, Physical Review Letters **67**, 661 (1991).

- [71] J. W. Gibbs, *Elementary principles in statistical mechanics: developed with especial reference to the rational foundation of thermodynamics* (Yale University Press, 1914).
- [72] S. Saunders, *The concept ‘indistinguishable’*, *Stud. Hist. Philos. Sci. B: Stud. Hist. Philos. M. P.* **71**, 37–59 (2020).
- [73] C. Santori, D. Fattal, J. Vučković, G. S. Solomon, and Y. Yamamoto, *Indistinguishable photons from a single-photon device*, *Nature* **419**, 594–597 (2002).
- [74] K. Sun, Y. Wang, Z.-H. Liu, X.-Y. Xu, J.-S. Xu, C.-F. Li, G.-C. Guo, A. Castellini, F. Nosrati, G. Compagno, and R. L. Franco, *Experimental quantum entanglement and teleportation by tuning remote spatial indistinguishability of independent photons*, *Opt. Lett.* **45**, 6410–6413 (2020).
- [75] B. Kambs and C. Becher, *Limitations on the indistinguishability of photons from remote solid state sources*, *New J. Phys.* **20**, 115003 (2018).
- [76] Y.-M. He, Y. He, Y.-J. Wei, D. Wu, M. Atatüre, C. Schneider, S. Höfling, M. Kamp, C.-Y. Lu, and J.-W. Pan, *On-demand semiconductor single-photon source with near-unity indistinguishability*, *Nat. Nanotechnol.* **8**, 213–217 (2013).
- [77] O. Gazzano, S. M. De Vasconcellos, C. Arnold, A. Nowak, E. Galopin, I. Sagnes, L. Lanco, A. Lemaître, and P. Senellart, *Bright solid-state sources of indistinguishable single photons*, *Nat. Commun.* **4**, 1–6 (2013).
- [78] H. Wang, Y.-M. He, T.-H. Chung, H. Hu, Y. Yu, S. Chen, X. Ding, M.-C. Chen, J. Qin, X. Yang *et al.*, *Towards optimal single-photon sources from polarized microcavities*, *Nat. Photonics* **13**, 770–775 (2019).

- [79] D. Branning, W. Grice, R. Erdmann, and I. Walmsley, *Engineering the indistinguishability and entanglement of two photons*, Phys. Rev. Lett. **83**, 955 (1999).
- [80] M. Müller, S. Bounouar, K. D. Jöns, M. Glässl, and P. Michler, *On-demand generation of indistinguishable polarization-entangled photon pairs*, Nat. Photonics **8**, 224–228 (2014).
- [81] D. Huber, M. Reindl, Y. Huo, H. Huang, J. S. Wildmann, O. G. Schmidt, A. Rastelli, and R. Trotta, *Highly indistinguishable and strongly entangled photons from symmetric GaAs quantum dots*, Nat. Commun. **8**, 1–7 (2017).
- [82] J. Liu, R. Su, Y. Wei, B. Yao, S. F. C. da Silva, Y. Yu, J. Iles-Smith, K. Srinivasan, A. Rastelli, J. Li *et al.*, *A solid-state source of strongly entangled photon pairs with high brightness and indistinguishability*, Nat. Nanotechnol. **14**, 586–593 (2019).
- [83] H. Wang, H. Hu, T.-H. Chung, J. Qin, X. Yang, J.-P. Li, R.-Z. Liu, H.-S. Zhong, Y.-M. He, X. Ding *et al.*, *On-demand semiconductor source of entangled photons which simultaneously has high fidelity, efficiency, and indistinguishability*, Phys. Rev. Lett. **122**, 113602 (2019).
- [84] L. Mandel, *Coherence and indistinguishability*, Opt. Lett. **16**, 1882–1883 (1991).
- [85] D. M. Greenberger and A. Yasin, *Simultaneous wave and particle knowledge in a neutron interferometer*, Phys. Lett. A **128**, 391–394 (1988).
- [86] T. B. Pittman, D. V. Strekalov, A. Migdall, M. H. Rubin, A. V. Sergienko, and Y. H. Shih, *Can two-photon interference be considered the interference of two photons?* Phys. Rev. Lett. **77**, 1917–1920 (1996).

- [87] T. J. Herzog, P. G. Kwiat, H. Weinfurter, and A. Zeilinger, *Complementarity and the quantum eraser*, Phys. Rev. Lett. **75**, 3034–3037 (1995).
- [88] M. N. Bera, T. Qureshi, M. A. Siddiqui, and A. K. Pati, *Duality of quantum coherence and path distinguishability*, Phys. Rev. A **92**, 012118 (2015).
- [89] M. C. Tichy, *Interference of identical particles from entanglement to boson-sampling*, J. Phys. B: At. Mol. Opt. **47**, 103001 (2014).
- [90] B. Liu, F. Sun, Y. Gong, Y. Huang, Z. Ou, and G. Guo, *Investigation of the role of indistinguishability in photon bunching and stimulated emission*, Phys. Rev. A **79**, 053846 (2009).
- [91] V. Shchesnovich, *Universality of generalized bunching and efficient assessment of boson sampling*, Phys. Rev. Lett. **116**, 123601 (2016).
- [92] H. A. Shenoy, R. Srikanth, and T. Srinivas, *Efficient quantum random number generation using quantum indistinguishability*, Fluct. Noise Lett. **12**, 1350020 (2013).
- [93] R. Lo Franco and G. Compagno, *Indistinguishability of elementary systems as a resource for quantum information processing*, Phys. Rev. Lett. **120**, 240403 (2018).
- [94] F. Nosrati, A. Castellini, G. Compagno, and R. L. Franco, *Robust entanglement preparation against noise by controlling spatial indistinguishability*, Npj Quantum Inf. **6**, 1–7 (2020).
- [95] S. Bose and D. Home, *Duality in entanglement enabling a test of quantum indistinguishability unaffected by interactions*, Phys. Rev. Lett. **110**, 140404 (2013).

- [96] A. Peres, *Quantum theory: concepts and methods*, vol. 57 (Springer Science & Business Media, 2006).
- [97] A. M. L. Messiah and O. W. Greenberg, *Symmetrization postulate and its experimental foundation*, Phys. Rev. **136**, B248–B267 (1964).
- [98] J. J. Sakurai and E. D. Commins, *Modern quantum mechanics, revised edition*, (1995).
- [99] N. Koguchi, K. Ishige, and S. Takahashi, *New selective molecular-beam epitaxial growth method for direct formation of gaas quantum dots*, Journal of Vacuum Science & Technology B: Microelectronics and Nanometer Structures Processing, Measurement, and Phenomena **11**, 787–790 (1993).
- [100] S. Bietti, J. Bocquel, S. Adorno, T. Mano, J. G. Keizer, P. M. Koenraad, and S. Sanguinetti, *Precise shape engineering of epitaxial quantum dots by growth kinetics*, Physical Review B **92**, 075425 (2015).
- [101] P. Senellart, G. Solomon, and A. White, *High-performance semiconductor quantum-dot single-photon sources*, Nature nanotechnology **12**, 1026–1039 (2017).
- [102] S. Kiravittaya, A. Rastelli, and O. G. Schmidt, *Advanced quantum dot configurations*, Reports on Progress in Physics **72**, 046502 (2009).
- [103] O. Gazzano and G. S. Solomon, *Toward optical quantum information processing with quantum dots coupled to microstructures*, J. Opt. Soc. Am. B **33**, C160–C175 (2016).
- [104] P. Kaer, N. Gregersen, and J. Mork, *The role of phonon scattering in the indistinguishability of photons emitted from semiconductor cavity qed systems*, New J. Phys. **15**, 035027 (2013).

- [105] S. Ates, S. Ulrich, S. Reitzenstein, A. Löffler, A. Forchel, and P. Michler, *Post-selected indistinguishable photons from the resonance fluorescence of a single quantum dot in a microcavity*, Phys. Rev. Lett. **103**, 167402 (2009).
- [106] Y.-J. Wei, Y.-M. He, M.-C. Chen, Y.-N. Hu, Y. He, D. Wu, C. Schneider, M. Kamp, S. Höfling, C.-Y. Lu *et al.*, *Deterministic and robust generation of single photons from a single quantum dot with 99.5% indistinguishability using adiabatic rapid passage*, Nano Lett. **14**, 6515–6519 (2014).
- [107] Ł. Dusanowski, S.-H. Kwon, C. Schneider, and S. Höfling, *Near-unity indistinguishability single photon source for large-scale integrated quantum optics*, Phys. Rev. Lett. **122**, 173602 (2019).
- [108] R. Stevenson, C. Salter, J. Nilsson, A. Bennett, M. Ward, I. Farrer, D. Ritchie, and A. Shields, *Indistinguishable entangled photons generated by a light-emitting diode*, Phys. Rev. Lett. **108**, 040503 (2012).
- [109] A. Bennett, R. Patel, A. Shields, K. Cooper, P. Atkinson, C. Nicoll, and D. Ritchie, *Indistinguishable photons from a diode*, Appl. Phys. Lett. **92**, 193503 (2008).
- [110] R. C. Schofield, C. Clear, R. A. Hoggarth, K. D. Major, D. P. McCutcheon, and A. S. Clark, *Photon indistinguishability measurements under pulsed and continuous excitation*, arXiv preprint arXiv:2107.09434 (2021).
- [111] D. J. Brod, E. F. Galvão, N. Viggianiello, F. Flamini, N. Spagnolo, and F. Sciarrino, *Witnessing genuine multiphoton indistinguishability*, Phys. Rev. Lett. **122**, 063602 (2019).
- [112] T. Brünner, G. Dufour, A. Rodríguez, and A. Buchleitner, *Signatures of indis-*

- tinguishability in bosonic many-body dynamics*, Phys. Rev. Lett. **120**, 210401 (2018).
- [113] I. I. Faruque, G. F. Sinclair, D. Bonneau, T. Ono, C. Silberhorn, M. G. Thompson, and J. G. Rarity, *Estimating the indistinguishability of heralded single photons using second-order correlation*, Phys. Rev. Appl. **12**, 054029 (2019).
- [114] S. Bose and D. Home, *Generic entanglement generation, quantum statistics, and complementarity*, Phys. Rev. Lett. **88**, 050401 (2002).
- [115] N. Killoran, M. Cramer, and M. B. Plenio, *Extracting entanglement from identical particles*, Phys. Rev. Lett. **112**, 150501 (2014).
- [116] G. Ghirardi and L. Marinatto, *General criterion for the entanglement of two indistinguishable particles*, Phys. Rev. A **70**, 012109 (2004).
- [117] Y. Omar, N. Paunković, S. Bose, and V. Vedral, *Spin-space entanglement transfer and quantum statistics*, Phys. Rev. A **65**, 062305 (2002).
- [118] S. Bose and D. Home, *Generic entanglement generation, quantum statistics, and complementarity*, Phys. Rev. Lett. **88**, 050401 (2002).
- [119] S. Bose, A. Ekert, Y. Omar, N. Paunković, and V. Vedral, *Optimal state discrimination using particle statistics*, Phys. Rev. A **68**, 052309 (2003).
- [120] N. Paunković, Y. Omar, S. Bose, and V. Vedral, *Entanglement concentration using quantum statistics*, Phys. Rev. Lett. **88**, 187903 (2002).
- [121] J. Ma, X. Yuan, C. Zu, X. Chang, P. Hou, and L. Duan, *Experimental observation of entanglement duality for identical particles*, New J. Phys. **16**, 083011 (2014).

- [122] E. Moreva, G. Brida, M. Gramegna, S. Bose, D. Home, and M. Genovese, *Bell measurements as a witness of a dualism in entanglement*, Phys. Rev. A **91**, 062117 (2015).
- [123] D. Bhatti, J. von Zanthier, and G. S. Agarwal, *Entanglement of polarization and orbital angular momentum*, Phys. Rev. A **91**, 062303 (2015).
- [124] N. Lal, S. Mishra, A. Rani, A. Banerji, C. Perumangattu, and R. Singh, *Polarization-orbital angular momentum duality assisted entanglement observation for indistinguishable photons*, arXiv preprint arXiv:2104.11784 (2021).
- [125] X. Liu, G. Long, D. Tong, and F. Li, *General scheme for superdense coding between multiparties*, Physical Review A **65**, 022304 (2002).
- [126] N. Gisin, G. Ribordy, W. Tittel, and H. Zbinden, *Quantum cryptography*, Reviews of modern physics **74**, 145 (2002).
- [127] C. Couteau, *Spontaneous parametric down-conversion*, Contemporary Physics **59**, 291–304 (2018).
- [128] D. Dehlinger and M. Mitchell, *Entangled photons, nonlocality, and bell inequalities in the undergraduate laboratory*, American Journal of Physics **70**, 903–910 (2002).
- [129] L.-J. Kong, Y. Li, Y. Si, R. Liu, C. Tu, and H.-T. Wang, *Near-complete polarization bell-state analysis based on symmetry-broken scheme with linear optics*, arXiv preprint arXiv:1512.01131 (2015).
- [130] F. Wang, M. Erhard, A. Babazadeh, M. Malik, M. Krenn, and A. Zeilinger, *Generation of the complete four-dimensional bell basis*, Optica **4**, 1462–1467 (2017).

- [131] C. H. Bennett and S. J. Wiesner, *Communication via one-and two-particle operators on einstein-podolsky-rosen states*, Physical review letters **69**, 2881 (1992).
- [132] A. N. Boto, P. Kok, D. S. Abrams, S. L. Braunstein, C. P. Williams, and J. P. Dowling, *Quantum interferometric optical lithography: exploiting entanglement to beat the diffraction limit*, Physical Review Letters **85**, 2733 (2000).
- [133] P. Walther, J.-W. Pan, M. Aspelmeyer, R. Ursin, S. Gasparoni, and A. Zeilinger, *De broglie wavelength of a non-local four-photon state*, Nature **429**, 158–161 (2004).
- [134] M. W. Mitchell, J. S. Lundeen, and A. M. Steinberg, *Super-resolving phase measurements with a multiphoton entangled state*, Nature **429**, 161–164 (2004).
- [135] A. Kolkiran and G. Agarwal, *Heisenberg limited sagnac interferometry*, Optics Express **15**, 6798–6808 (2007).
- [136] F. Sun, Z. Ou, and G. Guo, *Projection measurement of the maximally entangled n -photon state for a demonstration of the n -photon de broglie wavelength*, Physical Review A **73**, 023808 (2006).
- [137] A. K. Jha, G. S. Agarwal, and R. W. Boyd, *Supersensitive measurement of angular displacements using entangled photons*, Physical Review A **83**, 053829 (2011).
- [138] J. v. Neumann, *Mathematische grundlagen der quantenmechanik (springer, berlin, (1932))*.
- [139] M. B. Plenio, *Logarithmic negativity: a full entanglement monotone that is not convex*, Physical review letters **95**, 090503 (2005).

- [140] W. K. Wootters, *Entanglement of formation of an arbitrary state of two qubits*, Physical Review Letters **80**, 2245 (1998).
- [141] S. J. Freedman and J. F. Clauser, *Experimental test of local hidden-variable theories*, Physical Review Letters **28**, 938 (1972).
- [142] J. F. Clauser and A. Shimony, *Bell's theorem. experimental tests and implications*, Reports on Progress in Physics **41**, 1881 (1978).
- [143] A. Aspect, P. Grangier, and G. Roger, *Experimental tests of realistic local theories via bell's theorem*, Physical review letters **47**, 460 (1981).
- [144] Y. Shih and C. O. Alley, *New type of einstein-podolsky-rosen-bohm experiment using pairs of light quanta produced by optical parametric down conversion*, Physical Review Letters **61**, 2921 (1988).
- [145] T. Kiess, Y. Shih, A. Sergienko, and C. Alley, *Einstein-podolsky-rosen-bohm experiment using pairs of light quanta produced by type-ii parametric down-conversion*, Physical Review Letters **71**, 3893 (1993).
- [146] G. Weihs, T. Jennewein, C. Simon, H. Weinfurter, and A. Zeilinger, *Violation of bell's inequality under strict einstein locality conditions*, Physical Review Letters **81**, 5039 (1998).
- [147] B. S. Cirel'son, *Quantum generalizations of bell's inequality*, Letters in Mathematical Physics **4**, 93–100 (1980).
- [148] A. Aspect, *Bell's theorem: the naive view of an experimentalist*, in “Quantum [un] speakables,” (Springer, 2002), pp. 119–153.

- [149] P. W. Shor, *Algorithms for quantum computation: discrete logarithms and factoring*, in “Proceedings 35th annual symposium on foundations of computer science,” (Ieee, 1994), pp. 124–134.
- [150] D. Beckman, A. N. Chari, S. Devabhaktuni, and J. Preskill, *Efficient networks for quantum factoring*, *Physical Review A* **54**, 1034 (1996).
- [151] A. Ekert and R. Jozsa, *Quantum computation and Shor’s factoring algorithm*, *Reviews of Modern Physics* **68**, 733 (1996).
- [152] C. Bennett, G. Brassard ‘*quantum cryptography: Public key distribution and coin tossing*’, in “Proceedings of IEEE International Conference on Computers, Systems & Signal Processing, Bangalore,” (1984), pp. 175–179.
- [153] S.-K. Liao, W.-Q. Cai, J. Handsteiner, B. Liu, J. Yin, L. Zhang, D. Rauch, M. Fink, J.-G. Ren, W.-Y. Liu, Y. Li, Q. Shen, Y. Cao, F.-Z. Li, J.-F. Wang, Y.-M. Huang, L. Deng, T. Xi, L. Ma, T. Hu, L. Li, N.-L. Liu, F. Koidl, P. Wang, Y.-A. Chen, X.-B. Wang, M. Steindorfer, G. Kirchner, C.-Y. Lu, R. Shu, R. Ursin, T. Scheidl, C.-Z. Peng, J.-Y. Wang, A. Zeilinger, and J.-W. Pan, *Satellite-relayed intercontinental quantum network*, *Physical Review Letters* **120**, 030501 (2018).
- [154] C. Perumangatt, N. Lal, A. Anwar, S. Gangi Reddy, and R. Singh, *Quantum information with even and odd states of orbital angular momentum of light*, *Physics Letters A* **381**, 1858–1865 (2017).
- [155] S. E. Harris, M. K. Oshman, and R. L. Byer, *Observation of tunable optical parametric fluorescence*, *Physical Review Letters* **18**, 732–734 (1967).
- [156] P. G. Kwiat, K. Mattle, H. Weinfurter, A. Zeilinger, A. V. Sergienko, and

- Y. Shih, *New high-intensity source of polarization-entangled photon pairs*, *Physical Review Letters* **75**, 4337–4341 (1995).
- [157] T. Rajesh and S. Ramachandran, *Extensive and intensive properties of aerosol over distinct environments: Influence of anthropogenic emissions and meteorology*, *Journal of Atmospheric and Solar-Terrestrial Physics* **202**, 105223 (2020).
- [158] E. Waks, A. Zeevi, and Y. Yamamoto, *Security of quantum key distribution with entangled photons against individual attacks*, *Physical Review A* **65**, 052310 (2002).
- [159] A. Scherer, B. C. Sanders, and W. Tittel, *Long-distance practical quantum key distribution by entanglement swapping*, *Opt. Express* **19**, 3004–3018 (2011).
- [160] M. Jabir and G. Samanta, *Robust, high brightness, degenerate entangled photon source at room temperature*, *Scientific Reports* **7**, 1–8 (2017).
- [161] T. Scheidl, R. Ursin, A. Fedrizzi, S. Ramelow, X.-S. Ma, T. Herbst, R. Prevedel, L. Ratschbacher, J. Kofler, T. Jennewein *et al.*, *Feasibility of 300 km quantum key distribution with entangled states*, *New Journal of Physics* **11**, 085002 (2009).
- [162] S. P. Neumann, T. Scheidl, M. Selimovic, M. Pivoluska, B. Liu, M. Bohmann, and R. Ursin, *Model for optimizing quantum key distribution with continuous-wave pumped entangled-photon sources*, *Physical Review A* **104**, 022406 (2021).
- [163] C. Bennett, G. Brassard, C. Crepeau, and U. Maurer, *Generalized privacy amplification*, *IEEE Transactions on Information Theory* **41**, 1915–1923 (1995).
- [164] A. Beer, *Bestimmung der absorption des rothen lichts in farbigen flussigkeiten*, *Ann. Physik* **162**, 78–88 (1852).

- [165] J. Yin, Y.-H. Li, S.-K. Liao, M. Yang, Y. Cao, L. Zhang, J.-G. Ren, W.-Q. Cai, W.-Y. Liu, S.-L. Li *et al.*, *Entanglement-based secure quantum cryptography over 1,120 kilometres*, *Nature* **582**, 501–505 (2020).
- [166] R. Ursin, F. Tiefenbacher, T. Schmitt-Manderbach, H. Weier, T. Scheidl, M. Lindenthal, B. Blauensteiner, T. Jennewein, J. Perdigues, P. Trojek *et al.*, *Entanglement-based quantum communication over 144 km*, *Nature Physics* **3**, 481–486 (2007).
- [167] G. Limei, R. Qi, J. Di, and H. Duan, *Qkd iterative information reconciliation based on ldpc codes*, *International Journal of Theoretical Physics* **59**, 6 (2020).
- [168] C. Bennett, G. Brassard, C. Crepeau, and U. Maurer, *Generalized privacy amplification*, *IEEE Transactions on Information Theory* **41**, 1915–1923 (1995).
- [169] D. Vasylyev, V. Vogel, and F. Moll, *Satellite-mediated quantum atmospheric links*, *Physical Review A* **99**, 053830 (2019).
- [170] G. Ribordy, J. Brendel, J.-D. Gautier, N. Gisin, and H. Zbinden, *Long-distance entanglement-based quantum key distribution*, *Physical Review A* **63**, 012309 (2000).
- [171] J. Romero, D. Giovannini, S. Franke-Arnold, S. Barnett, and M. Padgett, *Increasing the dimension in high-dimensional two-photon orbital angular momentum entanglement*, *Physical Review A* **86**, 012334 (2012).
- [172] N. J. Cerf, M. Bourennane, A. Karlsson, and N. Gisin, *Security of quantum key distribution using d-level systems*, *Physical review letters* **88**, 127902 (2002).
- [173] H. Cao, S.-C. Gao, C. Zhang, J. Wang, D.-Y. He, B.-H. Liu, Z.-W. Zhou, Y.-J. Chen, Z.-H. Li, S.-Y. Yu *et al.*, *Distribution of high-dimensional orbital angular momentum entanglement over a 1 km few-mode fiber*, *Optica* **7**, 232–237 (2020).

- [174] M. Krenn, M. Huber, R. Fickler, R. Lapkiewicz, S. Ramelow, and A. Zeilinger, *Generation and confirmation of a (100×100) -dimensional entangled quantum system*, Proceedings of the National Academy of Sciences **111**, 6243–6247 (2014).
- [175] J. Torres, A. Alexandrescu, and L. Torner, *Quantum spiral bandwidth of entangled two-photon states*, Physical Review A **68**, 050301 (2003).
- [176] F. M. Miatto, A. M. Yao, and S. M. Barnett, *Full characterization of the quantum spiral bandwidth of entangled biphotons*, Physical Review A **83**, 033816 (2011).
- [177] L. Allen, M. Padgett, and M. Babiker, *On the orbital angular momentum of light*, in “Progress in optics,” , vol. 39 (Elsevier, 1999), pp. 291–372.
- [178] M. Beijersbergen, R. Coerwinkel, M. Kristensen, and J. Woerdman, *Helical-wavefront laser beams produced with a spiral phaseplate*, Optics communications **112**, 321–327 (1994).
- [179] N. Heckenberg, R. McDuff, C. Smith, and A. White, *Generation of optical phase singularities by computer-generated holograms*, Optics letters **17**, 221–223 (1992).
- [180] E. Yao, S. Franke-Arnold, J. Courtial, M. J. Padgett, and S. M. Barnett, *Observation of quantum entanglement using spatial light modulators*, Optics express **14**, 13089–13094 (2006).
- [181] H. Qassim, F. M. Miatto, J. P. Torres, M. J. Padgett, E. Karimi, and R. W. Boyd, *Limitations to the determination of a laguerre–gauss spectrum via projective, phase-flattening measurement*, JOSA B **31**, A20–A23 (2014).

- [182] P. Vaity, J. Banerji, and R. Singh, *Measuring the topological charge of an optical vortex by using a tilted convex lens*, *Physics letters a* **377**, 1154–1156 (2013).
- [183] Z. Wang, Z. Zhang, and Q. Lin, *A novel method to determine the helical phase structure of laguerre–gaussian beams*, *Journal of Optics A: Pure and Applied Optics* **11**, 085702 (2009).
- [184] J. Leach, M. J. Padgett, S. M. Barnett, S. Franke-Arnold, and J. Courtial, *Measuring the orbital angular momentum of a single photon*, *Physical review letters* **88**, 257901 (2002).
- [185] F. A. Bovino, P. Varisco, A. M. Colla, G. Castagnoli, G. Di Giuseppe, and A. V. Sergienko, *Effective fiber-coupling of entangled photons for quantum communication*, *Optics Communications* **227**, 343–348 (2003).
- [186] S.-K. Liao, H.-L. Yong, C. Liu, G.-L. Shentu, D.-D. Li, J. Lin, H. Dai, S.-Q. Zhao, B. Li, J.-Y. Guan *et al.*, *Long-distance free-space quantum key distribution in daylight towards inter-satellite communication*, *Nature Photonics* **11**, 509–513 (2017).
- [187] D. Cozzolino, E. Polino, M. Valeri, G. Carvacho, D. Bacco, N. Spagnolo, L. K. Oxenløwe, and F. Sciarrino, *Air-core fiber distribution of hybrid vector vortex-polarization entangled states*, *Advanced Photonics* **1**, 046005 (2019).
- [188] Y. Zhang, F. S. Roux, T. Konrad, M. Agnew, J. Leach, and A. Forbes, *Engineering two-photon high-dimensional states through quantum interference*, *Sci. Adv.* **2**, e1501165 (2016).
- [189] J. Daboul, X. Wang, and B. C. Sanders, *Quantum gates on hybrid qudits*, *Journal of Physics A: Mathematical and General* **36**, 2525 (2003).

- [190] P. Chithrabhanu, S. G. Reddy, N. Lal, A. Anwar, A. Aadhi, and R. Singh, *Pancharatnam phase in non-separable states of light*, JOSA B **33**, 2093–2098 (2016).
- [191] C. Perumangatt, G. R. Salla, A. Anwar, A. Aadhi, S. Prabhakar, and R. Singh, *Scattering of non-separable states of light*, Optics Communications **355**, 301–305 (2015).
- [192] T. Kim, M. Fiorentino, and F. N. Wong, *Phase-stable source of polarization-entangled photons using a polarization sagnac interferometer*, Physical Review A **73**, 012316 (2006).

QST Group Members

Technology is not an objective to be aimed at, but a tool to be used for the benefit of common man.

-Dr. Vikram A. Sarabhai



